Universidade de Aveiro
2010/2011

Secção Autónoma de Ciências da Saúde

Igor Oliveira Marques

Modelação Molecular de transportadores transmembranares de Cloreto

Molecular Modelling of transmembranar transporters for Chloride

Universidade de Aveiro
2010/2011

Secção Autónoma de Ciências da Saúde

Igor Oliveira Marques

Modelação Molecular de transportadores transmembranares de Cloreto

Molecular Modelling of transmembranar transporters for Chloride

Dissertação apresentada à Universidade de Aveiro para cumprimento dos requisitos necessários à obtenção do grau de Mestre em Biomedicina Farmacêutica, realizada sob a orientação científica do Doutor Vítor Manuel Sousa Félix, Professor Associado com Agregação do Departamento de Química da Universidade de Aveiro.

Os estudos apresentados nesta dissertação foram realizados com recursos computacionais adquiridos ao abrigo do Programa Operacional Factores de Competitividade (COMPETE) e a Fundos Nacionais da Fundação para a Ciência e a Tecnologia (FCT) sob o projeto PTDC/QUI-QUI/101022/2008.

dedico este trabalho aos meus pais

o júri

presidente

Doutor José Carlos Fontes das Neves Lopes

professor auxiliar da Universidade de Aveiro

Doutor Vítor Manuel Sousa Félix

professor associado com agregação da Universidade de Aveiro

Doutor José Luís de Almeida

professor associado convidado da Universidade de Aveiro

Doutor Miguel Ângelo dos Santos Machuqueiro

investigador auxiliar do centro de química e bioquímica da Faculdade de Ciências da Universidade de Lisboa

agradecimentos

Ao Professor Vítor Félix, meu orientador, que se dedicou tanto como eu a este trabalho. Sem o seu apoio e motivação, não teria sido possível. Agradeço-lhe também as condições e oportunidades criadas ao longo do tempo, o companheirismo e cumplicidade que demonstrou.
Ao Professor Luís Almeida, diretor do meu mestrado e coorientador, por ter sugerido o tema e por me ter acompanhado ao longo do processo, sempre com interesse no desenvolvimento do trabalho e ao Professor Bruno Gago, vice-diretor do meu mestrado, por me ter ajudado a resolver algumas questões logísticas e incompatibilidades, garantido o meu sucesso tanto nas unidades curriculares como na tese.

Ao Paulo Costa, João Sardinha e Sílvia Carvalho, meus colegas no GMM, por me terem acolhido e partilhado os seus conhecimentos e experiência comigo. Agradeço, em particular, ao Paulo todo o excelente trabalho de revisão científica deste texto, ao João a explicação sobre os processos e a ajuda em parte do trabalho, e à Sílvia o apoio ao longo dos últimos meses.

À Cátia Magalhães, à Catarina Silva, à Rita Carreiro, ao Miguel Ângelo Costa, ao Tiago Silva (os *farmaçúticos* originais), à Joana Vieira, à Joana Oliveira, à Joana Rocha, à Sofia Varanda, à Cátia Pereira, à Carina Bernardo, à Margarida Resende e ao Edgar Coelho agradeço a amizade, cumplicidade, compreensão e companheirismo dos últimos cinco anos e todos os momentos que passámos juntos, que guardarei sempre.
Ao Joel Moreira, à Fabiana Almeida, à Rita Santos e ao João Barros, por me proporcionarem bons momentos longe do trabalho, a compreensão e paciência pelo tempo que esta tese acabou por roubar, e o apoio dado. À Joana Rita Azevedo, todo o apoio e insistência que, mesmo de longe, contribuíram para que este trabalho chegasse a bom porto.
À Sara Soares e Joana Panda, pela vossa recente amizade e apoio nesta caminhada.
Às Professoras Teresa Herdeiro, Sandra Rebelo, Sandra Vieira, Odete Cruz e Silva e Margarida Fardilha por se terem interessado em mim e no meu trabalho, pelo apoio prestado e pelos desafios que me foram colocando.

Ao Miguel Ângelo Costa e à Joana Panda, pela complementar revisão deste texto.

To Professor Philip A. Gale for providing the experimental data without which this work would not be possible. To Professor Tamás A. Martinek, for providing his force field parameters for POPC.

Aos meus irmãos, cunhados e sobrinha, pelo apoio e carinho de sempre. Sem o vosso apoio, este percurso teria sido muito mais complicado.

Aos meus pais, a quem reconheço todos os esforços dos últimos anos, para que eu pudesse seguir em frente e chegar mais longe. Sem o vosso espírito de sacrifício e a vossa disponibilidade, nada disto teria sido possível. Obrigado, do fundo do coração.

palavras-chave

dinâmica molecular, fibrose cística, receptores sintéticos, reconhecimento de aniões, simulações de membranas, transporte de aniões, GAFF, POPC

resumo

O transporte de iões através da membrana celular é crucial para a manutenção da homeostasia celular e orgânica. Quando o transporte de iões está afectado, várias patologias podem surgir, tais como canalopatias. Durante a última década surgiram vários potenciais substitutos de origem sintética para os canais iónicos afectados, com a capacidade de mimetizarem as suas funções. Neste contexto, receptores sintéticos trípodes, incorporando grupos de reconhecimento tioureia, foram investigados experimentalmente como receptores de aniões e transportadores transmembranares. Os resultados obtidos demonstraram a capacidade destes carregadores para mediarem a difusão de cloreto através de vesículas lipídicas de POPC. Com base nestes indícios, realizaram-se estudos computacionais com duas moléculas desta série de receptores, em solução e numa membrana fosfolípidica, utilizando cálculos de mecânica molecular e simulações de dinâmica molecular, com recurso ao campo de forças GAFF. Nesta tese são apresentados e analisados os resultados obtidos.

Os estudos efectuados em solução de dimetilsulfóxido/água mostram que as associações com cloreto são estabilizadas por múltiplas ligações de hidrogénio N-H•••Cl^-. Por oposição, quando solvatados em água, os receptores perdem imediatamente o anião. Os comportamentos observados sugerem a utilização potencial destas moléculas como transportadores membranares.

Antes da avaliação do comportamento das associações com cloreto no modelo de membrana, investigou-se o modelo de água e as cargas atómicas dos fosfolípidos, utilizados conjuntamente com o GAFF na descrição da bicamada fosfolípidica. Determinou-se que o melhor conjunto de parâmetros consiste no modelo de água SPC/E e cargas atómicas RESP não constrangidas.

As duas associações com cloreto foram colocadas em duas posições iniciais alternativas num modelo de membrana super-hidratado: dentro da bicamada e na fase aquosa. Genericamente, observou-se a migração de ambos os receptores para a interface água/lípido. Adicionalmente, no primeiro cenário, a libertação do cloreto ocorre com a chegada receptores à interface, enquanto que, no segundo cenário, o cloreto é libertado na fase aquosa antes da internalização dos receptores. Na maioria dos casos, os receptores aninharam-se perto das cabeças dos fosfolípidos, afectando ligeiramente alguns dos parâmetros biofísicos da membrana.

keywords

anion recognition, anion transport, cystic fibrosis, membrane simulations, molecular dynamics, synthetic receptors, GAFF, POPC

abstract

Ion transport across cell membranes is crucial for the maintenance of cellular and organic homeostasis. When the ions transport is impaired, several disorders may arise, such as channelopathies. Over the last decade, potential synthetic substitutes for the impaired ion channels have been developed, with the ability to mimetic their functions. In this context, tripodal synthetic molecules incorporating thiourea binding groups were experimentally investigated as anion receptors and transmembranar transporters. The obtained results demonstrated the ability of these carrier molecules to mediate the chloride diffusion across POPC lipid vesicles. Inspired by these hints, computational studies with two molecules of this receptors' set were undertaken in solution and in phospholipid membrane, using molecular mechanics calculations and molecular dynamics simulations, with the GAFF force field. This thesis reports and analyses the results obtained.

The solution studies carried out in dimethyl sulfoxide/water solution show that the anion associations are stabilised by multiple N-H•••Cl^- hydrogen bonds. In contrast, when solvated in water, the receptors promptly released the anion. The observed behaviours suggest the potential use of these carriers as membrane transporters.

Before the evaluation of the chloride associations' behaviour in the membrane model, the water model and phospholipid atomic charges to be utilized along with GAFF, describing the phospholipid bilayer, were investigated. The best set of parameters found is composed of SPC/E water model and unconstrained RESP atomic charges.

The two chloride associations were placed in an overhydrated membrane model in two alternative starting positions: inside of the bilayer and in the water phase. Generally, the migration of the receptors to the water/lipid interface was observed. Moreover, in the first scenario, the chloride release occurs when the carrier reaches the interface, while in the second one, the chloride release happens in the water phase, before the receptors' internalization. In most cases, the receptors have nested themselves near the lipid head groups, exerting little effect on the studied biophysical membrane parameters.

publicações e comunicações científicas

com base no trabalho descrito nesta dissertação, foram elaborados os seguintes pósteres científicos:

- I. Marques; V. Félix, Chloride Transmembranar Transport assisted by Thiourea Tripods: a MD Investigation. 5th Theoretical Biophysics International Symposium (TheoBio 2011), Funchal - Madeira, 2011.

- V. Félix; I. Marques; J. Sardinha; P. J. Costa; P. A. Gale; M. Wenzel; N. Busschaert; C. J. E. Haynes; S. J. Moore, Chloride Transmembranar Transport assisted by Thiourea based synthetic Receptors: a Molecular Dynamics Investigation. 6th International Symposium on Macrocyclic and Supramolecular Chemistry (6-ISMSC), Brighton - England, 2011.

aqui encontrará os documentos acima, bem como este documento em PDF:

here you will find the documents above, as well as this document in PDF:

Index

Figures Index

Tables Index

Schemes Index

Abbreviations

Item	*Definition*
$\|S_{CD}\|$	Deuterium order parameter
^{13}C NMR	Carbon 13 Nuclear Magnetic Resonance
^{1}H NMR	Proton Nuclear Magnetic Resonance
ADP	Adenosine Diphosphate
AM1BCC	Semi-empirical Austin Model 1 Bond Charge Corrections
AMBER	Assisted Model Building and Energy Refinement
AMP	Adenosine Monophosphate
ATP	Adenosine Triphosphate
CACNL1A4	Voltage-gated Ca^{2+} channel
CFTR	Cystic Fibrosis Transmembrane conductance Regulator
CHARMM	Chemistry at HARvard Molecular Mechanics
CSD	Cambridge Structural Database
DLPC	1,2-didodecanoyl-*sn*-glycero-3-phosphocholine
DMF	Dimethylformamide
DMPC	1,2-dimyristoyl-*sn*-glycero-3-phosphocholine
DMSO	Dimethyl sulfoxide
DNA	Desoxyribonucleic Acid
DOPC	1,2-dioleoyl-*sn*-glycero-3-phosphocholine
DOPC	1,2-dioleoyl-*sn*-glycero-3-phosphocholine
DOPE	1,2-dioleoyl-*sn*-glycero-3-phosphoethanolamine
DPPE	1,2-dipalmitoyl-*sn*-glycero-3-phosphoethanolamine
ESP	Electrostatic Potential
EYPC	Egg-Yolk Phosphatidylcholine
frcmod file	AMBER force field modification file
GABA	Gamma-Amino Butyric Acid
GAFF	General AMBER Force Field
GLUT	Glucose transporter
GROMACS	GROningen MAchine for Chemical Simulations
GROMOS	GROningen MOlecular Simulation
LINCS	Linear Constraint Solver
MARTINI	MARrink Toolkit INItiative
MD	Molecular Dynamics
MM	Molecular Mechanics

Item	***Definition***
MM-PBSA	Molecular Mechanics Poisson-Boltzmann Surface
mol2 file	Tripos Mol2 file
NAMD	Not (just) Another Molecular Dynamics program
NMR	Nuclear Magnetic Resonance
NPT	Isothermal–isobaric ensemble
NVT	Canonical ensemble
OPLS	Optimized Potentials for Liquid Simulations
PDB file	Protein Data Bank file
PME	Particle Mesh Ewald
POPC	1-palmitoyl-2-oleoyl-s*n*-glycero-3-phosphocholine
POPE	1-palmitoyl-2-oleoyl-s*n*-glycero-3-phosphoethanolamine
POPG	1-palmitoyl-2-oleoyl-s*n*-glycero-3-phospho-rac-(1-glycerol)
PyMOL	Python-enhanced molecular graphics tool
RDF	Radial Distribution Functions
RESP	Restrained Electrostatic Potential
siRNA	Small interfering RNA
sn-1	Stereospecific number 1
sn-2	Stereospecific number 2
sn-3	Stereospecific number 3
SPC	Single Point Charge
SPC/E	Extended Single Point Charge
TBA	Tetrabutylammonium
TIP3P	Transferable Intermolecular Potential 3 Point
TIP4P	Transferable Intermolecular Potential 4 Point
TIPS3P	Transferable Intermolecular Potential 3 Point
TREN	Tris(2-aminoethyl)amine

1 Introduction

This chapter begins with a brief description of the cell membrane including its composition, and the structures responsible for the transport of substances between the media inside and outside the cell. Subsequently, channelopathies, *i.e.*, diseases derived from the defective anion transmembrane transport through ionic channels, will be addressed, namely those related with the chloride transport. In this context, examples of the different synthetic receptors currently available to mediate the anion transport as well as the corresponding mechanisms will be focused. In the scope of this work, a particular attention will be dedicated to the synthetic carriers designed for the chloride transport. Thus, the single crystal X-ray diffraction structures of tren (tris(2-aminoethyl)amine) based carriers, as well as their associations with relevant biological anions will be described. The experimental anion transport results that support this thesis will also be described.

To understand the modelling studies presented, a brief description of the basic concepts associated with Molecular Dynamics simulations based on classical force fields will also be given.

1.1 Transmembranar transport and channelopathies

1.1.1 Biomembranes: brief characterization

The cell membrane surrounds the cell contents, controlling the in and out movement of substances, and maintaining the structural and physical properties of the cell, as well as the fundamental differences between the cytosol and the cell surroundings, as shown in Figure 1.(1, 2) The cytosol has higher concentration of potassium and phosphate ions, while outside the cell, the ions with higher concentration are sodium, calcium and chloride, to attain the proper conditions for the normal functioning of the cell and its components.(3)

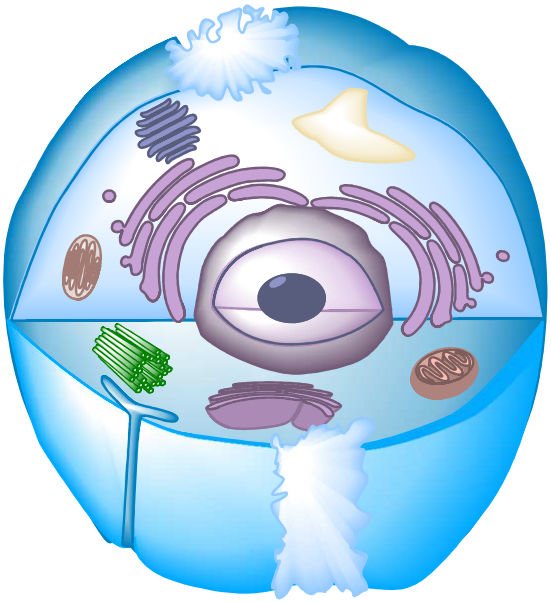

Figure 1 – Schematic representation of the cell membrane (blue). It surrounds the whole cell, separating its contents from the outer medium and maintaining its structural properties.

The cell membrane is a semipermeable structure, allowing only some substances to pass through it and excluding others, being composed of a lipid bilayer and several proteins that act as receptors or sensors to changes in the interstitial fluid.(1, 4) The lipid bilayer is quite heterogeneous, being composed of phospholipids, sphingolipids (derivatives from sphingosine that contain a long-chain fatty acid attached to the sphingosine amino group) and steroids (cholesterol and its derivatives).(2) Phospholipids represented by the orange structures in Figure 2,(2, 4) are amphipathic molecules, whose nonpolar (hydrophobic) chains are directed towards the bilayer's core, and whose polar (hydrophilic) heads are oriented towards the bilayer exterior and in contact with either the interstitial fluid or with the cytosol. Cholesterol is evenly distributed between leaflets and the remaining bilayer components are distributed asymmetrically, with a larger percentage of sphingolipids and phosphatidylcholine lipids in the outside layer, while the inside layer comprises most of the phosphatidylethanolamine lipids.(2, 5) Some of the proteins associated with the membrane might present some motility, changing their position in the membrane like a cork floating on water, while other proteins have little or no motility due to their anchorage to the cell cytoskeleton or to an outer matrix. There are three types of proteins associated to the membrane:

- *Integral proteins* (or *intrinsic proteins*), which are embedded in the membrane, spanning the bilayer from side-to-side. The segments that cross the width of the

membrane are commonly composed of amino-acids with nonpolar side-chains. This type of proteins is represented by the red structure in Figure 2;(3)

- *Peripheral proteins* (or *extrinsic proteins*), which are in contact only with the surface of one of the bilayer's leaflets, not penetrating it, facing either the cytosol or the interstitial fluid. Cyan and light green structures in Figure 2 represent, in this order, peripheral proteins present in the outside and in the inside leaflets of the cell membrane;(3)
- *Lipid-anchored membrane proteins*, which are covalently bonded to a lipid inserted into the membrane. This lipid can be a phosphatidylinositol, a fatty acid, or a prenyl group. The peptide does not enter the phospholipid bilayer and is represented by the brown structure in Figure 2.(2, 6)

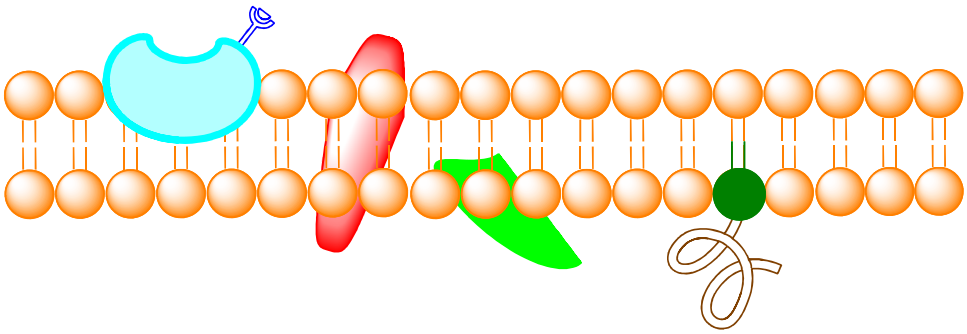

Figure 2 – Schematics of the phospholipid bilayer structure of the cell membrane.

In addition, most of these proteins present a carbohydrate molecule attached to the face exposed to the interstitial fluid and are, therefore, designated glycoproteins, shown as the blue structure in Figure 2.(3)

The hydrophobic core of the membrane prevents the diffusion of water and hydrosoluble solutes and the van der Waals interactions help to keep the membrane's structure and stability.(2) This way, the necessary molecules are unable to leave the cell, as they are needed for its normal functioning, and the unnecessary or harmful substances are kept outside.(3)

Inside the cell, several organelles rely on membranes, such as the endomembrane system (nuclear envelope, endoplasmic reticulum, Golgi body, endosome and lysosomes or vacuoles) or mitochondria (not part of the endomembrane system), being bond by similar membranous structures.(6)

1.1.2 Transport across the membrane

Passive Diffusion

Small uncharged polar molecules (*e.g.*, urea and ethanol), and gases such as O_2 and CO_2 can diffuse across cellular membranes without assistance. These movements occur without any energy expense, *i.e.*, the species move spontaneously accordingly to the concentration gradient, and the rate of diffusion is proportional to the concentration gradient of that molecule. Also an important factor for the passive diffusion of a molecule across the membrane is its hydrophobicity, as a highly hydrophobic molecule diffuses faster across the cell membrane than a substance with low hydrophobicity.(2)

Charged molecules have their movement across the membrane not only influenced by concentration gradients but also by membrane potential (derived from the different concentrations of anions and cations on both sides of the membrane). This electrochemical gradient only allows the movement of charged energetically favoured species.(2)

Aided transport: Facilitated Diffusion, Active Transport and other mechanisms

As stated above, charged molecules have little capability to cross the cellular membrane through passive diffusion. Instead, they rely on the existent proteins on the membrane. Additionally channels and transporters may exist for neutral species that can diffuse across the membrane, such as the family of five membranar proteins GLUT1-5 that increases the intake of glucose at greater rates than passive diffusion allows.(2, 6)

One mechanism that relies on proteins present in the cell membrane is **facilitated diffusion**. Indeed, channel-like proteins transport water and other substances accordingly to their electrochemical gradient. Units from these proteins form a hydrophilic channel across the membrane, allowing the rapid movement of multiple molecules at once. Ion channels may be open most of the time – nongated channels – or open or close in response to a certain electrochemical signal – gated channels.(2)

The transport dependent of energy is designated as **active transport** and requires energy obtained through hydrolysis of adenosine-5'-triphosphate (ATP) to move the species against their electrochemical gradient. The proteins that carry out this process are ATPases – enzymes which enhance the decomposition of ATP into adenosine-5'-(trihydrogen

diphosphate) (ADP) and a free phosphate ion, releasing the energy for subsequent chemical reactions, as in the sodium-potassium pump.(2, 7)

Transport through the membrane can also be mediate by other natural **cotransporters** which are classified in agreement with the transport mechanism employed, as follows:

- *Uniporters*, which mediate the transport of only a type of species accordingly to its concentration gradient, *via* facilitated diffusion. Glucose, as previously mentioned, and amino acids are two kinds of substances that benefit from this mechanism;(2)
- *Symporters*, which allow the transport of a solute in the same direction of an ion moving accordingly to its electrochemical gradient. This process is also known as cotransport;(3)
- *Antiporters*, which allow the movement of a solute in the opposite direction of an ion which moves accordingly to its electrochemical gradient. This process is also designated as exchange.(3)

These transporters are integral membrane proteins, with high specificity to the species they transport. Furthermore, symporters and antiporters cannot function without the ion that moves accordingly to its electrochemical gradient and supplies the energy necessary for the transport of the other species against its own electrochemical gradient. Sodium is one of the most common ions on which these transporters rely on, with the cotransport of sugar and amino acids in the small intestine and in the renal tubule, and with the exchange of H^+ and Ca^{2+}, for the cell internal pH control and to keep a low cytosolic calcium concentration, with a net charge movement.(3)

Moreover, the movement of ions across cellular membranes also occurs throughout **ion channels** composed of embedded membrane proteins occupying semi-static positions in the membrane and spanning it from side-to-side.(8) Alternatively, mobile molecules promote the facilitated diffusion of ionic guests and may diffuse themselves (like shuttles, moving outwards the cell, then inwards the cell, and repeating this movement) across the hydrophobic component of the membrane. Such molecules are small polypeptides, as the antibiotic valinomycin, and are designated as **ion carriers.**(7, 8) The different transport features related with those two natural ion transport mechanisms across the membrane are addressed in Table 1 and are discussed in more detail in the following section. Additionally, Table 2 summarizes and compares the previously mentioned types of membranar transport for several species.

Table 1 – Differences between carrier and channel transporters.*

Ion Carriers	***Ion Channels***
Transport ions with high selectivity	Less selective in ion transport
Transport rate below limit of diffusion	Transport rate approaches limit of diffusion
Usually monomeric	Usually oligomers of identical subunits
Transport activity not gated	Transport activity often gated in response to cellular events

*Adapted from Davis *et al.*(8)

Table 2 – Mechanisms for transporting ions and small molecules across cell membranes.*

Property	*Requires specific molecule*	*Solute transported against its gradient*	*Coupled to ATP hydrolysis*	*Driven by movement of a cotransported ion down its gradient*
Passive Diffusion	No	No	No	No
Facilitated Diffusion	Yes	No	No	No
Active Transport	Yes	Yes	Yes	No
Cotransport	Yes	Yes	No	Yes

*Adapted from Lodish *et al.*(2)

1.1.3 Channelopathies

Normal ion channels functioning

As previously mentioned, ion channels are transmembrane proteins, spanning the cell membrane and carrying out more functions beyond the electric excitability of muscular and nervous cells, thus reflecting the importance of ions in the tasks presented in Table 3.

Table 3 – Functions of ion channels.*

Level of task	Task
Cellular Level	• Volume and cell pH regulation • Osmotic balance regulation • Ca^{2+} concentration regulation • Contractility (heart, skeletal muscle, smooth muscle) • Neuronal excitability • Cell proliferation • Sensory transduction
Organism Level	• Transepithelial transportation (gut, kidney, lung) • Hormone secretion (adrenals, gonads, pituitary, pancreas) • Bone metabolism • Learning and memory • Regulation of blood pressure

*This table gathers information retrieved from refs. (8-11)

Furthermore, ion channels incorporate several polypeptide subunits that form a hydrophilic channel, with a 3-5 Å diameter, through which ions can move from one side of the membrane to the other.(3, 11) In addition, integral membrane proteins can form different types of ion channels through which different species (not exclusively ions) may cross the cell membrane, as summarized and compared in Table 4.

As pores have no gates, no conformational changes occur, while channels experiment conformational changes between open and closed gate states. When channels are open, both intracellular and extracellular media are communicable, allowing several ions to cross the membrane during that "opening" event*.(7)

Carriers, on the other hand, are virtually never open on both sides, so an "opening" is not appropriate to describe the event that allows the movement of ions; a better expression to the opening and closing of the gates on each side of the carrier is "cycle of conformational changes". The limitations of this cycle and the few binding sites in a carrier both reduce the number of particles that move from one side of the membrane to the other during an event.(7)

* The length of an "event" is variable between the several types of integral proteins

Table 4 – Types of passive, non-coupled transport through integral membrane proteins.*

Pathway type	*Pore*	*Channel*	*Carrier*†
Description	The protein subunits form a pore that is permanently open	The membrane protein forms a channel with a movable gate (or barrier). The gate is able to open or close	The protein forms a pathway with a tunnel that is a discontinuous transmembrane path, due to gates that are never open at the same time, with a compartment that can contain binding sites for the transported species
Status	Permanently open, without gates	Intermittently open, with one gate	Never open, with at least two gates
Molecules transported	Up to 2×10^9/s	10^6-10^8/s when open	200-50000/s
Examples	Porins in the outer membranes of mitochondria and aquaporins (water channels)	Almost all ion channels that allow Na^+, Cl^-, K^+, and Ca^{2+} to cross the membrane	Carriers that move single solutes through the membrane via facilitated diffusion (eg: GLUT1)

*Adapted from Boron *et al*.(7)
†This is an integral protein, with little mobility in the membrane. It should not to be confused with the *Ion Carrier* definition previously presented, a mobile molecule that only transports ions as a shuttle.

Gated ion channels consist of at least one polypeptide subunit, presenting α helical membrane-spanning segments and several functional segments – adapted from (7, 9):

- **Gate** – determines if the channel is opened or closed (with different protein conformations);
- **Sensors** to respond to a specific signal from the following:
    a. Changes in membrane potential;
    b. Second messenger systems acting in the cytosolic face of the membrane protein;
    c. Ligands that bind to the extracellular face of the membrane protein;
- **Selectivity filter** – determines which type of ion (either anions or cations) or which specific ions can permeate the channel (*e.g.*, Na^+, Ca^{2+}, Cl^-) – cation channels often present negatively charged residues near these selectivity filters, attracting cations and repelling anions;
- **Open channel-pore** – During the open channel conformation, a continuous pathway across the membrane is established, allowing the passive flow of ions until the channel closes again.

Regarding the most common ion channels, they are characterized in Table 5.

Table 5 – Most common ions channels characterization.*

Type of channel	*Ion*	*Electrochemical potential difference*	*Typical ion passive movement*	*Function/Role*
Cation Channels	Na^+	Strongly negative	Inward the cell	Action potential generator in many excitable cells
	K^+	Close to zero or somewhat positive	At equilibrium or outward of the cell	Resting membrane potential generator; action potentials terminator in excitable cells
	Ca^{2+}	Strongly negative	Inward the cell	Transmembrane signalling in excitable and nonexcitable cells; action potentials generator in excitable cells
Anion Channel	Cl^-	Modestly positive	Outward of the cell	Transepithelial movement of Cl^- in basolateral membranes

*Adapted from Boron *et al.* (7)

Ion channels have become a common target for diseases affecting tissues referred in Table 3. Based on the rationale that ion channels are responsible for some diseases, the following types of drugs have ion channels as therapeutic targets: antiepileptic drugs, local anaesthetics, migraine treatments, antipsychotics and mood stabilizers, antiarrhythmics, antihypertensives, and oral hypoglycaemic agents.(11)

Ion channels dysfunctioning

Channel dysfunctioning (*i.e.*, channelopathy) may be attributed to several causes:

- Mutations in the promoter region of the ion channel gene may change its expression: diminishing or augmenting it;(9)
- Mutations in the coding region of the ion channel gene may lead to the gain or loss of channel functions, both with harmful effects;(9)
- Some channelopathies result from inappropriate regulation of channel activity by intra or extracellular signals (ligands or modulators), due to defects in their encoding genes or in their production pathways;(9)
- Autoantibodies to the channel protein may enhance or decrease its functioning, leading to autoimmune diseases. These autoantibodies bind to specific extracellular epitopes on glycoprotein ion channels;(9, 11)

- When secreted by cells and after inclusion in another cell's membrane, ion channels may act as lethal agents, acting as non-selective pores that lead to the lysis and death of the latter cell (the haemolytic toxin produced by *Staphylococcus aureus* is an example of this type of ion channel);(9)
- Ion channels function as targets for venoms or toxins that function as enhancers or ion channels blockers, modulating their functions. These malfunctions are examples of the first channelopathies detected, and were the motto for the development of therapeutic drugs.(9, 11)

Genetic origin

Recently, a connection between heritable defects in ion channels coding genes and channelopathies has been established.(12) The genetic coding of the major α subunit of human muscle sodium channel, in chromosome 17q, was shown to be linked to hyperkalemic periodic paralysis, a disorder of skeletal muscle excitability.(12) During the last two decades, the list of channelopathies has increased and currently includes over 40 diseases. These disorders are associated with mutations of all the major classes of voltage-gated ion channels (Na^+, K^+, Ca^{2+}, Cl^-), several fast ligand-gated receptors or channels (nicotinic acetylcholine receptor, glycine receptor, Gamma-Amino Butyric Acid (GABA) receptor), intracellular channels (ryanodine receptor, Ca^{2+} release channel), and intercellular channels (connexins).(11, 13) In spite of the genetic origin of these disorders, the working mechanisms of different ion transporters should not be overlooked, whether they are passive channels, or ATP dependent pumps, or if they function as simple channels *via* uniport mechanism or are based in symport or antiport mechanisms.(10, 11)

When approaching a channelopathy, one must consider that the disorder presentation may be due to a single mutation or may be related to several possible mutations. The two following concepts are important:

- **Phenotypic heterogeneity** – different mutations in the same gene can cause different diseases (*e.g.*, mutations in voltage-gated Ca^{2+} channel, CACNL1A4, result in episodic ataxia type 2, familial hemiplegic migraine, and spinocerebellar ataxia type 6);(9, 13)
- **Genetic heterogeneity** – mutations in different genes can result in the same clinically apparent disease phenotype (*e.g.*, three independent mutations in three different genes all result in long QT syndrome, a rare cardiac disorder that causes sudden death from ventricular arrhythmia in young people).(9, 13)

Channelopathies are commonly recognized after a trigger that results in an attack. This trigger might be the rest after an intense physical activity, hormones, stress or specific types of food. These attacks may last from some minutes to some days, presenting spontaneous and complete remission afterwards, with a special onset during the first two decades of life and improving by the fifth decade of life and not showing chronic progression.(14)

Channelopathies associated with chloride transport

The chloride anion is critical for the maintenance of the membrane potential and is the most abundant of the three most common physiological anions, along with phosphate and bicarbonate. Furthermore, among these inorganic ions, chloride is the most lipophilic one.(15) Chloride channels play an important role in membrane excitability, transepithelial transport, cell volume and intracellular pH regulation. Additionally, inside the cell, chloride ion channels provide an electrical shunt pathway which facilitates the acidification of organelles. The best well-characterized chloride ion channels are the voltage-gated chloride channels, the cystic fibrosis transmembrane conductance regulator (CFTR) and related channels, and the ligand-gated chloride channels opened by GABA and glycine.(9)

Many channelopathies associated with chloride ion channels were discovered during the last fifteen years. Some diseases associated to these channels are epilepsy, startle disease (neurologic disorder), deafness, blindness, lysosomal storage and degradation, Bartter syndrome type III (severe renal salt loss), Dent's disease, some forms of myotonia (muscle stiffness), osteopetrosis (bone disease), pulmonary infections and fibrosis (cystic fibrosis), male infertility, and renal stones development. This *plethora* of diseases shows the importance of chloride transmembrane transport for the human health.(8-10)

Cystic fibrosis is one of the most frequent hereditary diseases, with one case in 2000 to 4000 births. Patients suffering from this condition have a mean life expectancy between 20 to 40 years, most of them fighting chronic pulmonary infections (which result in lung destruction, right heart insufficiency, and heart failure).(14)

The CFTR gene codes the CFTR protein, which acts as the chloride channel as well as the regulator for other ion channels. When CFTR is mutated, the NaCl and water secretion in the airways is reduced, with simultaneous NaCl absorption enhancement. This combination of events precludes the airway cleaning process, allowing pathogenic bacteria to colonize the airways, infecting and destroying them.(14)

1.2 Synthetic ionophores

1.2.1 Overview

Along the last decade, inspired by the natural ionophores, the supramolecular chemists have devoted a particular attention to the design and development of synthetic receptors with potential for ion transmembranar transport,(16, 17) *i.e.*, to act as ionophores. An ionophore is commonly defined as *A compound which can carry specific ions through membranes of cells or organelles.*(18) In a deeper definition, this is a class of *Chemical agents that increase the permeability of biological or artificial lipid membranes to specific ions. Most ionophores are relatively small organic molecules that act as mobile carriers within membranes or coalesce to form ion permeable channels across membranes. Many are antibiotics, and many act as uncoupling agents by short-circuiting the proton gradient across mitochondrial membranes.*(19)

Therefore, ionophores are typically considered as small molecules, capable of carrying ions or of facilitating their diffusion through a biomembrane, using a wide range of mechanisms. These compounds are naturally occurring as peptides, cyclic depsipeptides, macrotetrolides, and polyether antibiotics,(20) but can also be prepared in laboratory, being labelled as **synthetic ionophores**.(20, 21)

However, unlike the common natural occurring cation ionophores (*e.g.*, valinomycin and gramicidin A for K^+),(15) the natural occurring anion ionophores are not abundant. Some examples of natural anion receptors include pamamycins, macrodiolides with antibiotic activity;(22) duramycins, peptides that form weak selective anion channels;(23) and prodigiosins, which act as H^+/Cl^- symporters without ATP hydrolysis.(24) The prodigiosin receptors are both anion and cation ionophores.(15, 25) The basic structural units of these anion receptors are sketched in Scheme 1.

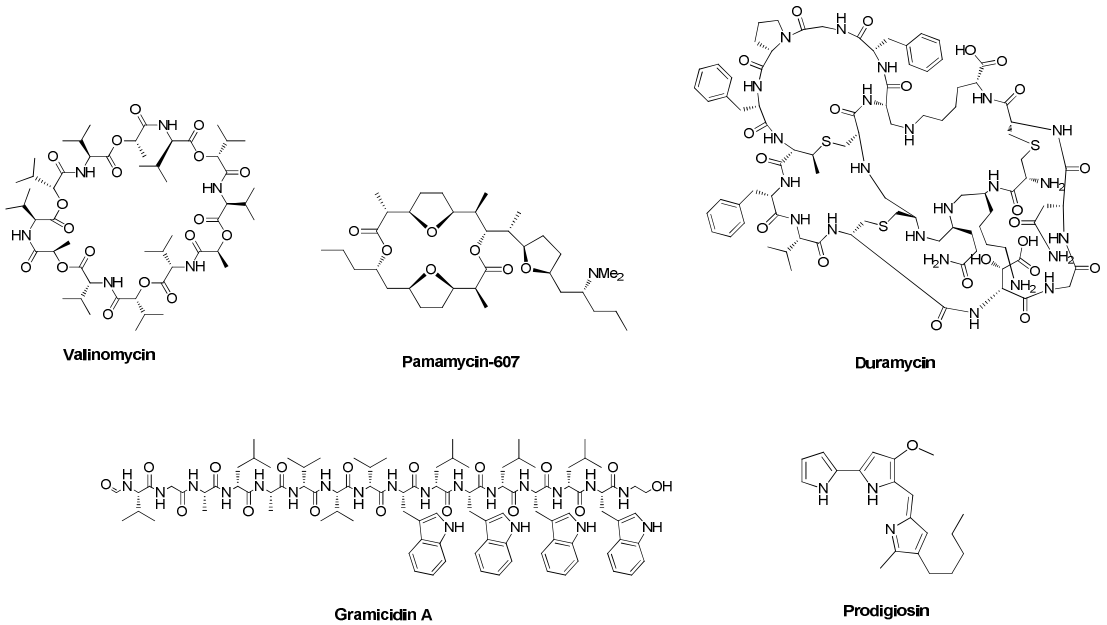

Scheme 1

Nowadays, the reduced number of natural anionophores available is a strong driving force in the development of synthetic anion receptors, especially the amphiphilic receptors, which may be utilized in the transport of anions through the phospholipid bilayer, as not every anion receptor has the potential to become a membrane transporter.(8)

These synthetic ionophores share some structural characteristics with the natural occurring ion channels,(15) bringing some enlightenment to the ion transport process across the membrane, and might even be applied as therapeutics in some channelopathies.(8) In cystic fibrosis, the replacement of the malfunctioning ion channels with peptide based ionophores has recently been proposed,(26) but it must be taken in account that, to develop a potential pharmaceutical application with an anionophore, the methods for medicine administration have to be considered: an anionophore applied to cystic fibrosis therapy should be amphiphilic, with sufficiently hydrophilicity for delivery in the lungs, and lipophilicity enough to be internalized in the epithelial target biomembranes, where the residence time should be adequate.(15, 27) And, of course, if these ionophores are to be applied as therapeutics, several factors should be looked at, such as the pharmacokinetics and safety profiles.(28)

Noteworthy, is the need of these ionophores to be able not only to separate the anion from water, but also from their (if existent) cation partner – ability shown, so far, only by cholapods,(15) whose study has been deepen to demonstrate that increased lipophilicity has

no real advantage for these receptors and that the pre-organized structure of cholapods really is beneficial.(29)

The historical hallmarks of research in the field of synthetic ionophores are addressed in Table 6. Initially, the development of synthetic ionophores was based on the structural modification of natural transporters, aiming to improve their affinity with anionic guests or their solubility properties.(15) Progress in this area was, and still is, sought through the synthesis of anionophores from scratch, with no natural components.(15)

Table 6 – Summary of advances in synthetic ionophores.

Year	*Hallmark*	*Refs.*
1967	Synthesis of the first synthetic ion-carrier	(30)
1968	First report of anion (Cl^-) recognition and complexation by Macrobicyclic Amines	(31)
1978	First attempts to synthesize an ionophore	(32, 33)
1982	First reports of man-made ionophore synthesis	(34, 35)
1998	First report of a crystal structure of a biological ion channel	(36)
2005	Understanding of conductivity and selectivity based on architecture and chemistry of pathways	(37)

1.2.2 An outlook on the development of synthetic anionophores

This section presents some examples of synthetic receptors successfully tested as anions transmembrane transporters, which are appointed as good examples to illustrate the existent mechanisms in anion transport across biomembranes. Therefore this section is not intended to provide an exhaustive review on the subject. Comprehensive reviews on the recent advances in synthetic transmembranar anion transporters can be found on refs. (8, 21, 38-47) Also, in these reviews, beyond ionophores, other receptors are presented, with the potential to be applied as health related applications.

Two of the mechanisms for the transport of ions that employed by synthetic ionophores also mimic natural mechanisms of ion carriers and ion channels, as depicted in Figure 3.

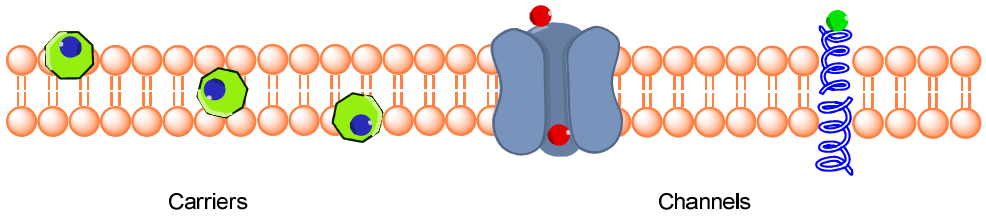

Figure 3 – Schematic representation of the carriers and channel mechanisms employed by the synthetic transporters.

Molecules that form receptor-ion complexes, shuttling in and out of the cell and wrapping the ion are designated as **carriers.** The exterior of a carrier is typically hydrophobic and this mechanism presents high selectivity.(15, 20) With less mobility, **channels** insert and span the biomembrane, forming static polar channels that allow the in or out movement of anions as well as some cations.(15, 20) These channels may rely on one unit or on several subunits.(48) Some examples of synthetic ionophores that rely on such mechanisms are described below:

Glycine-based polymeric receptors for chloride transport were developed by Gokel's workgroup. These peptides form self-assembled pores that span the liposomal membranes, thus allowing the movement of chloride across the membrane.(49, 50)

A remarkable contribution to the anion transport arena was given by Matile's workgroup, with the synthesis of oligonaphthalenediimide rods, which form anion–π slides that span the membrane and anions are transported *via* a multi-ion hopping system (several receptors are present in a cluster that spans the membrane: as an anion binds to a receptor, the previously bond anion is pushed to the next receptor, hopping its way through the membrane).(51) Tubular architectures based in aligned macrocycles that transport anions in a mechanism resembling a ladder, were also developed by this group.(52)

Calixarenes, cyclodextrins and calixpyrroles have been employed in the design of a wide group of functionalized anion transporters.(8, 53) The first two macrocyclic classes operate as channels. In the case of the calixarenes, the channel is a calix-tube spanning the membrane or alternatively it is derived from the self-assembly of several calixarene units inside the phospholipid bilayer, as observed for gramicidin polypeptide (see Figure 3, above).(53) In contrast, the calixpyrroles mediate the anion transport as carriers.(48)

Davis and co-workers developed cholapods, receptors based on cholic acid. In this rigid steroid platform it is possible to anchor amines that can be modified to urea or thiourea groups. The ability of urea-substituted cholapods to transport chloride as carriers was demonstrated by his workgroup, Furthermore, beyond its synthetic versatility, cholic acid is widely available and at low cost.(44)

Other receptors exist that cannot be classified as ion carriers or channels, which operate *via* a **relay mechanism.** Receptor molecules are aggregated inside the membrane and the anion transport occurs as depicted in Figure 4. For instance, Smith *et al.* developed a phospholipid derivative incorporating urea binding group (see Scheme 2). Such receptor uses this relay mechanism. The structural similarity between this receptor and the phospholipids in the membrane is obvious, and consequently is compatible with the membrane structural environment.(27)

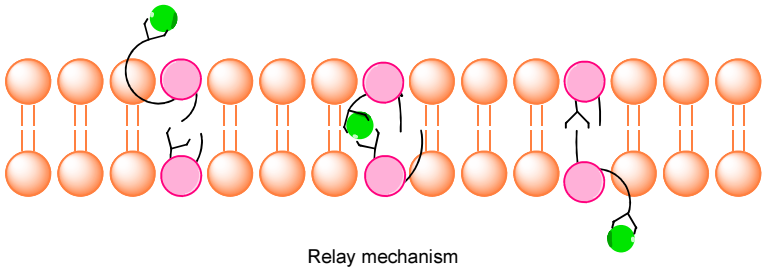

Figure 4 – Representation of the relay mechanism proposed by Smith and co-workers for these derivatives showing the active two molecules aggregate dependent of the membrane thickness.

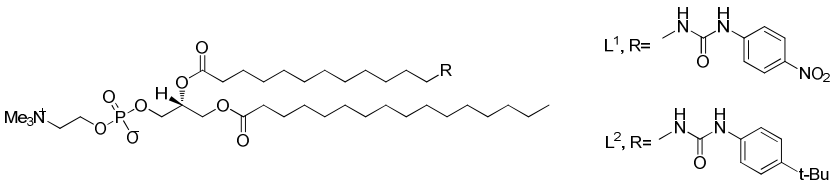

Scheme 2

In all cases reported in this section the anion is recognised by multiple hydrogen bonds and electrostatic interactions. Furthermore, the strength of the binding association determines the use of a receptor as a transmembranar transporter.(48, 54) In other words, a strong binding constant precludes the anion release to the surrounding membranar aqueous environment, while a weak binding constant will prevent the uptake of the anion from the aqueous medium.

Concluding this section, two notes are important:

- High concentrations of receptors are able to disrupt biomembranes in a detergent-like fashion,(55) probably due to structural and dynamic changes in the bilayer.
- For chloride there are already available a significant number of synthetic transporters. However, a literature search revealed that this is not the case for other biological relevant anions such as bicarbonate, organic carboxylates, organic phosphates, and sulphates. In other words, the development of synthetic transporters for these polyatomic anions is still a challenge.(25)

1.3 Application of the tren unit in the design of anion receptors

Tris(2-aminoethyl)amine (tren), sketched in Scheme 3, is a common scaffold utilized in the molecular design of synthetic receptors for anion recognition. (8, 38-43, 56, 57) This structural unit can be functionalised with several binding groups. In a search performed on the Cambridge Structural Database (CSD),(58) carried out using the tren framework as query, several crystal structures of tren derivatives were found, with a wide range of functional groups such as ureas, thioureas, amides and amines. The results obtained are summarized in Table 7 for the anion receptors incorporating urea and thiourea functional groups. The structures of the receptors are represented in Scheme 4.

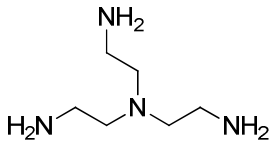

L^3

Scheme 3

Table 7 – Summary of the crystal structures of the associations between tren dericatives and inorganic anions with physiological relevance.

Receptor	*Formula*[*]	*CSD REFCODE*	*Refs.*
L[4]	$L^4_2 \subset (H_2PO_4)_2 \bullet (DMF)_2$	CITYOU	(59)
	$L^4_2 \subset SO_4$	XUFFIO	(60)
	$L^4 \subset F$	XUFFEK	(60)
	$L^4_2 \subset CO_3$	PUSTIH	(61)
L[5]	$L^5_2 \subset SO_4$	DIXWOX, GIYCAT, GIYCUN, GIYDAU, GIYDEY, HOXGIL	(62-64)
	$L^5_2 \subset CO_3$	GIYCIB	(63)
	$L^5 \subset SO_4$	BULLAW, BULKUP, BULLEA	(65)
L[6]	$L^6_2 \subset SO_4(\mu\text{-}H_2O)_3SO_4$	HIJGAJ	(66)
L[7]	$L^7_2 \subset SO_4$	KECHAC	(67)
L[8]	$L^8_2 \subset CO_3$	FUXYED	(68)
L[9]	$L^9_2 \subset SO_4$	FUXYIH	(68)

*The total negative charge of the associations is omitted as well as the counter ions.

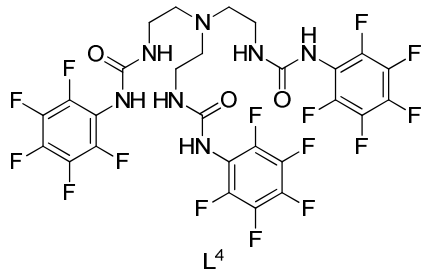

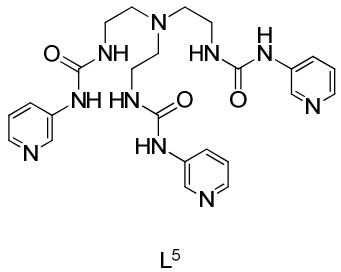

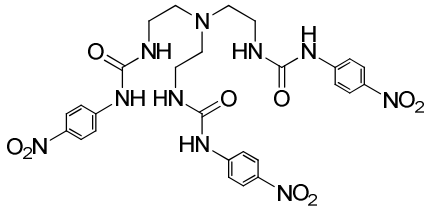

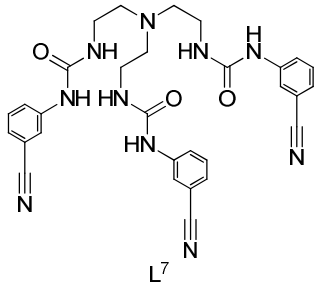

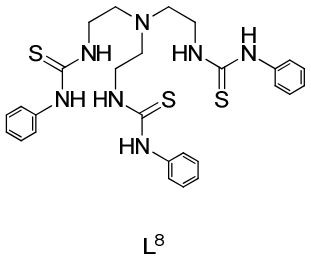

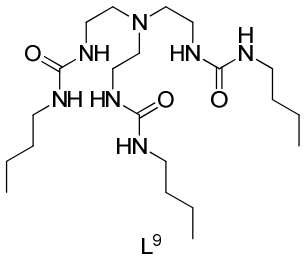

Scheme 4

The data listed in the Table 7 indicate that the polyatomic anions SO_4^{2-} and CO_3^{2-} form with receptors L^4 to L^9 binding associations with a receptor:anion stoichiometry 2:1. The structure of these associations is illustrated in Figure 5 with the crystal structure of $L^8{}_2{\subset}CO_3$. The carbonate anion is surrounded by two L^8 receptors with the oxygen atoms establishing twelve N-H•••O hydrogen bonds with the six thiourea groups leading to N•••O distances between 2.82 and 3.07 Å. However, this family of receptors is also able to recognise simultaneously two polyatomic anions yielding associations with a receptor:anion stoichiometry 2:2. This is the case of $L^4{}_2{\subset}(H_2PO_4)_2{\bullet}(DMF)_2$ (see Figure 6), and $L^6{}_2{\subset}SO_4(\mu\text{-}H_2O)_3SO_4$ (see Figure 7) associations. In the first one, a structural entity composed of two self-assembled phosphate anions and two dimethylformamide (DMF) solvent crystallisation molecules are hydrogen bonded to the urea groups of two L^6 molecules. The N-H•••O distances between the N-H binding sites and the oxygen atoms from the phosphate anions range from 2.75 to 2.98 Å. An equivalent binding arrangement was found for $L^6{}_2{\subset}SO_4(\mu\text{-}H_2O)_3SO_4$, but here the anion unit is composed of two sulphate anions bridged by three water molecules ($\{SO_4(\mu\text{-}H_2O)_3SO_4\}^{4-}$). This large dimeric entity is wrapped by two L^6 receptors through the multiple N-H•••O hydrogen bonds with O•••N distances ranging from 2.87 to 2.90 Å. In contrast, the fluoride, in the association $L^4{\subset}F$ represented in Figure 8, the smallest halogen anion is encapsulated by a single L^4 molecule, forming six strong hydrogen bonds with the three urea binding units, with distances between 2.70 and 2.88 Å. These receptors are able to bind different anions, in different stoichiometries, depending on the anion size species and crystallisation conditions.

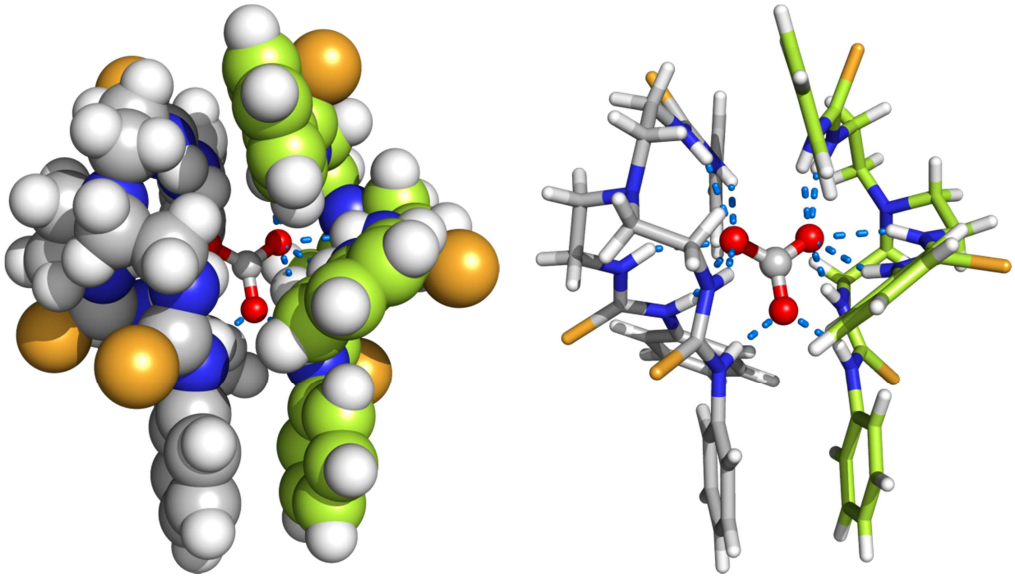

Figure 5 – Crystal structure of $L^8{}_2{\subset}CO_3$ shown in two alternative views. The left representation is a space filling model, displaying the anion encapsulated by two L^8 molecules. In the right view, L^8 is represented in sticks fashion, showing the N-H•••O hydrogen bonds drawn as light blue dashed lines.

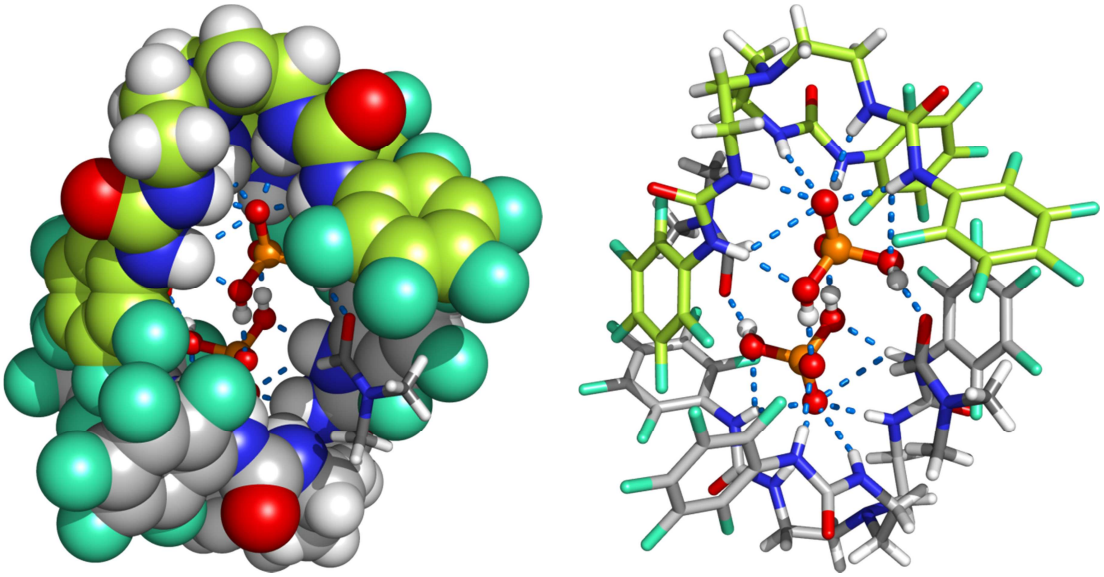

Figure 6 – Crystal structure of $L^4{}_2{\subset}(H_2PO_4)_2{\bullet}(DMF)_2$ shown in two views: in the left view, L^4 is shown in space filling model, emphasising the encapsulation of two $H_2PO_4^-$ anions. The right view, where L^4 is shown in sticks fashion, illustrates the N-H•••O hydrogen bonds, drawn as light blue dashed lines.

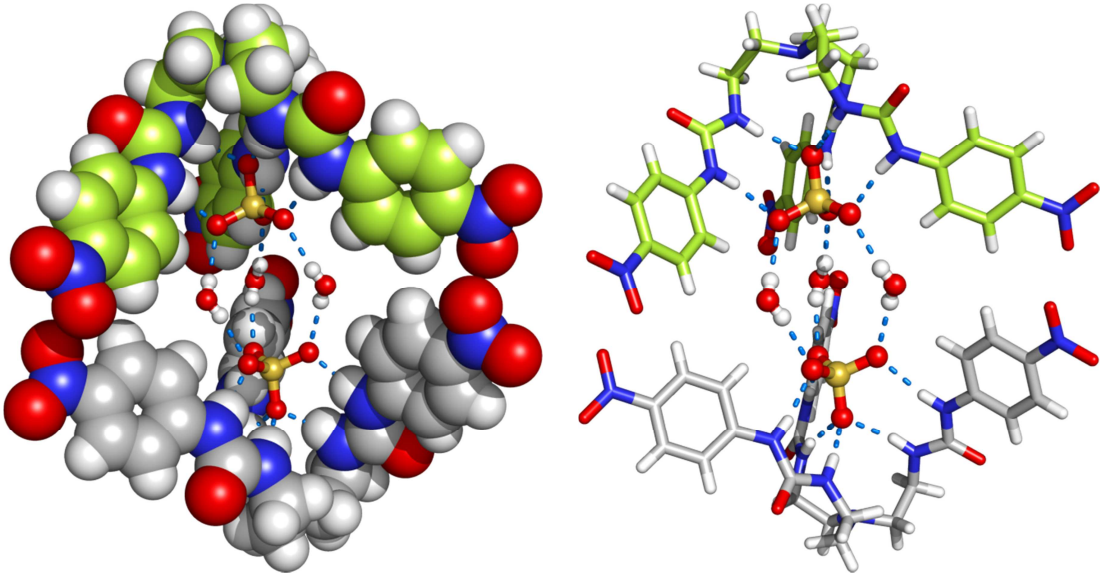

Figure 7 – Crystal structures of $L^6{}_2{\subset}SO_4(\mu\text{-}H_2O)_2SO_4$ shown in two views: In left, L^6 is represented in space filling model, showing the anions' encapsulation, while the right view, with L^6 in sticks model, illustrates the N-H•••O and O-H•••O hydrogen bonds drawn as light blue dashed lines.

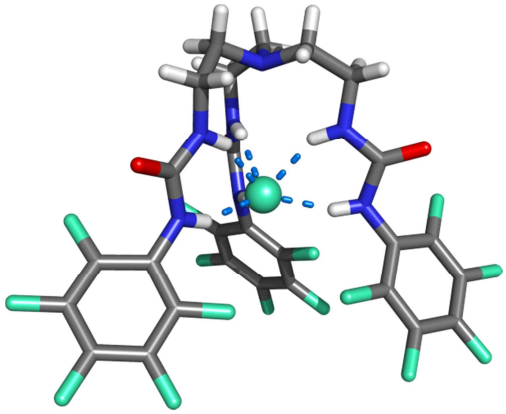

Figure 8 – Crystal structure of $L^4 \subset F$ association, with L^4 represented as sticks and fluoride as a green sphere. Remaining details are given in Figure 5.

Besides the receptors previously shown, the ligands depicted in Scheme 5 also have the ability to transport anions (Cl^- when coupled with H^+ as HCl) across a dichloromethane phase.(69) This ability was demonstrated in the following experiment: receptors L^{10}-L^{17} were dissolved in the organic phase and placed at the base of the U-tube, between one arm with aqueous HCl [pH=0.9] and other arm with deionised water. This experiment clearly shows the transport of HCl across the organic phase when a receptor is present, while no HCl transport was verified in the absence of the mentioned receptors.(69) Davis and co-workers reported tren derivatives incorporating two catechol binding units (see Scheme 6) able to transport anions (Cl^-, Br^-, NO_3^-, I^-, ClO_4^-) across egg-yolk phosphatidylcholine (EYPC) liposomal membranes, with the anion transport rates diminishing in the order $Cl^- > Br^- > NO_3^- > I^- > ClO_4^-$ a sequence similar to the Hofmeister series.(70) Other recent applications of this scaffold include encapsulation of sulphate,(62, 65) and of fluoride, due to the potential use of this anion in medical and biological fields.(60)

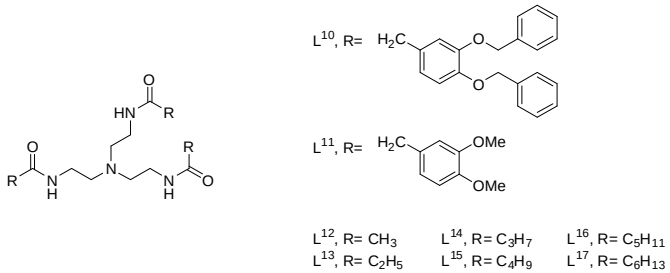

Scheme 5

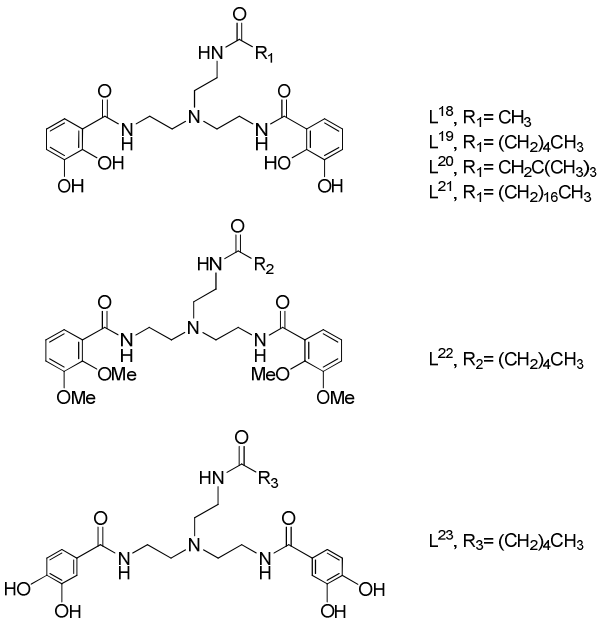

Scheme 6

Gale *et al.* developed two sets of tris-urea (L^{24} and L^{25}) and tris-thiourea (L^{26} and L^{8}) receptors, which are easily synthetized from the tren unit.(68) These receptors are shown in Scheme 4 and in Scheme 7.

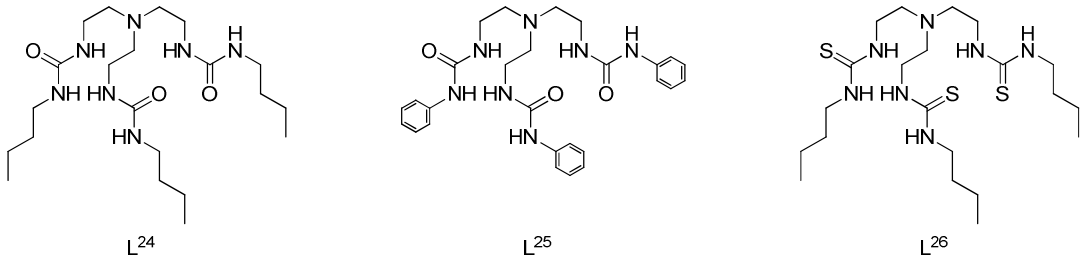

Scheme 7

The binding affinity of these receptors for sulphate, bicarbonate or chloride anions as tetrabutylamonium salts was experimentally evaluated in a deuterated dimethyl sulfoxide/0.5% water (DMSO-d_6/0.5% water) solution through ^{1}H NMR spectroscopy. The experimental stability constants of chloride associations measured for L^{24}, L^{25}, L^{26} and L^{8} were 658, 830, 447 and 191 M^{-1}, in this order. The chloride forms associations with a stoichiometry receptor:anion 1:1, as observed in the solid state structure for $L^4 \subset F$ (see Figure 8), whereas the polyatomic anions preferentially establish associations with the receptor:anion

stoichiometry 2:1 eventually adopting an equivalent binding arrangement to that found in the crystal structure of $L^8{}_2CO_3$ (see Figure 5). These two structures, if assumed in solution, would protect the anion from the solvent medium.(68) This particular feature is investigated in Chapter 2 for chloride associations $L^{26}\subset Cl^-$ and $L^8\subset Cl^-$.

To study the ability of these four receptors to transport chloride across a model membrane, 1-palmitoyl-2-oleoyl-*sn*-glycero-3-phosphocholine (POPC) unilamellar vesicles were prepared, loaded with a solution of sodium chloride and suspended in sodium nitrate solution as described in ref. (68). This experiment showed that L^{24} and L^{25}, incorporating urea binding groups, were less effective, when compared to L^{26} and L^8, with thiourea, to promote chloride transmembranar transport. In addition, when the experiment was run with KCl salt instead of NaCl, to test the cotransport of Na^+/Cl^-, no change in the chloride transport rate was observed, excluding a possible Na^+/Cl^- cotransport mechanism.(68)

On the other hand, equivalent experiments carried out in cholesterol rich vesicles (70% POPC and 30% cholesterol) led to a significant decrease of chloride transport rate. This result indicates that L^{24}, L^{25}, L^{26} and L^8 function as ion carriers (shuttling back and forth within the bilayer), instead of channels. The cholesterol makes the membrane more ordered, *i.e.*, less flexible and fluid,(71) and difficults the in- and out-movement of a carrier. In contrast, a channel would remain at a defined position and consequently the anion transport would be unaffected by the presence of cholesterol.(68)

The transport ability of these receptors for bicarbonate through the POPC bilayer was evaluated thought ^{13}C NMR spectroscopy, following the experimental procedure described in ref. (68). With the addition of sodium bicarbonate, the release of chloride from the vesicles was observed for L^{25}, which was concomitantly accompanied by a moderate chloride/bicarbonate exchange. This activity was significantly enhanced for L^{26} and L^8. In contrast L^{24} showed no activity as chloride/bicarbonate exchanger.

This set of results demonstrate that L^{26} and L^8 promote the release of chloride from POPC vesicles and are effective Cl^-/HCO_3^- exchangers, and they are the rationale for the theoretical investigations (molecular mechanics calculations and molecular dynamics simulations) reported in this thesis. Indeed this work is part of a collaboration project on the research of transmembrane anion transport, between the Gale's group and the Felix's group, and the work presented in thesis is part of this collaboration.

1.4 Molecular Dynamics Simulations of Biomembranes

In this section, the lipid structures commonly utilized in molecular dynamics (MD) simulations to mimic cell membranes are presented together with the typical force fields applied in these simulations. Subsequently, selected examples of the unassisted movement of ions across membranes investigated by MD simulations and reported in the literature are briefly described.

1.4.1 MD simulations of membrane models

The majority of the membrane MD simulations are frequently carried using one of the following types of lipid: 1-palmitoyl-2-oleoyl-*sn*-glycero-3-phosphocholine (POPC),(72) 1,2-dioleoyl-*sn*-glycero-3-phosphocholine (DOPC),(73) 1,2-dipalmitoyl-*sn*-glycero-3-phosphocholine (DPPC),(74) and 1,2-dimyristoyl-*sn*-glycero-3-phosphocholine (DMPC).(75) These lipids are depicted in Scheme 8. All of them are composed of a phosphatidylcholine head, *sn-3* (76) and two acyl chains differing in the length and degree of unsaturation. For instance, POPC presents one saturated acyl chain (*sn-1*, 16:0) and one monounsaturated acyl chain (*sn-2*, 18:1),(77) as seen in Scheme 8.

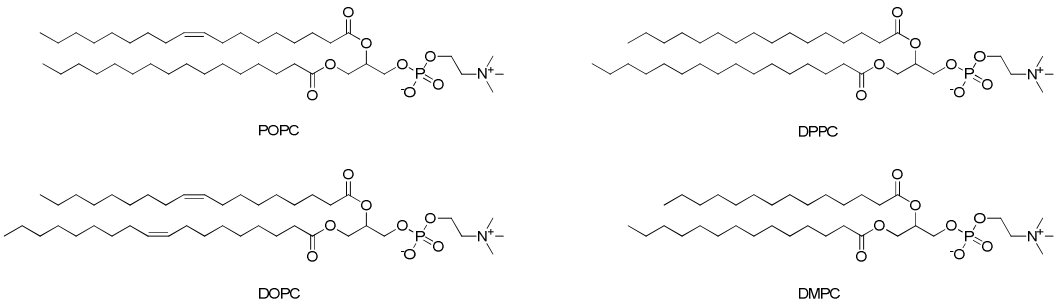

Scheme 8

One major aspect concerning all MD simulations is the employed force field (also known as specific potential function), that represents the interactions between atoms in the simulation system.(78) Several force fields exist,(79) and some are open and have been ported between several simulation software suites. All of them, nonetheless, have advantages and weaknesses, due to the empirical origin of the encoded parameters,(78) and a careful selection of the force field for a specific type of simulation is necessary.

Three types of force fields exist: all-atom; united atom, and coarse-grained. They are distinguished as follows: **all-atom** force fields represent all atoms in the system, including

nonpolar hydrogen atoms. On the other hand, **united atom** force fields explicitly represent polar hydrogen atoms with potential for hydrogen bonding, while nonpolar hydrogen atoms are considered as part of the heavy atoms they are bonded to, resulting in computational performance gains.(80, 81) Likewise, **coarse-grained** force fields do not represent all the atoms in a system, but use coarse particles to represent elements (functional groups or other groups of atoms) of the system. This type of representation is useful in larger systems and/or long simulations, although it yields less detail than the previous types of force fields.(82)

Regarding simulations of systems containing lipid molecules, several force fields have been recently developed. Some of the most preeminent examples are summarized in Table 8.

Table 8 – Examples of the MD simulations with different types of phospholipids and force fields.

Type of force field	*Force field*	*Phospholipids and corresponding refs.*
All-atom	GAFF	POPC (83) DMPC, DOPC (84) DOPC (85)
	CHARMM36	POPC, POPG (86) DPPC, DMPC, DLPC, DOPC, POPC, POPE (87)
United atom	G43A1-S3	DPPC, DMPC, DOPC, DLPC (88)
	$G53A6_L$	DLPC, DMPC, DPPC, DOPC, POPC (89)
Coarse-grained	MARTINI	DPPC, DOPC, DPPE, DOPE (90)

GAFF – General AMBER Force Field
CHARMM – Chemistry at HARvard Molecular Mechanics
MARTINI – MARrink Toolkit INItiative
POPG – 1-palmitoyl-2-oleoyl-*sn*-glycero-3-phospho-rac-(1-glycerol) (91)
DLPC – 1,2-didodecanoyl-*sn*-glycero-3-phosphocholine (92)
POPE – 1-palmitoyl-2-oleoyl-*sn*-glycero-3-phosphoethanolamine (93)
DPPE – 1,2-dipalmitoyl-*sn*-glycero-3-phosphoethanolamine (94)
DOPE – 1,2-dioleoyl-*sn*-glycero-3-phosphoethanolamine (95)

GAFF (General AMBER Force Field) in particular is an all-atom force field and was developed to be employed with the most diversified types of molecules.(84) GAFF has been tested in the MD simulations of bilayers of DOPC, DMPC and POPC lipids (see Table 8). When compared with previous results of PARM94,(84) CHARMM27 force fields and the force field of Berger, in the simulations of DOPC and POPC bilayers,(85) GAFF is able to reproduce most properties of bilayers, including structural and dynamic properties, even when considering the different

lengths and saturations and other properties experimentally verifiable,(84, 85) such as area per lipid.(84) Also, due to its compatibility with protein force fields, GAFF allows the simulation of proteins and other organic molecules embedded in membranes, thus expanding its application.(84, 85) Concerning the simulation of phospholipid bilayers with GAFF, the most prominent limitation is the need for imposition and selection of a suitable surface tension parameter when simulating the fluid phases of such bilayers.(85) In contrast, other force fields (*e.g.*, CHARMM36(87) and G53A6$_L$,(89)) do not require such artifice to accurately reproduce lipid experimental parameters like area per lipid.

Having in mind the experimental work performed by Gale *et al.*(68) information regarding simulations with the POPC lipid was searched. Two relevant works were found:

In 1992, Heller and co-workers have simulated for the first time a membrane-water system composed of 200 POPC lipid molecules and 5483 Transferable Intermolecular Potential 3 Point (TIPS3P) water molecules[†], using the CHARMM force field.(98) They have simulated both an ordered gel phase and a less ordered liquid-crystal phase that has a closer resemblance with the structure of cell membranes. The area per lipid (one easy and reliable parameter to evaluate) for the liquid-crystal phase simulation was of 65.50 ± 0.04 Å. The authors deemed this value as a good result, because at the time, with no experimental parameters of POPC to use as reference, that result could only be compared with the data available for two other structurally close lipids: DPPC (area comprehended between 57.60-70.90 Å^2) and DOPC (area of 60.00 Å^2).(98)

More recently, Martinek and Jójárt have tested GAFF applied to a system with 128 POPC lipid molecules and 2985 Transferable Intermolecular Potential 3 Point (TIP3P) water molecules[†].(83) The capacity of this force field was evaluated in several characteristics of the system, such as area per lipid, order parameter, lateral diffusion coefficients, electron density profile, and bond water at the lipid/water interface. When surface tension was applied, the simulation outputs were in general agreement with available experimental data (*e.g.*, they obtained an area per lipid of 66.8 ± 0.9 Å^2, close to the experimental reference 68.3 ± 1.5 Å^2), thus assuring that this force field was suitable for use with this type of lipid.(83)

[†] Although the expression is the same, TIPS3P and TIP3P water models present different geometry and parameters for potential functions (see section *II. Transferable Intermolecular Potential Functions*, subsection *A. Form and Parameters* in ref. (96) for TIPS3P and *Table I* of ref. (97) for TIP3P).

The work presented in this thesis differentiates from the above simulations in the following features: use of a different water model (extended single point charge – SPC/E), in a system with less lipid molecules,(72) although with higher water:lipid ratios, 31.14 and 68.81, creating the conditions to attempt the reproduction of experimental results by Gale *et al.*(68)

1.4.2 Other applications in the movement of ions and other molecules across biomembranes

The unassisted movement of anions and cations through membranes has also been studied with resort to MD simulations, by Pohorille and Wilson,(99) Gurtovenko and Vattulainen (100) and Wei and Pohorille.(101)

Pohorille and Wilson, in 1996, carried out MD simulations with free sodium and chloride ions in a system using 72 molecules of *glycerol 1-monooleate* as the lipid in a single *bilayer membrane* model and 2304 Transferable Intermolecular Potential 4 Point (TIP4P) water molecules, with a modified version of Optimized Potentials for Liquid Simulations (OPLS) force field**.** Those simulations demonstrated that, while on the aqueous phase, these anions do not cause any perturbation to the properties of the bilayer. On the other hand, as a single ion approaches and enters the membrane, some water molecules and surrounding lipid head groups accompany this movement of the ion. When the ion is in the middle of the bilayer, the opposite phospholipid heads turn to the hydrophobic core, to facilitate the remaining path of the ion and water molecules.(99) These ions have a natural poor permeation (about 8 to 10 orders of magnitude smaller when compared with small neutral molecules), however the understanding of this process is still biologically important.(102)

Gurtovenko and Vattulainen, in 2005, differentiated from the method employed by Phorille and Wilson: the system was setup with a double bilayer of DMPC lipids (256 total), ~10200 Single Point Charge (SPC) water molecules and 40 chloride and 40 sodium ions, with the sodium ions unevenly distributed between the two virtual spaces. These simulations were carried out using the Berger force field. As the MD simulation progressed, a transient water pore formed in one of the bilayers, while the other bilayer was structurally intact. With the pore formation, some water molecules were transported to the other side of the bilayer, as well as Na^+ ions, accordingly to the concentration gradient. It is worth notice that with bigger concentration differences, the diffusion velocity and size of the pore were also increased, diminishing

through time, as equilibrium between the two sides of the membranes was closer of being achieved.(100)

Recently, Wei and Pohorille have attempted the simulation of the permeation of adenine nucleosides through a 142 POPC lipid model bilayer, in a system with 5903 TIP3P water molecules, using the CHARMM force field. During the course of the MD simulations the nucleoside flipping movement while inside the bilayer was observed, to attain favourable positioning to carry on the permeation, as the entry orientation was different from the exit orientation. The authors believe that this mechanism can also explain the permeation behaviour of other large molecules, such as drugs,(101) and might eventually be followed by the synthetic receptors studied in this thesis.

1.5 Aims/Objectives

Considering what has been previously presented, both in the matters of the importance of the development and study of new synthetic transmembranar transporters, as well as the important role of the MD simulations as a tool to better understand these processes at the molecular level, the following major objectives, as well as their sub-objectives, are proposed be accomplished in this work:

1 Evaluate the binding ability of tren-derivative receptors for chloride, using unconstrained molecular dynamics simulations:

1.1 Evaluate the receptor binding preferences towards chloride in gas phase;

1.2 Perform the molecular dynamics simulation of the tren-derivative receptors both in DMSO/water and water solutions and compare the results with previous structural and experimental binding data.

2 Evaluate and compare the structural and dynamic properties of POPC bilayer membrane model using molecular dynamics simulations with experimental and computational data available:

2.1 Perform the molecular dynamics simulation of free POPC model membrane composed of 72 lipids with GAFF force field, to compare with published results.

3 Evaluate the impact of tren-derivative anion receptors in the structural and dynamic properties of the POPC bilayer membrane model using molecular dynamics simulations:

3.1 Perform the molecular dynamics simulation of every receptor, starting inside the bilayer and in the aqueous phase.

2 Structural preferences of the thiourea receptors

This chapter describes the molecular modelling studies performed on L^{26} and L^{8} in the gas phase as well as in DMSO and water solution.

2.1 Association between the receptors and chloride in gas phase

2.1.1 Conformational analysis of the free receptors

Methodology

The molecular mechanics (MM) calculations and MD simulations were carried out with force field parameters taken from the GAFF,(103) within the AMBER (Assisted Model Building and Energy Refinement) software suite,(104) with restrained electrostatic potential (RESP) atomic charges (105) for L^{26} and L^{8}.

The atomic coordinates of L^{8} were obtained directly from the X-ray single crystal structure of carbonate association, deposited at the CSD database (refcode FUXYED, see Table 7 and Figure 5 above). The starting geometry of L^{26} was generated from L^{8} by the replacement of the three phenyl substituents by butyl ones.

Subsequently, the *Avogadro* program (106) was utilized to prepare the inputs for the subsequent structure optimizations in gas phase with *Gaussian 03* (107). The structures were energy minimized at HF/6-31G(d), followed by a Single Point calculation of the Electrostatic Potential (ESP) at the same theory level and using 4 concentric layers for each atom and 6 density points in each layer (using the Gaussian internal options: Pop=MK IOp(6/33=2, 6/41=4, 6/42=6)), for consistency with the GAFF.(103) Subsequently, the atomic charges were calculated by RESP fitting in the *antechamber* (103, 108) tool as described below.

The *Gaussian 03* output of each receptor was utilized as input in *antechamber* to automatically generate a Tripos Mol2 (*mol2*) file comprising the atomic coordinates, GAFF atom types and RESP charges. The atom types were obviously assigned taking into account the atomic connectivities within the molecule. Additionally, a force field modification (*frcmod*) file was created with the missing force field parameters, using the program *parmchk*.(103, 108) At this stage, for each receptor the corresponding *frcmod* file together with GAFF parameter and

mol2 files were loaded into *xLEaP* and the topology and coordinate files required for the subsequent gas phase calculations were generated.

The GAFF is compatible with either the use of RESP (105) or AM1BCC (109, 110) atomic charges. As the majority of the atomic charge models commonly utilized in molecular mechanics and dynamics simulations, these are dependent of the molecular conformation. In this context, with the main goal to obtain atomic charges less dependent of the molecular conformation or orientation, the calculation of the final RESP charges applied in the MD simulations were preceded by conformational analyses on L^{26} and L^{8}, as follows:

The MM energy minimised structure with the initial set of RESP charges was heated in gas phase at 1000 K for 50 ps followed by a collection run of 1 ns, using a time step of 1 fs. The use of this high temperature enables the stochastic search of the conformational space since the energetic barriers are easily surmounted.(111) Frames were saved every 0.1 ps leading to a trajectory file containing 10000 structures. Subsequently, all of these structures were minimised by molecular mechanics using a steepest descendent gradient followed by the conjugate gradient algorithm, until convergence criteria of 0.0001 kcal mol^{-1} $Å^{-1}$ was attained. Afterwards, the frames were energy sorted and the five lowest energy structures with markedly different conformations were appointed for new geometry optimizations and charge calculations as described above. The individual ESP data was directly extracted from the corresponding *Gaussian 03* outputs with *espgen*, and then the ESP data of the five conformations were merged and utilized to generate the input files for the two-stage Restrained Electrostatic Potential fitting with the *resp* program of the AMBER package. This procedure enabled the calculation of RESP charges considering five different conformations for each receptor. The atomic charges for L^{26} and L^{8}, together with the employed atom types, are presented in Table 9 and Table 10, respectively, and the atomic numbering scheme is shown in Scheme 9.

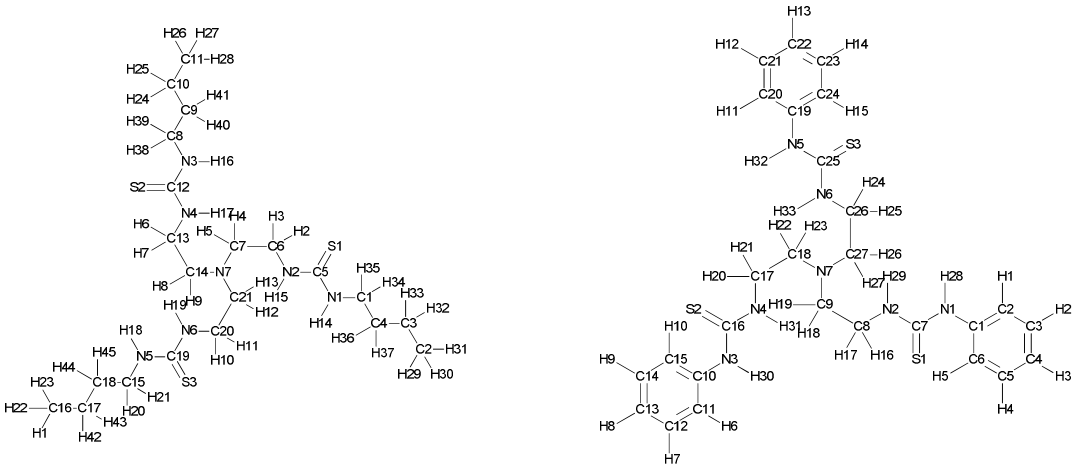

L^{26} L^{8}

Scheme 9

Table 9 – Atom types and RESP charges employed for L^{26}.

ID[a]	*AT*[b]	*Charge*	***ID***[a]	*AT*[b]	*Charge*	***ID***[a]	*AT*[b]	*Charge*	***ID***[a]	*AT*[b]	*Charge*
S1	s	-0.49345	**C10**	c3	0.18171	**H8**	h1	0.06362	**H27**	hc	0.03847
S2	s	-0.49345	**C11**	c3	-0.17397	**H9**	h1	0.06362	**H28**	hc	0.03847
S3	s	-0.49345	**C12**	c	0.24068	**H10**	h1	0.04365	**H29**	hc	0.03847
N1	n	-0.28252	**C13**	c3	0.07889	**H11**	h1	0.04365	**H30**	hc	0.03847
N2	n	-0.34331	**C14**	c3	-0.02416	**H12**	h1	0.06362	**H31**	hc	0.03847
N3	n	-0.28252	**C15**	c3	0.09910	**H13**	h1	0.06362	**H32**	hc	-0.03705
N4	n	-0.34331	**C16**	c3	-0.17397	**H14**	hn	0.21989	**H33**	hc	-0.03705
N5	n	-0.28252	**C17**	c3	0.18171	**H15**	hn	0.32454	**H34**	h1	0.02323
N6	n	-0.34331	**C18**	c3	-0.03622	**H16**	hn	0.21989	**H35**	h1	0.02323
N7	n3	-0.34182	**C19**	c	0.24068	**H17**	hn	0.32454	**H36**	hc	0.01023
C1	c3	0.09910	**C20**	c3	0.07889	**H18**	hn	0.21989	**H37**	hc	0.01023
C2	c3	-0.17397	**C21**	c3	-0.02416	**H19**	hn	0.32454	**H38**	h1	0.02323
C3	c3	0.18171	**H1**	hc	0.03847	**H20**	h1	0.02323	**H39**	h1	0.02323
C4	c3	-0.03622	**H2**	h1	0.04365	**H21**	h1	0.02323	**H40**	hc	0.01023
C5	c	0.24068	**H3**	h1	0.04365	**H22**	hc	0.03847	**H41**	hc	0.01023
C6	c3	0.07889	**H4**	h1	0.06362	**H23**	hc	0.03847	**H42**	hc	-0.03705
C7	c3	-0.02416	**H5**	h1	0.06362	**H24**	hc	-0.03705	**H43**	hc	-0.03705
C8	c3	0.09910	**H6**	h1	0.04365	**H25**	hc	-0.03705	**H44**	hc	0.01023
C9	c3	-0.03622	**H7**	h1	0.04365	**H26**	hc	0.03847	**H45**	hc	0.01023

[a] ID corresponds to the atom number shown in Scheme 9.
[b] AT is the atom type according to GAFF.

Table 10 – Atom types and RESP charges employed for L^8.

ID[a]	*AT*[b]	*Charge*	***ID***[a]	*AT*[b]	*Charge*	***ID***[a]	*AT*[b]	*Charge*	***ID***[a]	*AT*[b]	*Charge*
S1	s	-0.47250	**C9**	c3	0.05509	**C27**	c3	0.05509	**H18**	h1	0.05843
S2	s	-0.47250	**C10**	ca	0.45646	**H1**	ha	0.20018	**H19**	h1	0.05843
S3	s	-0.47250	**C11**	ca	-0.36225	**H2**	ha	0.13548	**H20**	h1	0.06071
N1	n	-0.44863	**C12**	ca	-0.05168	**H3**	ha	0.15515	**H21**	h1	0.06071
N2	n	-0.24081	**C13**	ca	-0.21685	**H4**	ha	0.13548	**H22**	h1	0.05843
N3	n	-0.44863	**C14**	ca	-0.05168	**H5**	ha	0.20018	**H23**	h1	0.05843
N4	n	-0.24081	**C15**	ca	-0.36225	**H6**	ha	0.20018	**H24**	h1	0.06071
N5	n	-0.44863	**C16**	c	0.22678	**H7**	ha	0.13548	**H25**	h1	0.06071
N6	n	-0.24081	**C17**	c3	-0.00402	**H8**	ha	0.15515	**H26**	h1	0.05843
N7	n3	-0.51688	**C18**	c3	0.05509	**H9**	ha	0.13548	**H27**	h1	0.05843
C1	ca	0.45646	**C19**	ca	0.45646	**H10**	ha	0.20018	**H28**	hn	0.28094
C2	ca	-0.36225	**C20**	ca	-0.36225	**H11**	ha	0.20018	**H29**	hn	0.29894
C3	ca	-0.05168	**C21**	ca	-0.05168	**H12**	ha	0.13548	**H30**	hn	0.28094
C4	ca	-0.21685	**C22**	ca	-0.21685	**H13**	ha	0.15515	**H31**	hn	0.29894
C5	ca	-0.05168	**C23**	ca	-0.05168	**H14**	ha	0.13548	**H32**	hn	0.28094
C6	ca	-0.36225	**C24**	ca	-0.36225	**H15**	ha	0.20018	**H33**	hn	0.29894
C7	c	0.22678	**C25**	c	0.22678	**H16**	h1	0.06071			
C8	c3	-0.00402	**C26**	c3	-0.00402	**H17**	h1	0.06071			

[a] ID corresponds to the atom number shown in Scheme 9.
[b] AT is the atom type according to GAFF.

The final results of those charge calculations with *resp* program were utilized to replace the charges automatically attributed by *antechamber* in each lowest-energy receptor *mol2* file. Those *mol2* files were later employed as inputs in *LEaP* to generate the proper AMBER topology and coordinate files for all MM calculations and MD simulations reported in this chapter. The described process is illustrated in the flow chart present in Figure 9:

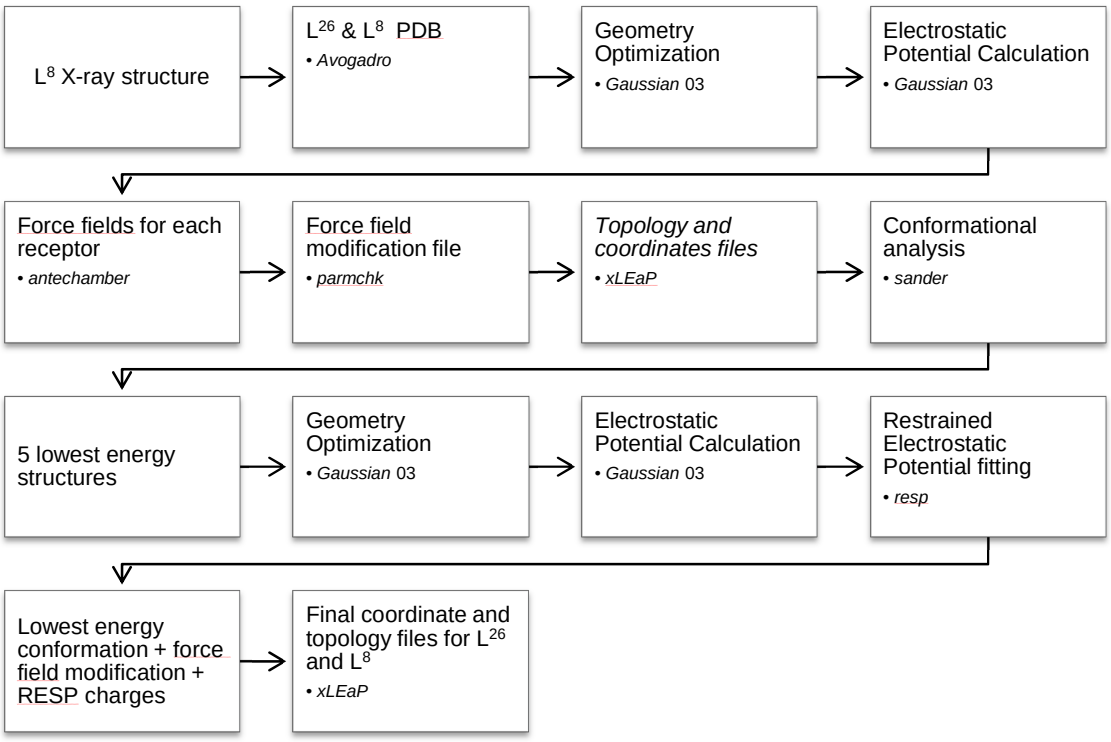

Figure 9 – Diagram for the receptor preparation before MM calculations and MD simulations.

Results and discussion

The conformational analysis of the free and chloride associated receptors (see below) relied on the assessment of the torsion angles defined in Scheme 10. The first four torsion angles (θ, κ, λ and μ) are defined by consecutive sets of three bonds, starting in tertiary nitrogen atom and finishing in the first carbon atom after the thiourea group. Each chain starting at the tertiary nitrogen atom is identified as 1, 2 or 3. Hence, the identification of a certain torsion angle is given by, *e.g.*, κ_2 for angle κ in chain 2. In addition, a fifth torsion angle φ, defined by the atoms H-N•••N-H, is utilized to characterise the configuration adopted by the thiourea binding units, taking values close of ±180º and 0º for *anti* and *syn* configurations, respectively.

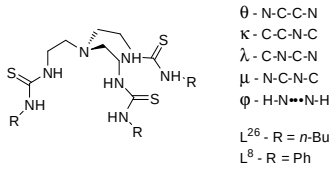

Scheme 10

The conformational analysis of L^{26} by quenched dynamics yielded 10000 conformations in a wide energy range of 38.83 kcal/mol, as consequence of the conformational flexibility exhibited by the three tren thiourea substituents. Five low energy conformations labelled from (***a***) to (***e***) with markedly different structures were selected for the subsequent analysis. These conformations are presented in Figure 10, while their relative energies along with the corresponding torsion angles are listed in Table 11, showing that those are substantially different.

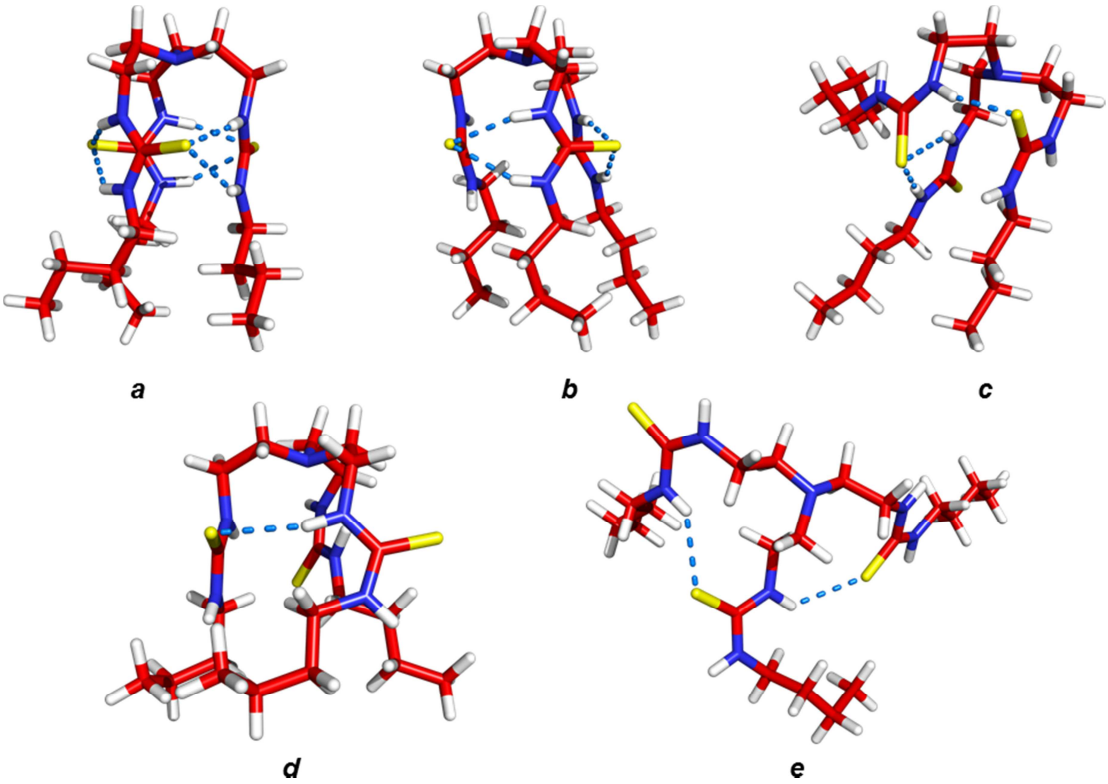

Figure 10 – Five lowest energy conformations found in conformational analysis of L^{26}. The N-H•••S hydrogen bonds are drawn as blue dashed lines.

Table 11 – MM energy (kcal/mol) and torsion angles (º) for five conformations of L^{26}, along with configurations assumed by the thiourea unit.*

Conf	*ΔE*	*Chain 1*					*Chain 2*					*Chain 3*					*Thiourea unit*	
		θ_1	κ_1	λ_1	μ_1	φ_1	θ_2	κ_2	λ_2	μ_2	φ_2	θ_3	κ_3	λ_3	μ_3	φ_3	*Syn*	*Anti*
a	0	-59.9	127.7	168.9	-166.1	-4.4	-58.6	120	-179.7	-163.7	-6.3	-59.7	127.7	173.5	-173.8	-2.8	3	0
b	0.14	-70.4	172.7	171.4	1	179.8	-60.9	123.8	-176.7	-176.5	-3.5	-60.7	119.5	-174.3	176.7	-4.1	2	1
c	3.5	50.1	-117.8	-8.5	1.5	-172.5	58.8	171.9	-170.7	-179.5	179.4	57	-105.9	171	171.2	1.9	1	2
d	11.91	51	78.9	168.4	-172.6	-177.3	54.8	92.2	168.7	-5.3	176	85.5	-91.8	6.6	0.6	179.4	0	3
e	20.56	152.4	-89.3	-178.9	-177.1	-173.8	171	88.8	-178.8	0.5	-179.9	-174.8	91.6	7.2	-3.6	175.9	0	3

* In agreement with Scheme 10, θ, κ, λ and μ represent the torsion angles N-C-C-N, C-C-N-C, C-N-C-N and N-C-N-C respectively. φ represents the torsion angle H-N•••N-H in the thiourea unit.

The lowest energy conformation (***a***) presents a tren organized architecture, with the three thiourea substituents displaying comparable torsion angles. This conformation is stabilized by six intramolecular N-H•••S hydrogen bonds derived from the synergetic interaction between adjacent *syn* thiourea binding groups (see Figure 10 ***a***). The next low energy conformation (***b***) is only 0.14 kcal/mol above, with one thiourea group changing from *syn* to *anti* configuration and only four hydrogen bonds are observed, but the tripodal shape is still conserved. The next low conformation (***c***) has two *anti* thiourea groups and the number of N-H•••S bonding interactions is reduced to three, being this structure energetically disfavoured by 3.50 kcal/mol. In conformation (***d***) all of the three thiourea groups are *anti*, leading to the formation of a single hydrogen bond. The conformation (***e***) exhibits three thiourea groups in *anti* configuration and is disfavoured by 20.56 kcal/mol being, therefore, very unlikely. Indeed, in this conformation the three chains are not involved in any intramolecular stabilising bonding interactions. The dimensions of the intramolecular hydrogen bonds are given in Table 12.

Table 12 – Number and dimensions of N-H•••S hydrogen bonds found in conformations of L^{26} and L^{8}.

Receptor	*Conformation*	*Number of hydrogen bonds*	*Distance N•••S (Å)*		*Angle N-H•••S (º)*	
			Min	Max	Min	Max
L^{26}	***a***	6	3.20	3.60	136	159
	b	4	3.20	3.30	143	162
	c	3	3.20	3.60	146	176
	d	1	3.60	3.60	165	165
	e	2	3.40	3.50	128	138
L^{8}	***a***	6	3.30	3.40	146	149
	b	4	3.20	3.40	149	159
	c	3	3.20	3.40	152	165
	d	2	3.30	3.60	148	154
	e	1	3.60	3.60	132	132

The conformations of L^{8} accessed by the conformational analysis were in the wide energy range of 37.78 kcal/mol. The five lowest energy conformations with notable structural differences were appointed for the current discussion and are also labelled from (***a)*** to (***e***) in Figure 11. Table 13 lists their MM relative energies with selected torsion angles for the three tren bond chains, which show that these conformations are markedly different. The lowest

energy conformation (***a***) displays an organised structure stabilised by six intramolecular N-H•••S hydrogen bonds between immediate thiourea binding groups. The next conformation (***b***) in energy occurs 1.40 kcal/mol above, with two aromatic rings exhibiting an almost parallel arrangement at an interplanar distance of 3.95 Å, suggesting the existence of favourable π-π stacking interactions. In this conformation (***b***), with one *anti* thiourea group, the number of N-H•••S hydrogen bonds formed is four. Similar to L^{26}, the third conformation (***c***) with a relative energy of 2.56 kcal/mol, displays a single *syn* thiourea, forming three N-H•••S hydrogen bonds. The following energy conformation (***d***) exhibits three *anti* thioureas and two hydrogen bonds. The last presented conformation (***e***) also has three *anti* thioureas, but only a single weak hydrogen bond is formed, with a N•••S distance of 3.6 Å and an N-H•••S angle of 132º. In addition, this structure is energetically disfavoured by 19.9 kcal/mol. The hydrogen bonds dimensions for all five conformations are collected in Table 12.

Both lowest energy conformations of L^{26} and L^{8} were subsequently applied in conformational analysis of the $L^{26}\subset Cl^-$ and $L^{8}\subset Cl^-$ associations.

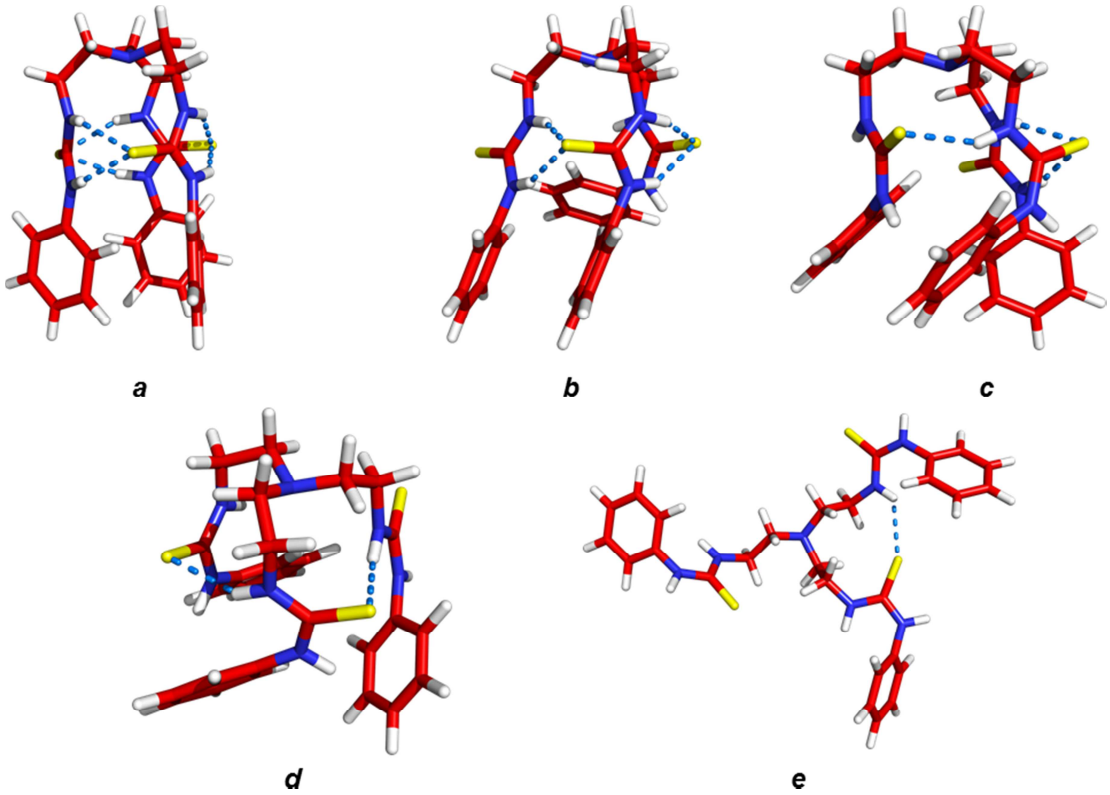

Figure 11 – Five lowest energy conformations found in conformational analysis of L^{8}. The N-H•••S hydrogen bonds are drawn as blue dashed lines.

Table 13 – MM energy (kcal/mol) and torsion angles (º) for five conformations of L^8, along with configurations assumed by the thiourea unit.*

Conf	*ΔE*	*Chain 1*					*Chain 2*					*Chain 3*					*Thiourea unit*	
		θ_1	κ_1	λ_1	μ_1	φ_1	θ_2	κ_2	λ_2	μ_2	φ_2	θ_3	κ_3	λ_3	μ_3	φ_3	*Syn*	*Anti*
a	0	63.4	-139.9	-168.5	171.2	-0.6	63.3	-140	-168.4	171.2	-0.6	63.3	-139.9	-168.4	171.2	-0.6	3	0
b	1.4	65.9	-116.3	-176.3	177.8	-0.9	67.8	-176	-177	-2	170.2	58.7	-123.9	172.6	179.7	4.2	2	1
c	2.56	-56.5	108.4	-175.2	174	-8.8	-55.6	141	174.1	-1.4	179.8	-71.6	168.6	178.6	-5	173.4	1	2
d	3.97	-58.9	106.1	-174.4	-5	177	-49.8	115.3	-179.7	2.5	-178.4	-67.2	164.4	172.3	-10.3	164.3	0	3
e	19.9	178.9	-89.4	-179.9	0.8	176.8	-158.5	86.8	178.3	-1.8	175.4	-160.6	-85.7	-179.5	-2.3	174.1	0	3

* Details as given in Table 11.

2.1.2 Conformational analysis of chloride associations

Methodology

The conformational analysis on the L^{26} and L^{8} chloride associations were performed using the quenched dynamics approach described in the previous section for the free receptors. The chloride charge was set to -1, and was described with the van der Waals parameters developed to be employed with the SPC/E water model.(112) The interactions between the receptors and the anion were described by electrostatic and van der Walls interactions.

Results and discussion

As with the free receptors, 10000 conformations were generated for each anion association, thus ensuring a random and comprehensive search of the conformational space.

The five lowest energy structures found in conformational analysis carried with L^{26} chloride association are depicted in Figure 11 while the corresponding selected torsion angles together with their relative MM energies are presented in Table 14. Dimensions of hydrogen bonds between L^{26} and the anion are listed in Table 15. In the lowest energy conformation, the L^{26} wraps the chloride anion which is tightly bonded *via* six N-H•••Cl^- hydrogen bonds to the three *syn* thiourea groups. The second lowest-energy conformation (***b***) in the energy ranking, disfavoured by 4.17 kcal/mol, presents the three thiourea chains organised around the chloride as observed in conformation ***a***. However one thiourea adopts an *anti* configuration and the anion is bonded by five N-H•••Cl^- hydrogen bonds only. The third conformation (***c***) occurs in the energy ranking only at 11.93 kcal/mol with two thiourea binding groups exhibiting an *anti* configuration and consequently the number of hydrogen bonds favouring this binding arrangement is reduced to three. In the last two conformations (***d***) and (***e***), the three thiourea groups are *anti*, differing mainly in the conformational disposition of individual chains. In both cases, the chloride is hydrogen bonded to L^{26} by two N-H•••Cl^- bonding interactions. These conformations present relative energies of 20.97 kcal/mol for (***d***) and 25.09 kcal/mol for (***e***), and are very unlikely.

Table 14 – MM energy (kcal/mol) and torsion angles (º) for five conformations of $L^{26}\subset Cl^-$, along with configurations assumed by the thiourea unit.*

Conf	*ΔE*	*Chain 1*					*Chain 2*					*Chain 3*					*Thiourea unit*	
		θ_1	κ_1	λ_1	μ_1	φ_1	θ_2	κ_2	λ_2	μ_2	φ_2	θ_3	κ_3	λ_3	μ_3	φ_3	*Syn*	*Anti*
a	0	-53.3	-177.1	-176.6	-179	-0.1	-48.4	162.9	-170.4	177.8	-0.7	-51.6	-171.7	-176.4	170	-2	3	0
b	4.17	-50	162.4	-174.1	-1.7	-180	-54.7	-159.9	-177.2	170.4	-2	-80.8	-90.2	174.9	179.4	-0.7	2	1
c	11.93	68.2	80.7	-174.3	-0.7	179.5	65.5	172.5	-174.6	-0.4	-178	69.5	122.5	-171.4	175.5	0.7	1	2
d	20.97	58.3	-160.1	12.2	-0.2	177.7	-85	167.5	-178.7	-178.8	-164.1	-62.3	-83.8	178.5	-0.9	-177	3	0
e	25.09	-164	86.5	-4.8	0	-179.4	-160.9	-87.8	178	-178.5	177.2	-152.7	-90.3	-179.7	-2.7	-178.5	3	0

* Details as given in Table 11.

Table 15 – Number and dimensions of N-H•••Cl^- hydrogen bonds found in conformations of L^{26} and L^8 chloride associations.

Associtaion	*Conformation*	*Number of hydrogen bonds*	*Distance N•••Cl^- (Å)*		*Angle N-H•••Cl^- (º)*	
			Min	Max	Min	Max
$L^{26}\subset Cl^-$	***a***	6	3.40	3.40	159	163
	b	5	3.30	3.50	157	163
	c	3	3.30	3.40	158	160
	d	2	3.40	3.60	162	168
	e	2	3.40	3.40	154	157
$L^8\subset Cl^-$	***a***	6	3.30	3.80	151	173
	b	5	3.40	3.60	141	173
	c	3	3.40	3.50	138	161
	d	2	3.30	3.40	159	167

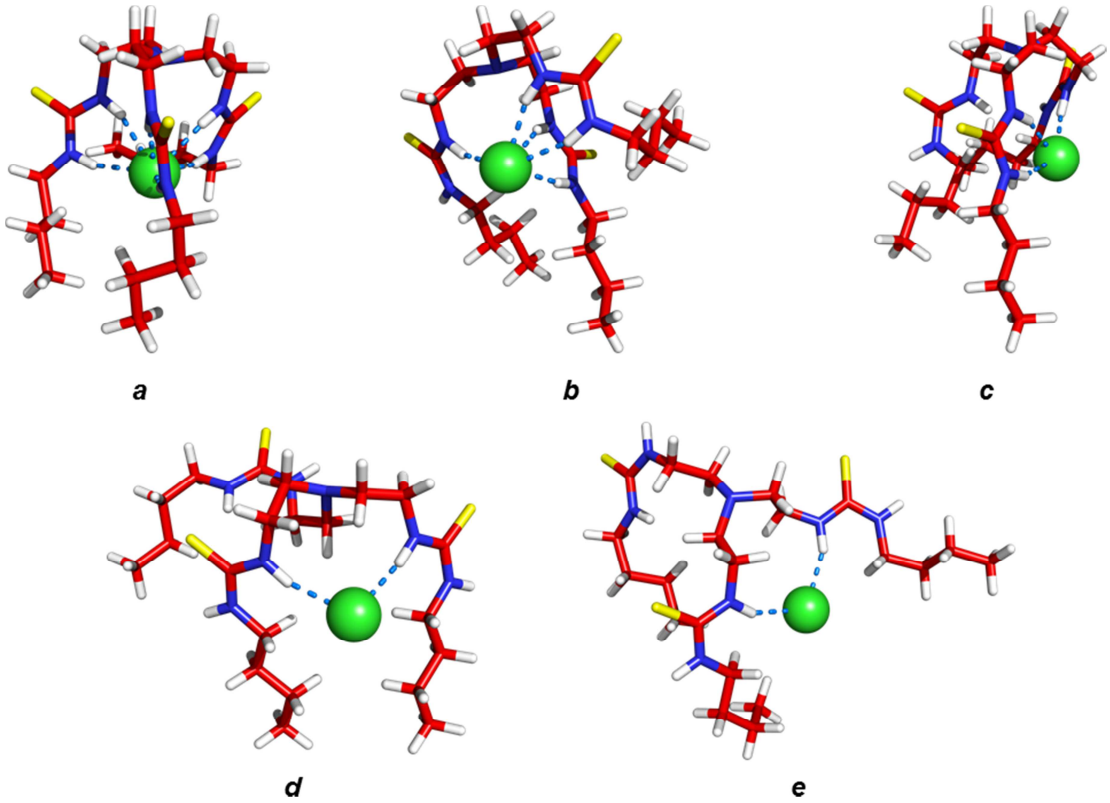

Figure 12 – Five lowest energy conformations found in conformational analysis of $L^{26}\subset Cl^-$ showing remarkable structural differences. The N-H•••Cl^- hydrogen bonds are drawn as blue dashed lines.

The lowest energy conformations found for L8⊂Cl- in conformational analysis are shown in Figure 13. Table 16 lists their relative energies as well the selected torsion angles utilized to describe these conformations. In the lowest energy conformation, similar to observations for L26, the three syn thiourea units surround the chloride, with the six N-H binding sites forming six hydrogen bonds with the anion. The dimensions of these bonding interactions are also listed in Table 15. This binding arrangement is comparable to that found in the crystal structure of the association between fluoride and related receptor L^4⊂F (see *Application of the tren unit in the design of anion receptors*), in which the smallest halogen anion is encapsulated. The next low energy conformation (***b***) with a relative energy of 4.76 kcal/mol has one *anti* thiourea binding unit, leading to five independent N-H•••Cl^- hydrogen bonds. The third and fourth conformations in the energy ranking present a single *syn* thiourea configuration and L^8 is able to form with chloride only three N-H•••Cl^- hydrogen bonds in ***c*** and two in (***d***). In these circumstances, the organized structure of L^8 around the anion is lost as evident in Figure 13 (***c***) and (***d***). These two conformations are largely disfavoured in MM energy (see Table 16) and have different conformational shapes: L^8 is folded in (***c***), while in (***d***) it adopts an open conformation. Chloride associations with three thiourea groups assuming *anti* configurations were not observed in the conformational analysis.

The lowest energy conformations found for L^{26} and L^8 chloride associations were employed in the subsequent DMSO/water and water simulations, as well as in the simulations with membrane setups later.

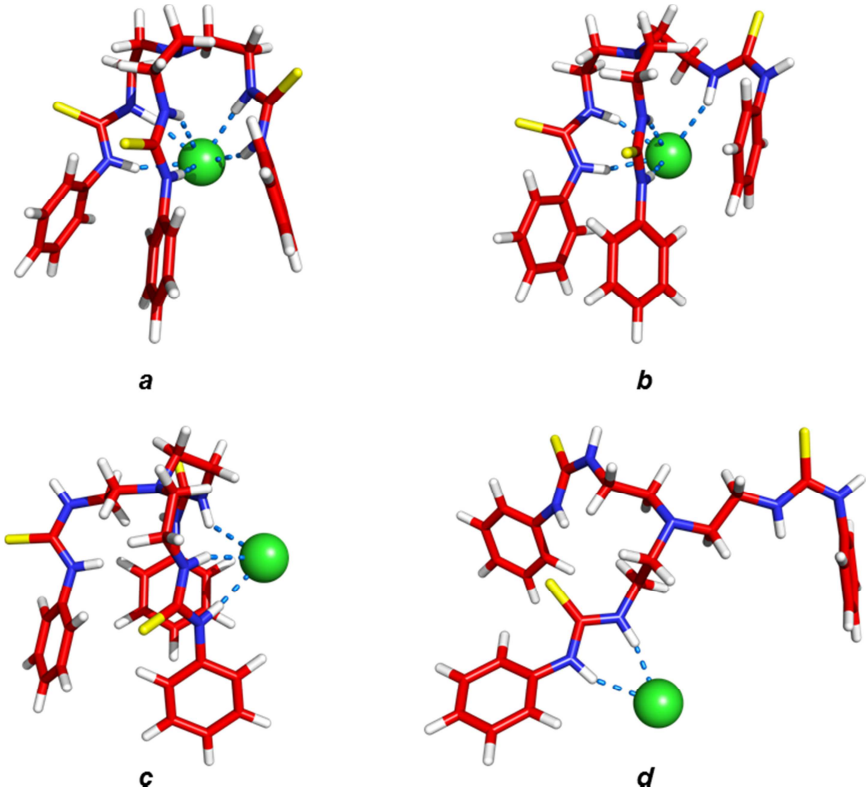

Figure 13 – Four lowest energy conformations found in conformational analysis of $L^8 \subset Cl^-$ showing remarkable structural differences. The N-H•••Cl^- hydrogen bonds are drawn as blue dashed lines.

Table 16 – MM energy (kcal/mol) and torsion angles (º) for five conformations of $L^{8}\subset Cl^{-}$, along with configurations assumed by the thiourea unit.*

Conf	*ΔE*	*Chain 1*					*Chain 2*					*Chain 3*					*Thiourea unit*	
		θ_1	κ_1	λ_1	μ_1	φ_1	θ_2	κ_2	λ_2	μ_2	φ_2	θ_3	κ_3	λ_3	μ_3	φ_3	*Syn*	*Anti*
a	0	44.3	-130.7	169.4	178	-2.9	60.2	87.1	-173.7	-172	5	50.1	166.4	178.7	172.7	-3.4	3	0
b	4.76	63.6	93.8	-170.9	178.2	4.9	-55.6	-84.1	172	175.3	-4.1	49	169.7	176	-4.4	179.6	2	1
c	13.72	60	-168.3	-177.9	6.3	-176.6	172.8	-91.5	5.3	179.6	2.6	54.3	80.5	-171.1	179.4	-175.2	1	2
d	28.13	-178.3	94	8.2	177.6	0.9	172.5	-178.7	179.4	-177	-176.3	179.6	84.5	175.8	-0.9	175	1	2

* Details as given in Table 11.

2.2 Molecular Dynamics Simulations in solution

The binding affinity of L^{26} and L^{8} for chloride as tetrabutylamonium (TBA) salt was experimentally evaluated in DMSO/water solution (v/v 99.5:0.5 solvent mixture ratio) by NMR titrations.(68) Therefore, the dynamic behaviour of chloride associations was investigated by means of unconstrained MD in DMSO/water solution consistent with the experimental conditions and in water.

Methodology

The $L^{26}\subset Cl^-$ and $L^{8}\subset Cl^-$ associations were solvated in *Packmol* (113) with 757 DMSO molecules and 15 SPC/E water molecules, to reproduce as well as possible the solvent medium utilized in the experimental binding studies. Chloride charge was set to -1 and the charge neutrality of both cubic boxes was achieved by the subsequent addition of one TBA cation with a total charge of +1. The force field parameters and atomic charges for DMSO were taken from ref. (114). The TBA was described with the GAFF parameters and RESP charges, as in a previous work of the group.(115) The AMBER force fields were originally developed considering a TIP3P water molecule.(116) This is the historical reason why most of the standard simulations reported in literature, carried out with AMBER, use this water model. The SPC/E water model was appointed in this work for consistency reasons with simulations performed with the phospholipid bilayer membrane model of employed in the MD investigations reported in Chapter 3.

The associations between L^{26} and L^{8} and chloride anion were described by electrostatic and van der Waals interactions with parameters for the anion developed to be utilized along with the SPC/E water model, taken from the ref. (112), as implemented in AMBER11.

Afterwards, each solvated system was equilibrated under periodic boundary conditions using the following multi-stage protocol: The equilibration process starts with minimization of the solvent molecules by molecular mechanics keeping the chloride association and the TBA counter ion fixed by the application of a positional restrain of 500 kcal mol^{-1} $Å^{-2}$. In this step, the eventual bad contacts between the solute and solvent molecules were removed. Subsequently the entire system was relaxed minimizing the energy by molecular mechanics after removal of the positional restrain. The system was then heated at 300 K for 50 ps using a NVT ensemble and a weak positional restraint of 10 kcal mol^{-1} $Å^{-2}$ on the solute. The positional restrain was removed and then equilibration process proceeded in a NPT ensemble for 300 ps at 300 K. At this stage, the density of each system was 1.12 g/cm^3 for both systems during the last 200 ps, remaining constant until the end of this run in close agreement with experimental value for DMSO solution (1.10 g/cm^3). The equilibrated cubic boxes with an edge of 44.76 and 44.66 Å

were obtained for L^{26} and L^{8} systems respectively. NPT data production run (300 K, 1 atm) was carried for each system, during 15 ns. The bath temperature was maintained with Langevin thermostat.(117) The covalent bonds to the hydrogen atoms were constrained with SHAKE algorithm (118) permitting the use of 2 fs time step. The Particle Mesh Ewald (PME) method (119) was utilized to treat the long-range electrostatic interactions and the non-bonded van der Waals interactions were truncated with a 12 Å cut-off.

For water simulations, a cubic box composed of $L^{26}\subset Cl^{-}$ or $L^{8}\subset Cl^{-}$ together with TBA counter ion was solvated with 3970 SPC/E model water molecules, and then were submitted to a multi-stage equilibration protocol identical to the previously described for the simulations carried out in DMSO/water solution. At the end of the equilibration process the value density for both systems was 1.00 g/cm^3, a value within the experimental density for a water solution (1.00 g/cm^3). At the end of equilibration, each cubic box had an edge of 49.31 and 49.36 Å, for the systems where L^{26} and L^{8} were solvated, in this order. NPT data collection runs of 15 ns were carried out for both systems.

For all systems, resulting frames were saved every 0.2 ps, leading to a trajectory file with 75000 frames. The collected data were analysed with the *ptraj* module as implemented in the AMBER11 software package.(104) The molecular diagrams were drawn with *PyMOL*.(120)

Results and discussion

The dynamic structural behaviour of L^{26} and L^{8} chloride associations were investigated in DMSO solution by molecular dynamics simulations for 15 ns. The evolution of the distance between the chloride anion and the centre of mass of the receptor ($Cl^{-}\bullet\bullet\bullet N_c$), defined by the atomic coordinates of the six thiourea nitrogen atoms, throughout the course of the MD simulation is plotted in Figure 14 for the two anion associations. In both cases, during most of the simulation time, the chloride is kept inside the receptor binding pocket, leading to $Cl^{-}\bullet\bullet\bullet N_c$ average distances of 1.35 ± 0.17 and 1.40± 0.16 Å for L^{26} and L^{8} associations, respectively. This feature is clearly illustrated in Figure 15, which represents the 3D histogram built with the atomic positions occupied by the chloride anion throughout the course of the MD simulations carried out with $L^{26}\subset Cl^{-}$ and $L^{8}\subset Cl^{-}$.

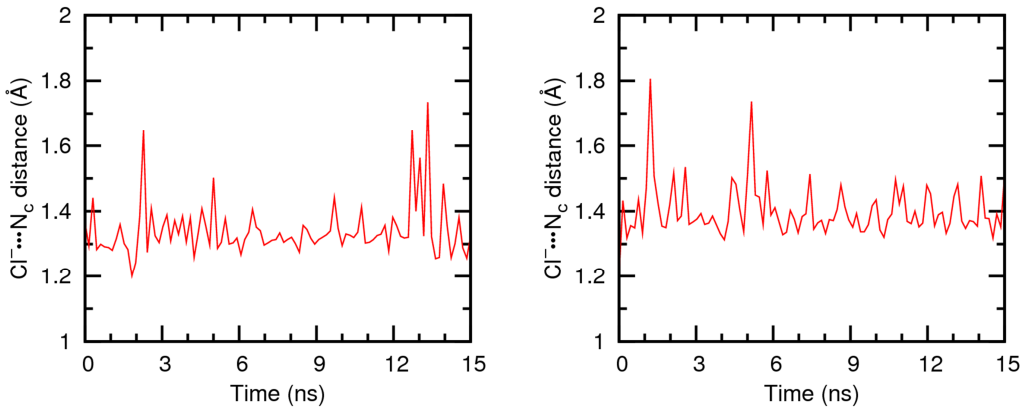

Figure 14 – Evolution of the $Cl^{-}\bullet\bullet\bullet N_c$ distance of L^{26} (left) and L^{8} (right) for 15 ns of the MD simulation carried out in DMSO solution. Data was smoothed with Bézier curves.

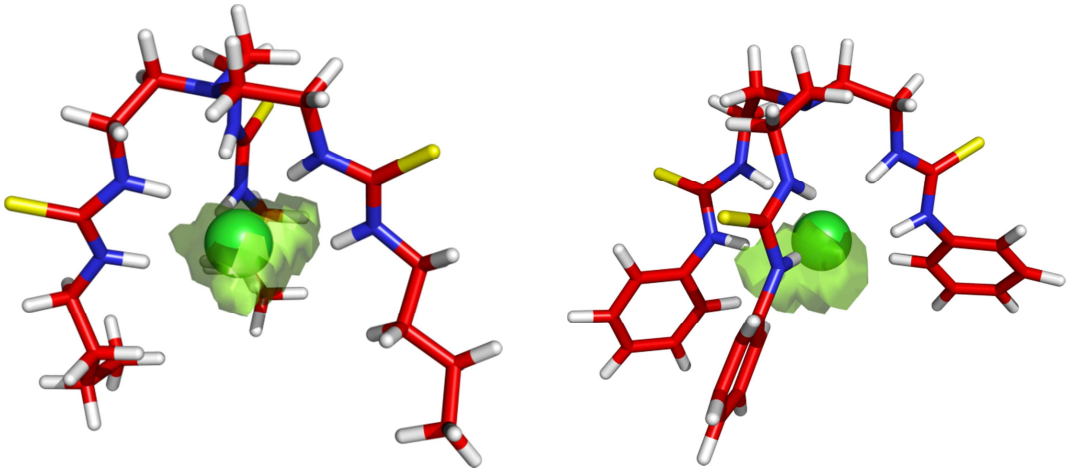

Figure 15 – Histograms built with all positions occupied by the chloride anion when associated with receptors L^{26} (left view) and L^{8} (right view) for 15 ns. The receptor structure presented corresponds to the starting binding arrangement.

A further structural insight into anion associations in solution is given by the analysis of the hydrogen bond parameters, which are given in Table 17.

Table 17 – Dimensions of the parameters of N-H•••Cl^- hydrogen bonds with the standard deviations for L^{26} and L^8 chloride associations in DMSO.

Dimension	*Binding site*	*L^{26}*			*L^8*		
		Min (Å)	Max (Å)	Mean ± Std Dev (Å)	Min (Å)	Max (Å)	Mean ± Std Dev (Å)
Distance	N1•••Cl^-	3.03	4.43	3.46 ± 0.15	2.98	4.48	3.40 ± 0.14
	N2•••Cl^-	2.99	4.59	3.42 ± 0.14	3.02	4.67	3.46 ± 0.15
	N3•••Cl^-	3.01	4.81	3.46 ± 0.15	3.01	4.80	3.39 ± 0.13
	N4•••Cl^-	3.01	4.61	3.42 ± 0.14	3.02	4.74	3.46 ± 0.15
	N5•••Cl^-	3.03	4.60	3.46 ± 0.15	3.01	4.35	3.39 ± 0.13
	N6•••Cl^-	2.99	4.49	3.42 ± 0.14	3.00	4.51	3.45 ± 0.14
Angle	N1-H•••Cl^-	109	180	156 ± 8	116	180	160 ± 8
	N2-H•••Cl^-	113	180	159 ± 7	111	180	156 ± 7
	N3-H•••Cl^-	111	180	156 ± 8	110	180	160 ± 8
	N4-H•••Cl^-	114	180	159 ± 7	116	180	156 ± 7
	N5-H•••Cl^-	113	180	156 ± 8	115	180	160 ± 8
	N6-H•••Cl^-	116	180	159 ± 7	112	180	156 ± 7

These values are based on 75000 observations for each system.

The N•••Cl^- distances and N-H•••Cl^- angles show that the chloride is hydrogen bonded to the three thiourea groups of both receptors in DMSO/water solution. Furthermore, the maximum values of N•••Cl^-, typically above 4.0 Å, indicate that some of these cooperative hydrogen bonds are occasionally interrupted, as clearly indicated by the individual occupancies above 60%, as can be seen in Table 18. Really, the small standard deviations values found for N•••Cl^- distances show that during most of the simulation time the chloride anion is firmly bonded to all six N-H thioureas binding sites, shielded by the receptor from DMSO solvent molecules as illustrated in Figure 15 for L^{26} and L^8.

Table 18 – Hydrogen bond occupancy for receptors L^{26} and L^{8}.

Binding site	*Occupancy (%)**	
	L^{26}	L^{8}
N1-H•••Cl^-	64.6	80.0
N2-H•••Cl^-	74.6	65.2
N3-H•••Cl^-	65.1	81.0
N4-H•••Cl^-	74.3	64.0
N5-H•••Cl^-	64.5	80.7
N6-H•••Cl^-	74.2	66.4

* The percentage of time the hydrogen bond is formed over the trajectory of the MD simulation, with a cut-off for N•••Cl^- distance and N-H•••Cl^- angles of 3.5 Å and 120º, respectively.

The evolution of Cl^-•••N_c distances for simulations carried in water solution with L^{26} and L^{8} is plotted in Figure 16, showing that the chloride anion leaves the receptor binding pocket at about 90 ps of production run until the end of the simulation time in the system with L^{8}, while in the system with L^{26} this event occurs even during the equilibration stage. These two scenarios are illustrated with the selected snapshots shown in Figure 17 for L^{26} and in Figure 18 for L^{8}. Furthermore, two additional replicas were carried out for both systems using different initial velocities and starting coordinates and equivalent results were obtained. Hence, as the distance between the considered reference point and Cl^-, on average, is beyond the distance within hydrogen bonds are possible, no further analysis of these bonding interactions is performed.

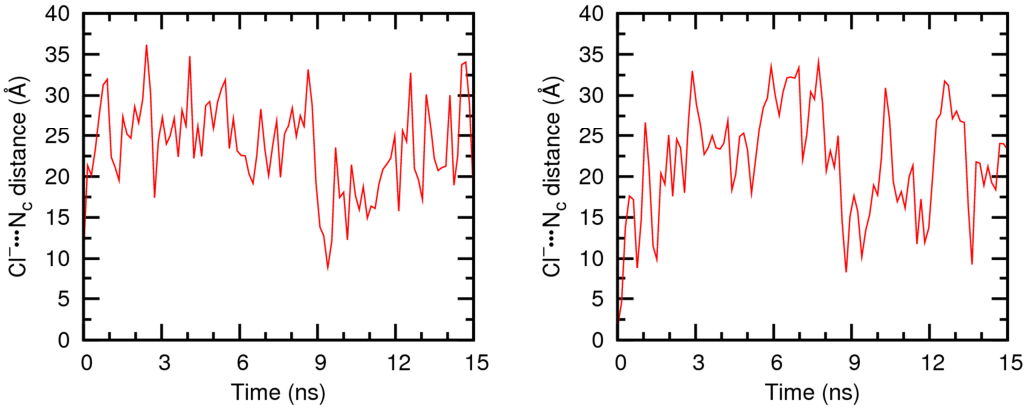

Figure 16 – Evolution of the Cl^-•••N_c distance during the entire time of the MD simulation for $L^{26}\subset Cl^-$ (left) and $L^{8}\subset Cl^-$ (right) associations in water. Data was smoothed with Bézier curves.

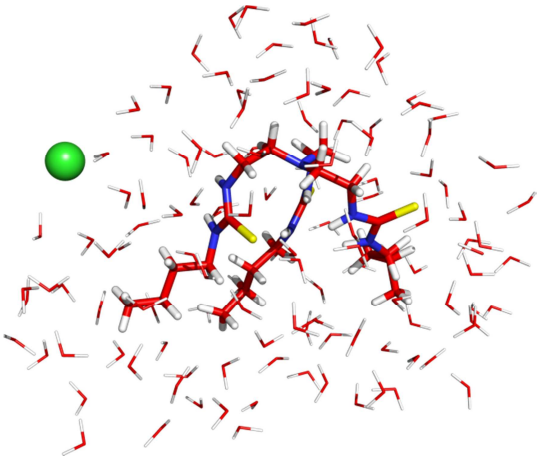

Figure 17 – Snapshot taken at 240 ps of equilibration, showing the chloride anion away from the L^{26} and surrounded by water molecules. Only water molecules within 5.0 Å radius from L^{26} are shown.

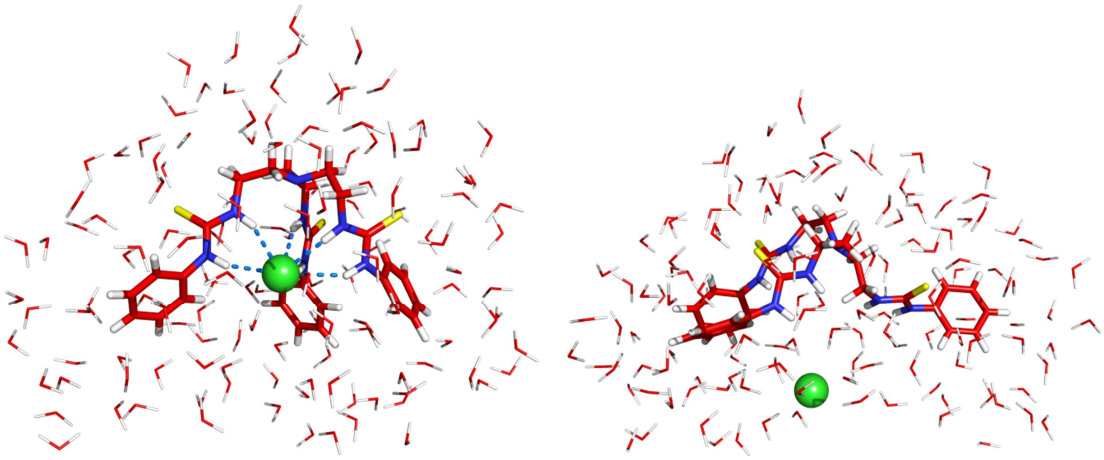

Figure 18 – Snapshots illustrating the release of chloride anion from L^{8} taken at 80 and 100 ps of the MD simulation, from left to right. Only water molecules within 5.0 Å radius from L^{8} are shown.

The structural results obtained in water were expected, taking into account that the chloride affinity for both receptors in DMSO/water solution, a less polar solvent, is low, as shown by the experimental binding constants of 447 and 191 M^{-1} for receptors L^{26} and L^{8} respectively.(68) However, the molecular dynamics simulations also show that L^{26} and L^{8} are able to release the chloride in water, in the opposition behaviour found in DMSO/water solution. These two insights together suggest that they are good candidates to promote the chloride transport across membranes. This is the matter of the next chapter.

Having analysed the chloride affinity of L^{26} and L^{8} in water and DMSO/water solution separately, the solvation of these systems is now evaluated using the radial distribution functions (RDF), calculated for receptors and chloride in the two solvent media. In addition, for comparison purposes, the RDF for an isolated chloride in pure DMSO solution and water solution was also considered in the subsequent discussion.

The solvation structure of DMSO around the chloride associations is presented in Figure 19 for L^{26} (left) and L^{8} (right). Both receptors (the centre of mass) show two smooth solvent shells (red line) with the first one occurring between 6 and 8 Å and the second one at about 12 Å in the solvent bulk. This result shows that the binding pocket provided by these receptors is free of DMSO solvent molecules. The chloride anion, while hydrogen bonded to either L^{26} or L^{8}, shows four well defined solvent shells (green line) with the first solvation centred at 6.2 Å from this anion. In contrast, the DMSO structure around an isolated chloride (blue line) is characterised by a strong solvation shell located at a shorter distance of 5.9 Å, which is agreement with value of 6.0 Å previously obtained by MD dynamics using a DMSO full atoms model,(121) and closer to the experimentally assessed value of 5.4 Å.(122) Therefore, this comparison confirms that the chloride is surrounded only by either L^{26} or L^{8}, while the association is prominently solvated by DMSO and water molecules, as seen in Figure 19.

The radial distribution functions for the systems where chloride with L^{26} and L^{8} were solvated in water, presented in Figure 20, left and right respectively, differ greatly from the results observed in DMSO solution. When considering the hydration of both receptors (the centre of mass), a shoulder corresponding to the first solvation shell occurs at 3.0 Å suggesting that no solvent molecules are present within the binding pockets while L^{26} and L^{8} retained the tripodal conformational shape.

On the other hand, the chloride in presence of L^{26} and L^{8} exhibits three water shells with the first one occurring as a strong and sharp peak at 3.1 Å. The second and third solvation shells were observed at 4.9 and 7.2 Å from the chloride. As the chloride is away of the receptor and completely surrounded by water molecules, this radial hydration structure is similar to that observed for the isolated chloride. This last RDF (blue line in left and right plots) reproduces the RDF of the water molecules around the chloride previously calculated with anion van der Walls parameters and SPC/E water model employed in this work,(112) and matches the experimental value of 3.12 Å (refs. (123, 124) cited in (112)).

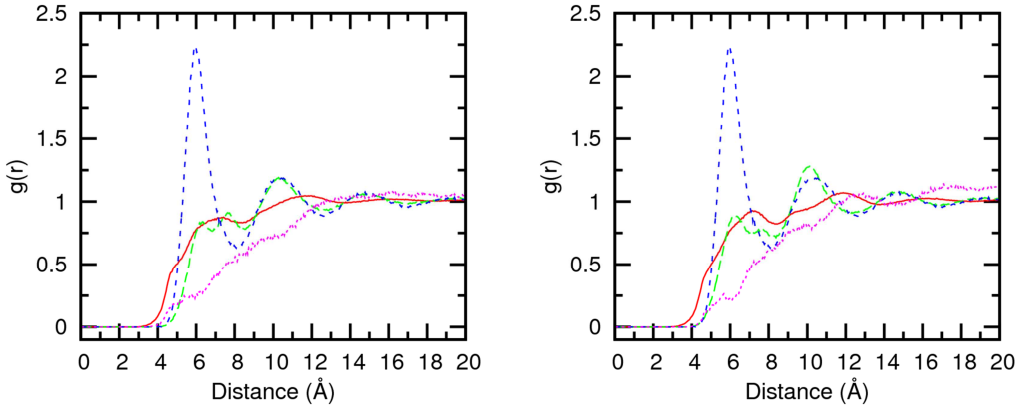

Figure 19 – RDF, g(*r*), of the DMSO molecules around the receptor (red line) and chloride (green line) and water molecules around the chloride (magenta line) in the associations with L^{26} (left) and L^{8} (right). For comparison purposes, the radial solvation structure of the isolated chloride (blue) is also shown.

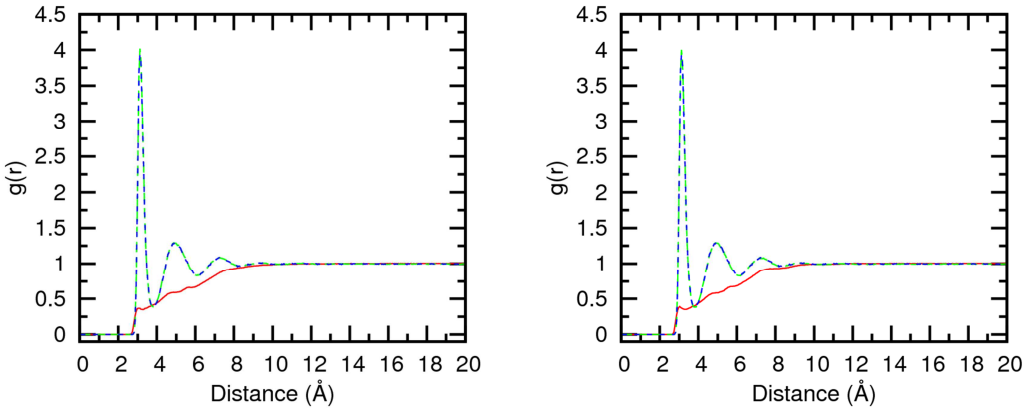

Figure 20 – Radial hydration structure of the receptor (red) and chloride anion (green) in the presence of L^{26} (left) and L^{8} (right) for the SPC/E water model. For comparison purposes, the RDF of the water molecules around an isolated chloride (blue) is also shown.

2.3 Summing Up

In conclusion, the MD simulation structural data show that the chloride association with both receptors is retained in DMSO/water solution, while in water the chloride anion is quickly solvated by water molecules, leaving the binding pocket of each receptor. This is in line with the expect behaviour of a potential transporter, that should be able to bind the anion while inside a phospholipid bilayer, here surrogated by the DMSO solution, but should also be able to free chloride when reaching the outside of such bilayer (the water solution) and, for instances, to be able to grab it in the water solution, to facilitate its transport across the bilayer. Thus, the main goal outlined for this second chapter, the evaluation of the binding ability for chloride anion, was almost accomplished up to this part of the text. Both receptors, L^{26} and L^{8}, were successfully described with the GAFF and RESP charges. Also, all MD simulations performed in gas-phase and solution yielded results that allowed an extensive structural characterization of L^{26} and L^{8} and their binding associations. Unfortunately, the comparison with experimental data in energetic terms was limited. Indeed, the estimative of the absolute and relative binding free energies of L^{26} and L^{8} towards chloride was intended by means of thermodynamic integration methods. The estimated binding free energies were inconsistent with those obtained from the experimental association constants. This drawback was, perhaps, due to the small values of the chloride association constants for both receptors, leading to a small difference in the free energy of 2.11 kJ mol^{-1}. Furthermore other well-established methods widely applied in the free energy calculations using MD data in water solution, such as Molecular Mechanics Poisson-Boltzmann Surface Area (MM-PBSA), are not parameterized to be utilized with organic solvents, for instance DMSO.

3 Chloride transport across a phospholipid bilayer membrane assisted by tripodal receptors

This chapter reports the molecular dynamics investigation carried out on the chloride transmembranar transport across a bilayer membrane model, mediated by the tripodal thioureas L^{26} and L^{8} (see Scheme 4 and Scheme 7, Chapter 1). The bilayer is composed of POPC phospholipids (see Scheme 8, also in Chapter 1) in agreement with the composition of the vesicle utilized in the experimental studies, as stated in Chapter 1.(68)

Over the last year, two significant studies reporting molecular dynamics simulations of pure POPC membranes with specific force field parameterisation for phospholipids were published: Poger *et al*. simulated a membrane composed of 128 POPC lipids and hydrated with 5940 SPC model water molecules in two slabs, using the GROMOS $G53A6_L$ united atom force field;(89) Pastor, MacKerell and co-workers simulated a membrane formed by 72 lipids and 2242 TIP3P water molecules with CHARMM36 all-atom force field.(87) The versions of these two force fields have reproduced well the structural and dynamic membrane parameters, *viz*. the area per lipid, without the imposition of artificial surface tension.

The first DMPC and DOPC lipid model membrane simulations using the GAFF together with the AMBER software package were reported by Gould and Rosso. These simulations were carried out without the imposition of surface tension, resulting in values of area per lipid below the experimental value (65.0 $Å^2$ for DOPC and 55.8 $Å^2$ for DMPC, *vs.* experimental values of 72.1 $Å^2$ for DOPC and between 59.6 to 62.2 $Å^2$ for DMPC).(84) Afterwards, Böckmann and co-workers found a better match between the estimated and experimental liquid phase properties, simulating a DOPC pure membrane model of 72 lipids and 2727 water molecules with a surface tension of 22 dyn/cm per monolayer.(85) Martinek and Jójárt have simulated a system with 128 POPC lipid membrane with GAFF and two slim hydration slabs with a total of 2985 TIP3P water molecules, fitting the experimental area per lipid (68.3 ± 1.5 $Å^2$) using a surface tension of 60 dyn/cm for the whole system.(83) The latter membrane simulations of the DOPC lipid bilayers were carried out with GROMACS (Groningen MAchine for Chemical Simulation) and the POPC with NAMD (Not (just) Another Molecular Dynamics program), because the AMBER11 suite does not feature the possibility to impose surface tension to a surface parallel to the *x-y* plane. The simulation conditions employed for the POPC independent studies mentioned above are summarised in the Table 19.

Table 19 – Summary of recent molecular dynamics simulations carried out with a pure POPC bilayer.

Membrane	*Number of molecules*		*Water:lipid ratio*	*Surface tension (dyn/cm)*	*Temperature (K)*	*Ref.*
	POPC	Water (model)				
I	128	5941 (SPC)	46.4:1	-	303	(89)
II	72	2242 (TIP3P)	31.1:1	-	303	(87)
III	128	2985 (TIP3P)	23.3:1	60	303 / 310*	(83)

Model III has a deficient number of waters per lipid (23.3:1) when compared with the models I and II, with water:lipid ratios above the necessary minimum, commonly *ca.* 30 water molecules per lipid molecule, corresponding to fully hydrated membrane models.(89, 125, 126) Therefore model II, corresponding to a fully hydrated lipid bilayer, was selected (see below), and tested with the TIP3P and SPC/E water models (simulations A to D below), as done by Böckmann *et al.* in the simulation of a DOPC bilayer membrane.(85) Additionally, an overhydrated membrane model containing 4954 water molecules, able to accommodate L^{26} and L^{8} in the water slabs, was built (model IV), as described below.

This chapter is organised as follows: in the first part, the simulations performed in the fully and overhydrated pure membrane models are described. The results obtained are compared with the literature. The impact of water excess in the structural properties of the phospholipid bilayer presented in model IV is also evaluated. The second part deals with structural and dynamic features associated with transmembranar permeation of L^{26} and L^{8} when their chloride associations are placed in the water slab or within the phospholipid bilayer of the overhydrated membrane model. All unconstrained molecular dynamics simulations were carried out using GAFF with the GROMACS package. While most of the analysis of the structural and dynamic parameters were performed with tools from the GROMACS package,(127) the order parameters were analysed with the dcd2dorder tool from the MOLDY Tools package.(128) All renderings were made with *PyMOL*.(120)

3.1 Pure Membranes

3.1.1 Fully Hydrated free membrane simulation

The first studies were performed to find out the best simulation conditions that consistently reproduced most of the experimental parameters available. This was done using the pre-equilibrated POPC bilayer (model II), available at the website of the Laboratory of Molecular & Thermodynamic Modeling of the University of Maryland,(129) conjugated with two water models (SPC/E and TIP3P) and two sets of atomic RESP charges (see below). Thus, four independent systems listed in Table 20 were obtained and were simulated at the physiological temperature of 310 K.

Table 20 – Summary of simulations conditions employed to simulate the membrane model II.

System ID	*Water Model*	*Charge Set*
A	SPC/E	Unconstrained RESP charges
B	TIP3P	
C	SPC/E	RESP charges taken from ref. (83)
D	TIP3P	

Methodology

POPC charge determination and conversion of AMBER files

From the pre-equilibrated POPC bilayer (model II), thirteen different conformations of the POPC lipid were extracted and optimized in *Gaussian 03* at the HF/6-31G* level of theory. Atomic charges were then calculated *via* a multiconformational RESP fitting using all these optimised conformations and following the methodology previously described for L^{26} and L^{8}. The POPC molecules were described with default parameters taken from the GAFF and the water molecules using SPC/E or TIP3P water models as implemented in AMBER11. The atomic charges for POPC, together with the atom types employed, are presented in Table 23, while the corresponding atomic numbering scheme for a single POPC molecule is shown in Scheme 11.

The atomic coordinates of a single POPC molecule together with multiRESP atomic charges as well as a corresponding *frcmod* file, were loaded in *xLEaP* to generate the AMBER

topology and coordinate files. These two files, along with topology and atomic coordinate files for a single SPC/E or TIP3P water model molecules were then converted with *acpype.py* (130, 131) into GROMACS topology files for the systems A to D (see Table 20).

Table 21 – Atom types and unconstrained RESP charges employed for the systems A and B.

ID[a]	*AT*[b]	*Charge*	***ID***[a]	*AT*[b]	*Charge*	***ID***[a]	*AT*[b]	*Charge*	***ID***[a]	*AT*[b]	*Charge*
N1	n4	0.05325	**H18**	hc	0.03824	**H38**	hc	-0.01203	**H61**	hc	-0.02641
C1	c3	0.08104	**C10**	c3	-0.05392	**C22**	c3	0.02431	**C33**	c3	-0.00796
C2	c3	-0.21377	**H19**	h1	0.09508	**H39**	hc	-0.00914	**H62**	hc	-0.00429
C3	c3	-0.21377	**H20**	h1	0.09508	**H40**	hc	-0.00914	**H63**	hc	-0.00429
C4	c3	-0.21377	**O7**	os	-0.41283	**C23**	c3	0.02762	**C34**	c3	0.00544
H1	hx	0.05800	**C11**	c	0.89042	**H41**	hc	-0.01239	**H64**	hc	-0.00782
H2	hx	0.05800	**O8**	o	-0.61260	**H42**	hc	-0.01239	**H65**	hc	-0.00782
H3	hx	0.12795	**C12**	c3	-0.38849	**C24**	c3	0.01149	**C35**	c3	0.02685
H4	hx	0.12795	**H21**	hc	0.08987	**H43**	hc	-0.00730	**H66**	hc	-0.00739
H5	hx	0.12795	**H22**	hc	0.08987	**H44**	hc	-0.00730	**H67**	hc	-0.00739
H6	hx	0.12795	**C13**	c3	0.05948	**C25**	c3	0.00212	**C36**	c3	0.02223
H7	hx	0.12795	**H23**	hc	-0.01022	**H45**	hc	-0.00371	**H68**	hc	-0.00887
H8	hx	0.12795	**H24**	hc	-0.01022	**H46**	hc	-0.00371	**H69**	hc	-0.00887
H9	hx	0.12795	**C14**	c3	0.01051	**C26**	c3	-0.00805	**C37**	c3	0.00291
H10	hx	0.12795	**H25**	hc	-0.00185	**H47**	hc	-0.00236	**H70**	hc	-0.00878
H11	hx	0.12795	**H26**	hc	-0.00185	**H48**	hc	-0.00236	**H71**	hc	-0.00878
C5	c3	0.08010	**C15**	c3	0.01933	**C27**	c3	0.14052	**C38**	c3	0.03461
H12	h1	0.05395	**H27**	hc	-0.00314	**H49**	hc	-0.03056	**H72**	hc	-0.01300
H13	h1	0.05395	**H28**	hc	-0.00314	**H50**	hc	-0.03056	**H73**	hc	-0.01300
P1	p5	1.09860	**C16**	c3	0.01678	**C28**	c3	-0.16932	**C39**	c3	0.02002
O1	o	-0.68892	**H29**	hc	-0.01514	**H51**	hc	0.03476	**H74**	hc	-0.00933
O2	o	-0.68892	**H30**	hc	-0.01514	**H52**	hc	0.03476	**H75**	hc	-0.00933
O3	os	-0.41491	**C17**	c3	0.06219	**H53**	hc	0.03476	**C40**	c3	-0.01804
O4	os	-0.43193	**H31**	hc	-0.02897	**C29**	c3	0.19448	**H76**	hc	-0.00357
C6	c3	0.09333	**H32**	hc	-0.02897	**H54**	hc	-0.01597	**H77**	hc	-0.00357
H14	h1	0.05060	**C18**	c3	0.18218	**H55**	hc	-0.01597	**C41**	c3	0.16253
H15	h1	0.05060	**H33**	hc	-0.02013	**C30**	c3	-0.02362	**H78**	hc	-0.03591
C7	c3	0.25590	**H34**	hc	-0.02013	**H56**	hc	0.00208	**H79**	hc	-0.03591
H16	h1	0.04544	**C19**	c2	-0.26060	**H57**	hc	0.00208	**C42**	c3	-0.17712
O5	os	-0.39444	**H35**	ha	0.12796	**C31**	c3	-0.02797	**H80**	hc	0.03550
C8	c	0.71653	**C20**	c2	-0.27088	**H58**	hc	-0.00599	**H81**	hc	0.03550
O6	o	-0.57530	**H36**	ha	0.12663	**H59**	hc	-0.00599	**H82**	hc	0.03550
C9	c3	-0.11970	**C21**	c3	0.15846	**C32**	c3	0.10418			
H17	hc	0.03824	**H37**	hc	-0.01203	**H60**	hc	-0.02641			

[a] ID corresponds to the atom number shown in Scheme 11
[b] AT is the atom type according to GAFF

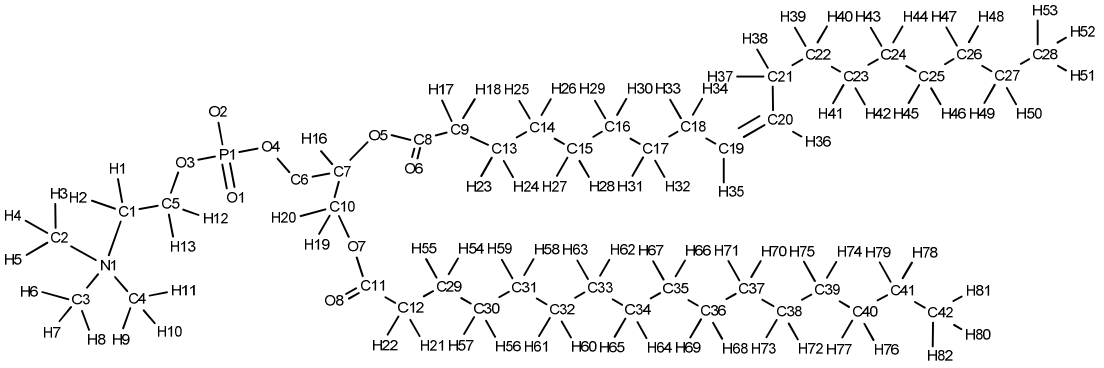

Scheme 11

The simulations of the systems C and D were performed with RESP charges calculated as described in ref. (83). These charges, presented in Table 22, were kindly provided by Professor Tamás A. Martinek, and were calculated using 12 different lipid conformations but applying the following restraints during the RESP fitting: charge of +1 for the $N(CH_3)_3$ moiety; charge of -1 for the PO4 group; the carbon and hydrogen atoms of the alkyl chains were treated as equivalent; and a 0.2 charge was assigned to each hydrogen atom in the choline head. Thus, it was possible to evaluate the impact of the two sets of RESP charges on the structure and dynamics of the phospholipid bilayer.

Table 22 – Atom Types and RESP charges from ref. (83) employed for the systems C and D.

ID[a]	*AT*[b]	*Charge*	***ID***[a]	*AT*[b]	*Charge*	***ID***[a]	*AT*[b]	*Charge*	***ID***[a]	*AT*[b]	*Charge*
N1	n4	-1.01913	**H18**	hc	0.06817	**H38**	hc	0.06817	**H61**	hc	0.06817
C1	c3	0.28103	**C10**	c3	0.16900	**C22**	c3	-0.13634	**C33**	c3	-0.13634
C2	c3	-0.33730	**H19**	h1	0.06817	**H39**	hc	0.06817	**H62**	hc	0.06817
C3	c3	-0.33730	**H20**	h1	0.06817	**H40**	hc	0.06817	**H63**	hc	0.06817
C4	c3	-0.33730	**O7**	os	-0.51928	**C23**	c3	-0.13634	**C34**	c3	-0.13634
H1	hx	0.25000	**C11**	c	0.92373	**H41**	hc	0.06817	**H64**	hc	0.06817
H2	hx	0.25000	**O8**	o	-0.67181	**H42**	hc	0.06817	**H65**	hc	0.06817
H3	hx	0.25000	**C12**	c3	-0.16261	**C24**	c3	-0.13634	**C35**	c3	-0.13634
H4	hx	0.25000	**H21**	hc	0.06817	**H43**	hc	0.06817	**H66**	hc	0.06817
H5	hx	0.25000	**H22**	hc	0.06817	**H44**	hc	0.06817	**H67**	hc	0.06817
H6	hx	0.25000	**C13**	c3	-0.13634	**C25**	c3	-0.13634	**C36**	c3	-0.13634
H7	hx	0.25000	**H23**	hc	0.06817	**H45**	hc	0.06817	**H68**	hc	0.06817
H8	hx	0.25000	**H24**	hc	0.06817	**H46**	hc	0.06817	**H69**	hc	0.06817
H9	hx	0.25000	**C14**	c3	-0.13634	**C26**	c3	-0.13634	**C37**	c3	-0.13634
H10	hx	0.25000	**H25**	hc	0.06817	**H47**	hc	0.06817	**H70**	hc	0.06817

ID[a]	*AT*[b]	*Charge*	***ID***[a]	*AT*[b]	*Charge*	***ID***[a]	*AT*[b]	*Charge*	***ID***[a]	*AT*[b]	*Charge*
H11	hx	0.25000	**H26**	hc	0.06817	**H48**	hc	0.06817	**H71**	hc	0.06817
C5	c3	-0.28697	**C15**	c3	-0.13634	**C27**	c3	-0.13634	**C38**	c3	-0.13634
H12	h1	0.06817	**H27**	hc	0.06817	**H49**	hc	0.06817	**H72**	hc	0.06817
H13	h1	0.06817	**H28**	hc	0.06817	**H50**	hc	0.06817	**H73**	hc	0.06817
P1	p5	1.36092	**C16**	c3	-0.13634	**C28**	c3	-0.20452	**C39**	c3	-0.13634
O1	o	-0.73818	**H29**	hc	0.06817	**H51**	hc	0.06817	**H74**	hc	0.06817
O2	o	-0.73818	**H30**	hc	0.06817	**H52**	hc	0.06817	**H75**	hc	0.06817
O3	os	-0.48106	**C17**	c3	-0.13634	**H53**	hc	0.06817	**C40**	c3	-0.13634
O4	os	-0.48106	**H31**	hc	0.06817	**C29**	c3	-0.13634	**H76**	hc	0.06817
C6	c3	0.08305	**H32**	hc	0.06817	**H54**	hc	0.06817	**H77**	hc	0.06817
H14	h1	0.06817	**C18**	c3	-0.13634	**H55**	hc	0.06817	**C41**	c3	-0.13634
H15	h1	0.06817	**H33**	hc	0.06817	**C30**	c3	-0.13634	**H78**	hc	0.06817
C7	c3	0.22257	**H34**	hc	0.06817	**H56**	hc	0.06817	**H79**	hc	0.06817
H16	h1	0.06817	**C19**	c2	-0.04095	**H57**	hc	0.06817	**C42**	c3	-0.20452
O5	os	-0.51928	**H35**	ha	0.04095	**C31**	c3	-0.13634	**H80**	hc	0.06817
C8	c	0.92373	**C20**	c2	-0.04095	**H58**	hc	0.06817	**H81**	hc	0.06817
O6	o	-0.67181	**H36**	ha	0.04095	**H59**	hc	0.06817	**H82**	hc	0.06817
C9	c3	-0.16261	**C21**	c3	-0.13634	**C32**	c3	-0.13634			
H17	hc	0.06817	**H37**	hc	0.06817	**H60**	hc	0.06817			

[a] ID corresponds to the atom number shown in Scheme 11
[b] AT is the atom type according to GAFF

Simulation conditions

The simulations of the four independent systems (A to D) were performed with GROMACS 4.5.3.(127) using the following protocol: The equilibration process started with molecular mechanics minimization of the system using the steepest descent algorithm for 100000 steps. The equilibration proceeded with the heating of the pure membrane from 0 to 310 K using a NVT ensemble for 50 ps. Subsequently, the ensemble was changed to NPT and a simulation run of 150 ns was carried out. The long-range electrostatic interactions under the periodic boundary conditions were described with the PME algorithm (119) using real-space cut-off at 10 Å, accordingly with the established for bilayer simulations,(132) and the maximal grid size of 1.2 Å. The cut-off for the Lennard-Jones interactions was also set at 10 Å and they were updated every 20 fs, together with pair lists. The temperature of the system was maintained independently coupling the lipids and the water slabs to an external bath temperature of 310 K, using the Berendsen thermostat,(133) and a coupling constant τ_T of 0.1 ps. The pressure was controlled by the Berendsen barostat at 1 atm and compressibility of 4.5×10^{-5} bar^{-1}, with the independent coupling in the *x,y-* and *z-* vectors and using a surface tension of 60

dyn/cm,(83) with a coupling constant τ_P of 1.0 ps. The covalent bonds to hydrogen atoms were constrained using the LINCS algorithm,(134) allowing the use of a 2 fs time step. Frames were saved every 1.0 ps, leading to trajectory files with 150000 structures.

This protocol was employed to run three independent replicas of the systems A, B, C and D with different random seeds for the initial velocities.

Results and discussion

The molecular dynamics POPC bilayer simulations were evaluated using the following biophysical membrane parameters: area per lipid, volume per lipid, bilayer thickness, electron density profile, chain order, lateral diffusion and hydration of the water/lipid interface. The values of these representative liquid phase properties for the structure and dynamics of lipids are compared with the experimental ones as well as with theoretical data from Pastor, MacKerell and co-workers,(87) and from Martinek and Jójárt,(83), to validate the employed parameters. The results obtained are presented in separated subsections, comparing the two water models and two charges sets utilized. These simulated systems are illustrated in Figure 21, with a snapshot taken at the end of a replica simulation of system A.

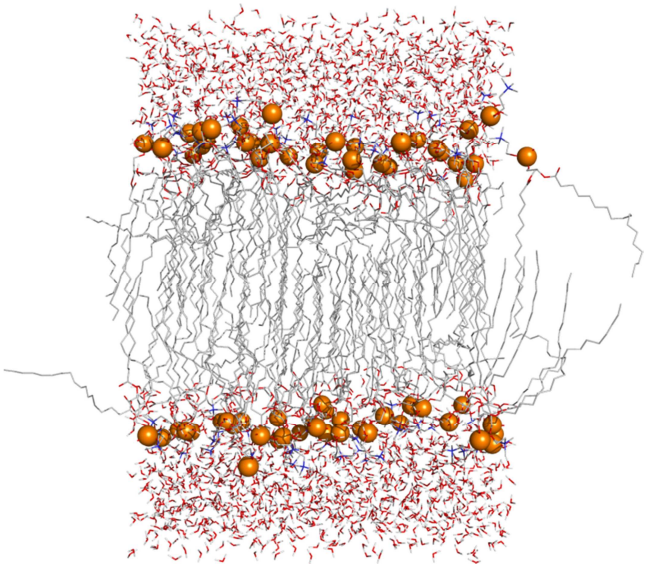

Figure 21 – Snapshot of a replica MD simulation of system A, at 150 ns.

Area per lipid

Area per lipid is quite often considered as the major indicator to assess when the membrane model is *equilibrated*. This condition is achieved when the area per lipid (A_L), estimated by Equation 1 (where $A_{x \bullet y}$ stands for the area of the *x*-*y* section of the system, and $n_L/2$ corresponds to the number of lipid molecules in each monolayer of the system (36)), stabilises around a given value for a considerable simulation time.

$$A_L = \langle \frac{A_{x \cdot y}}{n_L/2} \rangle \qquad \text{Equation 1}$$

In the MD simulations reported here, the systems were considered equilibrated after the first 100 ns of simulation, as indicated by the evolution of area per lipid shown in Figure 22 for the systems A and B and in Figure 23 for simulations C and D. Therefore, only the last 50 ns of the three replica runs, giving a total sampling time of 150 ns per system, were utilized in the calculation of area per lipid as well as other membrane structural parameters. Concerning the area per lipid, the experimental values of 68.3 (135) and 66.0 $Å^2$,(136) obtained at 303 and 310 K respectively, will be considered as reference in the subsequent analysis and are plotted in Figure 22 and Figure 23 as cyan and magenta lines, respectively. The value at 303 K will be utilized for comparison purposes in this parameter and in the following parameters, as any other experimental POPC studies were found in the literature at 310 K. Also, this temperature above the gel to liquid-crystalline phase transition temperature, ~270.5 K,(137) is commonly applied both in theoretical and experimental bilayer studies.

The average values for 150 ns of sampling with the associated standard deviations are listed in Table 17 for the systems A, B, C and D. Henceforth, these values will be utilized, unless it is stated otherwise. In the MD simulations with TIP3P water model (systems B and D), the average area per lipid is markedly above both reference values independently of the charge set (see Figure 22 and Figure 23, right plots). On the other hand, when the SPC/E water model is employed (systems A and C), the area per lipid presents different average values, according to the charges set employed. It is remarkable that the average value for system A of 65.55 ± 3.05 $Å^2$ is in perfect agreement with reference value of 66 $Å^2$ obtained by X-ray scattering.(136) In contrast, for system C, characterized by RESP charges from ref. (83) and SPC/E water model, the average area per lipid of 73.80 ± 2.48 $Å^2$ is higher than the experimental value. Furthermore, when the SPC/E water model in this system is replaced by TIP3P model (system D), the area per lipid average is 78.34 ± 3.09 Å, now deviated from the reference value by 12.34 Å. This last average area per lipid is higher than the one previously obtained (72.40 ± 0.58 Å) by Martinek and Jójárt at 310 K, for a system composed of 128

POPC lipids and 2985 TIP3P model water molecules, where the lipids were described with the same atomic charges scheme.(83)

This comparison indicates that the parameters of system A (RESP atomic charges for lipids conjugated with a SPC/E model for water molecules), with a negligible difference in area per lipid relatively to the experimental value, seems to be the best choice to simulate a POPC membrane with the GAFF at 310 K, when considering how complex this type of systems are. This hint will be subject to a subsequent confirmation by analysis of the remaining biophysical parameters.

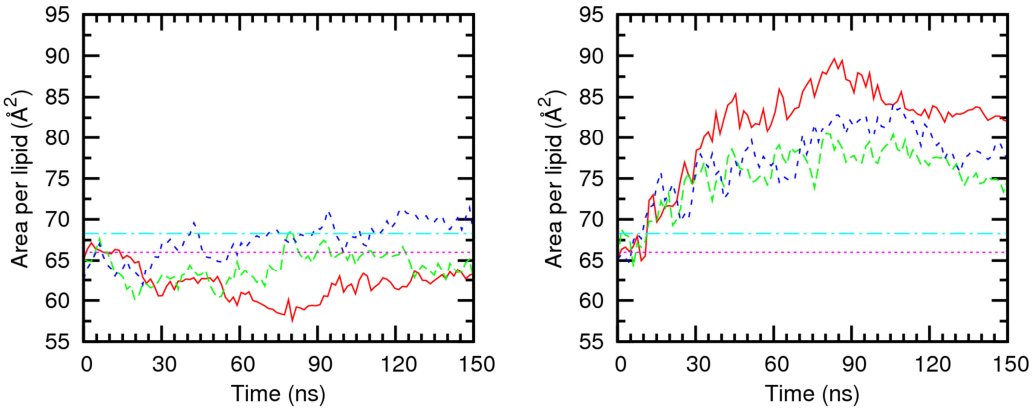

Figure 22 – Evolution of area per lipid in the systems A (left) and B (right) throughout the course of the MD simulation time. The experimental values are plotted as cyan and magenta lines. The red, blue and green lines correspond to each one of the three replicas. Data was smoothed with Bézier curves.

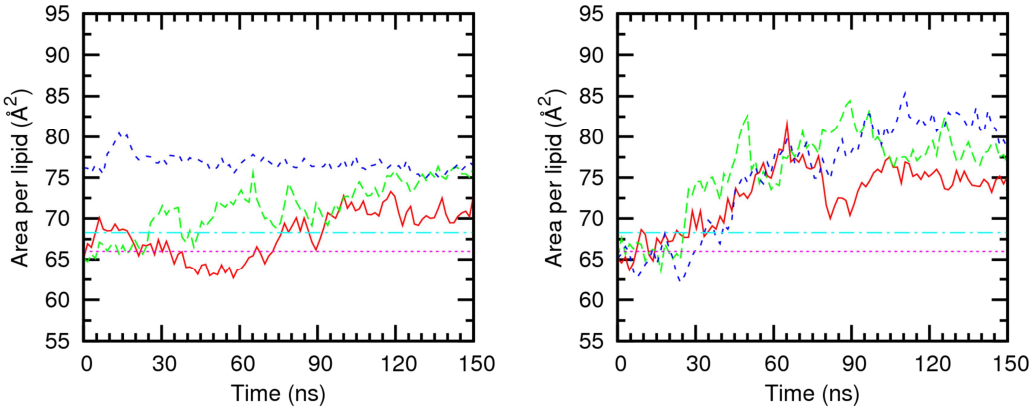

Figure 23 – Evolution of area per lipid in the systems C (left) and D (right) throughout the course of the MD simulation time. Remaining details as given in Figure 22.

Table 23 – Variation on the area per lipid for the systems A to D, using a 150 ns sampling time.*

System	*Mean ± Std Dev (Å²)*	*Min (Å²)*	*Max (Å²)*
A	65.55 ± 3.05	59.71	73.29
B	79.87 ± 3.29	71.84	88.27
C	73.80 ± 2.48	67.27	79.75
D	78.34 ± 3.09	71.14	87.89

* The average and standard deviation values are calculated for *N*=150000.

Volume per lipid

Volume per lipid (V_L) is another biophysical structural parameter, commonly evaluated in membrane MD simulations, and prone to be compared with experimental data. V_L is given by Equation 2, where V stands for the volume of the system, n_w stands for the number of molecules in the system (2242), V_w stands for the volume of a water molecule at 310 K (30.1096 Å^3) and n_L corresponds to the number of lipid molecules in the system (72).

$$V_L = \langle \frac{V - n_w V_w}{n_L} \rangle \qquad \text{Equation 2}$$

During the period where the membranes were considered to be equilibrated, except in system C (see Figure 25, right plot), all systems (Figure 24, both plots, and Figure 25, left plot) generally present a reduction in the volume per lipid, assuming values below the reference value of 1256 Å^3 for 303 K.(135) It is imperative to remember that these systems were simulated at 310 K, so the reference value must be carefully considered. In the systems A and C, the average volume per lipid is 1248.9 ± 23.8 and 1251.8 ± 19.2 Å^3, respectively, yielding averages close to the experimental reference. Also, in system B, with TIP3P water model, the volume per lipid average (1262.4 ± 10.6 Å^3) was in line with the reference value for 303 K. Regarding system D, characterized with atomic charges from ref. (83) and TIP3P water model, the average volume per lipid 1271.2 ± 11.4 Å^3 is found to differ greatly from the reference value. All volume per lipid averages for the systems A to D are summarized in Table 24. The absence of other theoretical results (83, 87) prevents further comparison.

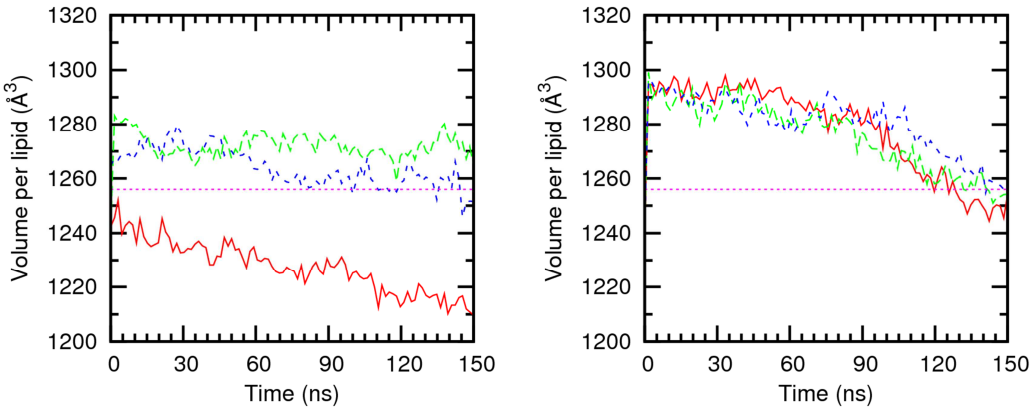

Figure 24 – Evolution of volume per lipid in the systems A (left) and B (right) throughout the course of the MD simulation time. The experimental value is plotted as a magenta line. The red, blue and green lines correspond to each one of the three replicas. Data was smoothed with Bézier curves.

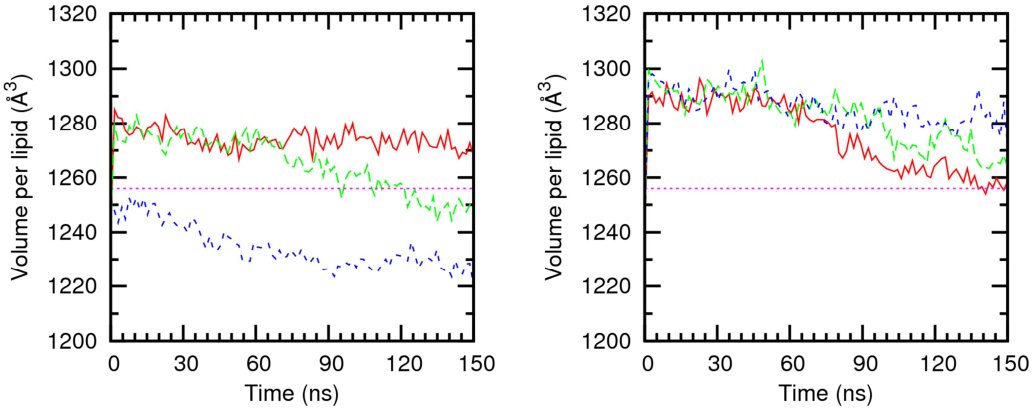

Figure 25 – Evolution of volume per lipid in the systems C (left) and D (right) throughout the course of the MD simulation time. Remaining details as given in Figure 24.

Table 24 – Variation on the volume per lipid for the systems A to D, using a 150 ns sampling time.*

System	*Mean ± Std Dev (Å^3)*	*Min (Å^3)*	*Max (Å^3)*
A	1248.9 ± 23.8	1194.6	1297.8
B	1262.4 ± 10.6	1226.0	1308.5
C	1251.8 ± 19.2	1205.9	1298.1
D	1271.2 ± 11.4	1235.4	1315.3

* The average and standard deviation values are calculated for *N*=150000.

Bilayer thickness

The bilayer thickness over simulation time was measured as the distance between the average *z* coordinate of the phosphorus atoms in each monolayer, for each frame, and is, along with area per lipid, of paramount importance in the structural characterisation of a phospholipid bilayer membrane. Moreover, when area per lipid diminishes, the bilayer thickness generally increases, and *vice versa*. This is precisely illustrated in Figure 26, for a replica MD simulation of system A.

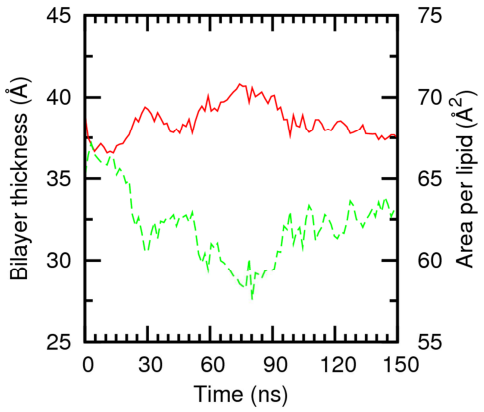

Figure 26 – Evolution of bilayer thickness and area per lipid for a single replica of system A throughout the course of the MD simulation time. The red line corresponds to the bilayer thickness and the green line corresponds to the area per lipid. Data was smoothed with Bézier curves.

The variation of the bilayer thickness for 150 ns of sampling assessed with the three replicas is plotted in Figure 27 for the systems A and B and in Figure 28 for the systems C and D. The bilayer thickness for the three replicas of the A system, through the last 50 ns of the MD simulation, almost oscillates around the experimental reference value of 37 Å, measured at 303 K,(135) indicating that the structural integrity of the lipid bilayer is preserved. It is also interesting to note that, when the atomic charges of system A are replaced by the RESP charges taken from the ref. (83), giving the system C, the bilayer thickness average is *ca.* 5 Å below the reference value. For the systems B and D, both with the TIP3P water model, independently of the employed atomic charges, the bilayer thickness is considerably low for the last 50 ns for the three replicas of the MD simulations. The structural findings are entirely consistent with those found for the area per lipid. Among the average bilayer thicknesses calculated for three replicas, the value for system A of 37.1 ± 1.4 Å is surprisingly similar to the experimental reference value of 37 Å at 303 K, while the simulation value previously reported by Martinek and Jójárt is 34 Å. This value was obtained from the electronic density profile of a lipid bilayer with a low water:lipid ratio (23.3:1, see above) measuring the distance between

electronic density peaks (see below). In addition, the systems B and D, with the TIP3P water model present lower average values of bilayer thickness, differ *ca.* 5 Å from the experimental value of 37 Å. Also, the estimated bilayer thicknesses are in agreement with the inverse relation with area per lipid. The variations in bilayer thickness for each simulation are presented in Table 25.

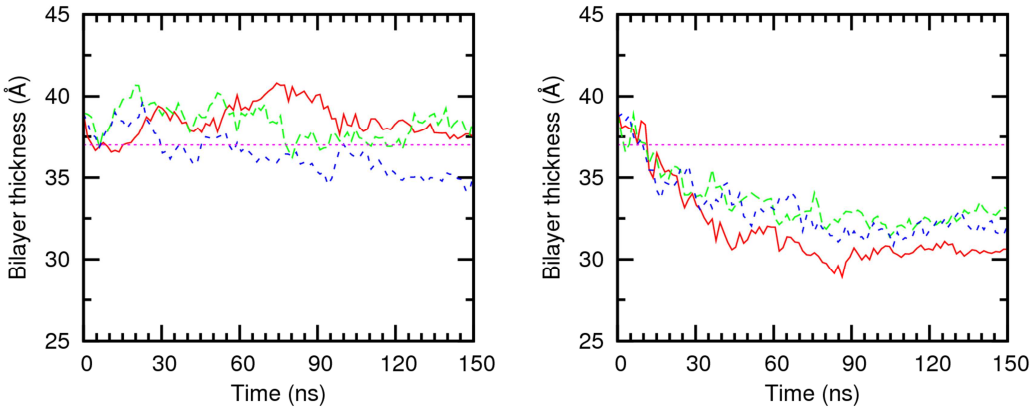

Figure 27 – Evolution of bilayer thickness in the systems A (left) and B (right) throughout the course of the MD simulation time. The experimental value is plotted as a magenta line. The red, blue and green lines correspond to each one of the three replicas. Data was smoothed with Bézier curves.

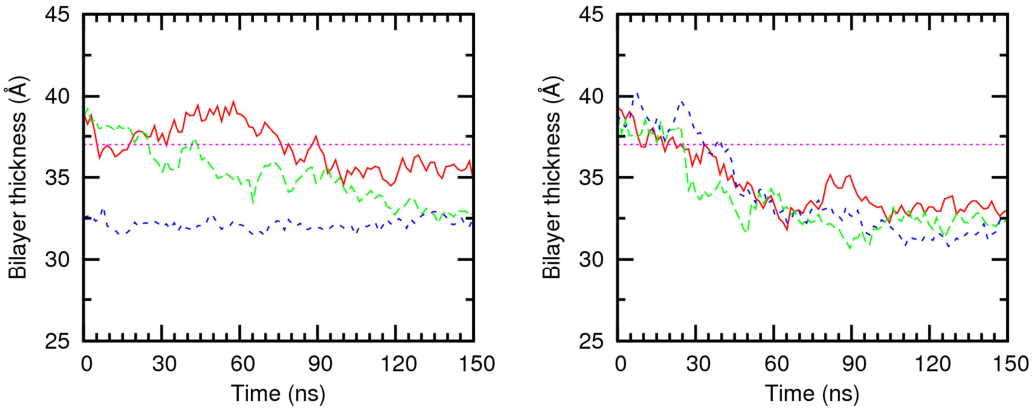

Figure 28 – Evolution of bilayer thickness in the systems C (left) and D (right) throughout the course of the MD simulation, represented as function of time. Remaining details as given in Figure 27.

Table 25 – Variation in the bilayer thickness for the systems A to D, using a 150 ns sampling time.*

Simulation	*Mean ± Std Dev (Å)*	*Min (Å)*	*Max (Å)*
A	37.1 ± 1.4	33.7	40.1
B	31.7 ± 0.9	29.3	34.1
C	33.7 ± 1.4	31.0	37.1
D	32.3 ± 0.8	30.1	34. 9

* The average and standard deviation values are calculated for *N*=150000.

Electron density profile

The electron density profiles are often utilized to estimate bilayer thickness, using the distance between the peaks assigned to the phosphate groups, commonly designated in the literature as $D_{HH,}$(84, 85, 89, 135) although in ref. (83) it is not specified. The electron density profiles of the systems A to D were measured through the *z* axis, considering only the last 10 ns of each MD simulation replica, totalling 30 ns of sampling time. The electron density profiles along the z axis are shown in Figure 29, for the systems A and B and in Figure 30, for the systems C and D. The *z* axis is perpendicular to the phospholipid bilayer normal, taking 0 Å at the core of bilayer. The red line is the total electronic profile of the system; the green line corresponds to the POPC profile, while the blue line represents the electronic density profile of the water slabs juxtaposed to the bilayer. The pink line presents the experimental electronic profile for an artificial POPC lipid bilayer commercially available, and was obtained at 303 K with X-ray scattering.(135) The green line overlaps the red line at z=0 Å (near the middle of the membrane system), where the electronic density of the system corresponds to the density of the POPC lipids. In the extremities of each plot, the blue line overlaps the red, because at greater distances from the middle of the system, the electronic density corresponds to the density of the water slabs, represented by the two symmetric plateaus. The peaks plotted with the red line result mainly from the densities of the head groups of POPC lipids (phosphate groups and choline moieties) and the density of the water molecules between them. The alignment of the red and magenta lines indicates a good fitting of the theoretical and experimental system profiles.

The theoretical profile of system A, showing a small elevation at the centre of the bilayer in the middle of apolar lipid tails, is closely aligned with the experimental one. Furthermore, as would be expected, reflecting the structure of the membrane model, the electron density profile is

symmetric relatively to the origin, displaying two fairly intense peaks, which are mainly determined by the phosphate groups and choline heads from lipids. The distance between these two peaks is *ca.* 34.6 Å, in good agreement with the value calculated for the layer thickness using the distance between the opposite bilayer phosphorus heads throughout the course of the MD simulation (see above). Despite this excellent fitting, it is worth mentioning that such experimental result was obtained at 303 K, while simulations A to D were ran at 310 K, thus the match obtained must be carefully taken in account

Identical profiles for the total electron density were obtained for the systems B, C and D, but presenting a small displacement towards the experimental profile. The distance measured between the two peaks was 31.8, 31.1 and 30.4 Å for the systems B, C and D, respectively. These observations are associated with the bilayer thickness, also lower in those three systems, as shown in Table 25.

The density profiles for the POPC lipids in all systems show a small elevation centred at the core of the lipid bilayer. A possible explanation for this elevation might be the fact that the bilayers in some systems are slightly packed along the *z* axis, thus overlapping methyl terminal groups and elevating the electronic density at the middle of the bilayer.

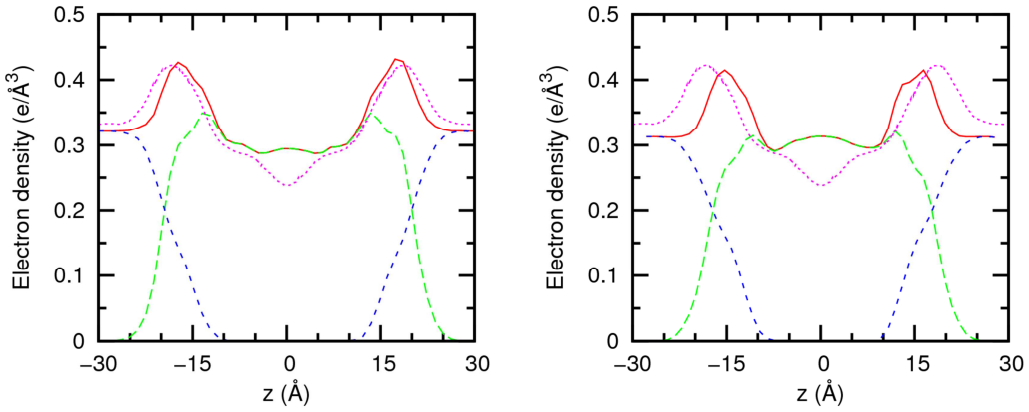

Figure 29 – Electron density profiles calculated for the 10 last ns of the MD simulations performed with system A (left) and B (right). The experimental profile is also shown, as a magenta line.

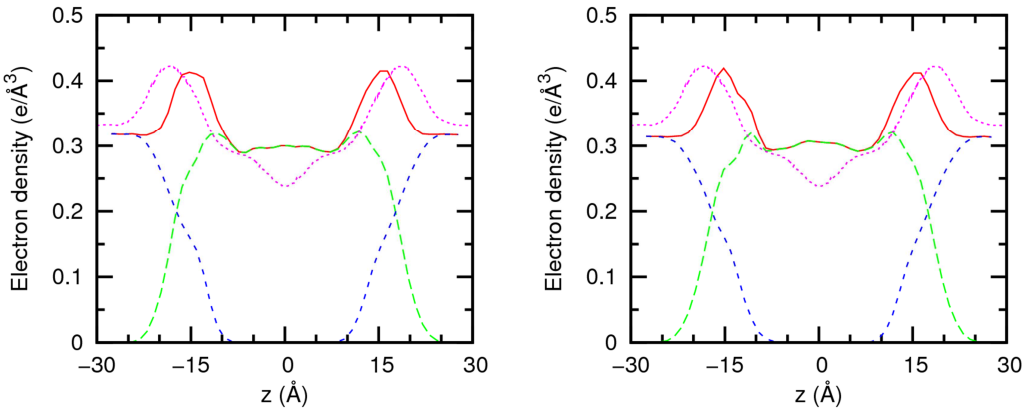

Figure 30 – Electron density profiles calculated for the 10 last ns of the MD simulations performed with system C (left) and D (right). The experimental profile is also shown, as a magenta line.

A comparison with previous MD results reported by Martinek and Jójárt at 310 K is presented in Figure 31, for the systems A (left side) and D (right side), with the pink line now corresponding to the published system, while the red, green and blue lines correspond to the system, POPC and water electronic profiles. System D was selected because the POPC lipids were represented with charges from Martinek (83) and the water model was also the same (TIP3P). On the other hand, among the remaining three systems, system A was characterised by the unconstrained RESP atomic charges and SPC/E water model, being the system with most differences to system D. In spite of the differences on the atomic charges and water models, both electronic density profiles for A and D are close to the theoretical results of Martinek, obtained using a different initial structure.

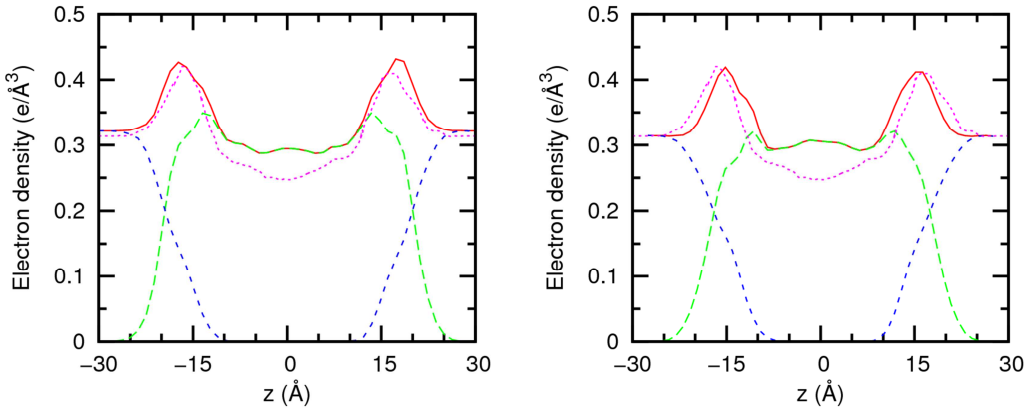

Figure 31 – Electron density profile of the 10 last ns of the MD simulation of system A (left) and of the MD simulation of system D (right) and comparison with published theoretical results.

Furthermore, electronic density profiling allows the analysis of the outline of each component in the system, being either static, if only evaluating a frame, or giving a sort of 'trail' of the most common positions that each component assumes in the system during the time of a trajectory. This characteristic will be further explored in membrane simulations with chloride associations of L^{26} and L^{8}.

Chain order

The ordering of the hydrophobic chains of a lipid is a structural parameter possible to evaluate and compare with the experimental deuterium order parameter ($|S_{CD}|$). In the MD simulations reported here, this analysis was performed for the last 5 ns of each replica, totalling 15 ns of sampling time, with this parameter given by Equation 3, where θ_i is the angle between the bilayer normal and the C*i*-H bond.

$$|S_{CD}| = \frac{1}{2}\langle(3\cos^2\theta_i - 1)\rangle \qquad \text{Equation 3}$$

The atomic numbering scheme applied for C*i* carbon atoms of the *sn*-1 palmitoyl and *sn*-2 oleyl chains of POPC is presented in Scheme 12:

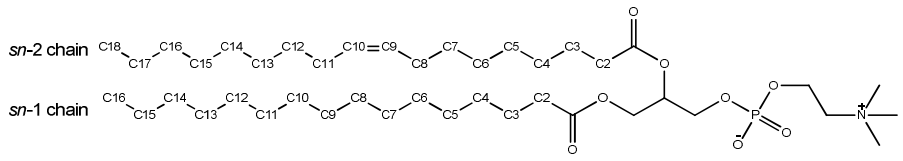

Scheme 12

The experimental data regarding the *sn*-1 palmitoyl chain is described by an $|S_{CD}|$ value of ~0.2 for the atoms between C2 and C8, and then smoothly decreasing until C16 has an $|S_{CD}|$ value of ~0.02. The *sn*-2 oleyl chain presents experimental values of $|S_{CD}|$ ~0.1 for C2, ~0.19 for C4 and lower values for C9 and C10 ($|S_{CD}|$ ~0.02), where the double bond is present; then slightly higher values are reported for C11 and C12, and C15 presents an $|S_{CD}|$ value about 0.80, close to the value for the same carbon number in the *sn*-1 chain. Noteworthy, is the fact that higher order parameters are registered for the C-H bonds of the phospholipid chains closer to the interface with water.(138-140)

Regarding the analysis of the simulation *sn*-1 chain results and their comparison with the experimental results, it is clear that all systems had remarkably different values of $|S_{CD}|$ for every carbon atom. In the systems C and D (see Figure 33, left and right views. respectively), $|S_{CD}|$ values are above 0.35 for some carbon atoms, especially on those further away from the interface. In system B, represented in the right plot of Figure 32, $|S_{CD}|$ values for atoms between C4 and C15 are above 0.4 and some are about 0.45 – more than double of the highest experimental $|S_{CD}|$ registered for those atoms. Only in system A, represented in the left plot of Figure 32, a closer agreement between theoretical and experimental results was achieved, although with higher values of $|S_{CD}|$. Also, only in the systems A and D the experimental inflexion between the $|S_{CD}|$ values in the first two atoms (C2 and C3) is present. A common feature between the four simulations is the rise in $|S_{CD}|$ from the chain carbon atoms closer to the interface to the atoms that are in the core of the bilayer and a sudden drop to an $|S_{CD}|$ value of ~0.1 in the methyl carbon of all systems.

Comparing the computed deuterium parameters with the few available experimental results for *sn*-2 oleyl chain, it is difficult to fully grasp which of the simulations is closer to the NMR results.(138-140) Results for system B (represented on the right plot of Figure 32) do match an $|S_{CD}|$ value, in C9 atom, while system C appears to correspond to the experimental result in the C2 atom. However, the results from system A, in the left view of Figure 32, closely reproduce the expected behaviour of $|S_{CD}|$ in the *sn*-2 chain, and present the higher $|S_{CD}|$ values for the carbon atoms closer to the interface. Systems B, C and D all present higher $|S_{CD}|$ values towards the end of each chain, *i.e.*, near the bilayer core.

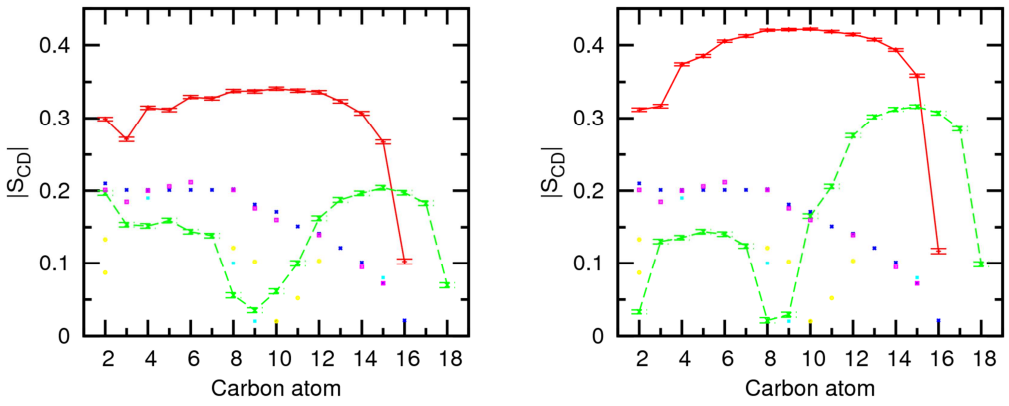

Figure 32 – Computed $|S_{CD}|$ for palmitoyl and oleyl chains for 15 ns of sampling for system A (left) and for system B (right). The $|S_{CD}|$ values calculated for the *sn*-1 chain are shown in red, while the values computed for the *sn*-2 chain are shown in green. The error bars associated with these results correspond to the standard error. The experimental results for the *sn*-1 chain were taken from refs. (138) – blue and (139) – magenta, while the results for the sn-2 chain were taken from refs. (140) – cyan and (139) – yellow.

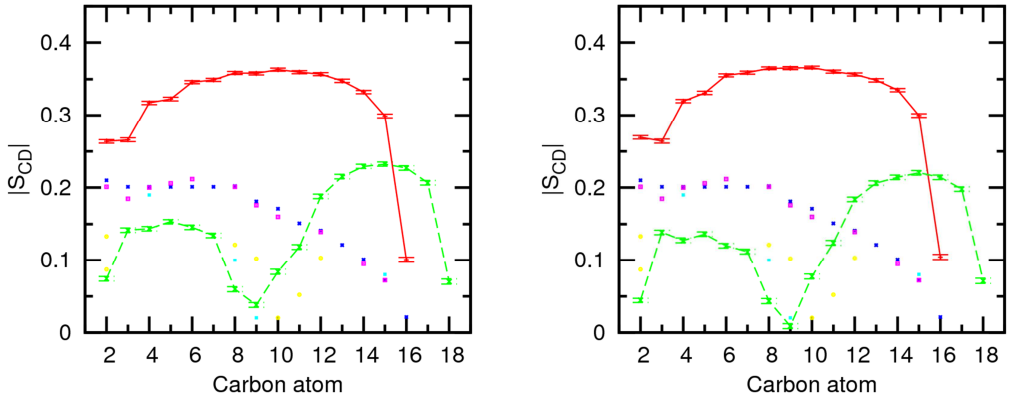

Figure 33 – Computed $|S_{CD}|$ for palmitoyl and oleyl chains for 15 ns of sampling for system C (left) and for system D (right). Remaining details as given in Figure 32.

Comparison with previous theoretical results (83, 87) was also performed, as can be seen in Figure 34 and Figure 35. From the comparison of the published computed $|S_{CD}|$ values for both *sn*-1 and *sn*-2 chains with the results of the MD simulations of the systems A to D, it is possible to notice that only system A (see the left panel of Figure 34) has results close to those previously published.

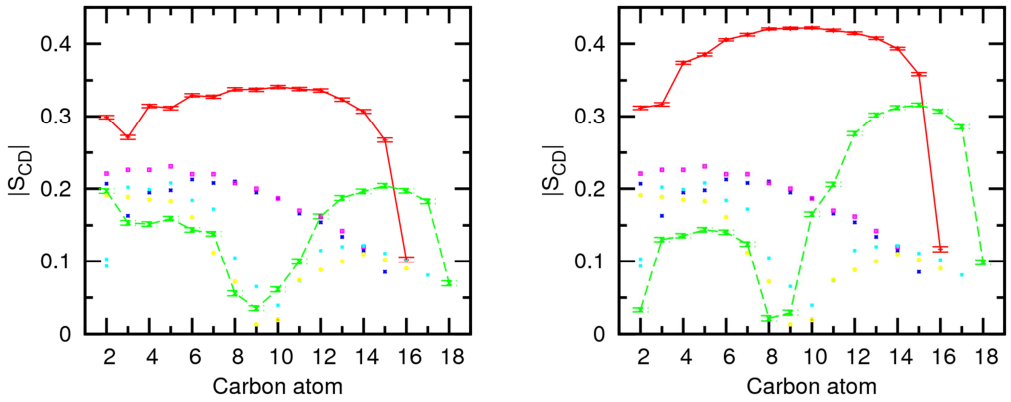

Figure 34 – Computed $|S_{CD}|$ for palmitoyl and oleyl chains for 15 ns of sampling for system A (left) and for system B (right). The $|S_{CD}|$ values calculated for the *sn*-1 chain are shown in red, while the values computed for the *sn*-2 chain are shown in green. The error bars associated with these results correspond to the standard error. The theoretical results for the *sn*-1 chain were taken from refs. (87) – blue and (83) – magenta, while the results for the sn-2 chain were taken from refs. (87) – cyan and (83) – yellow.

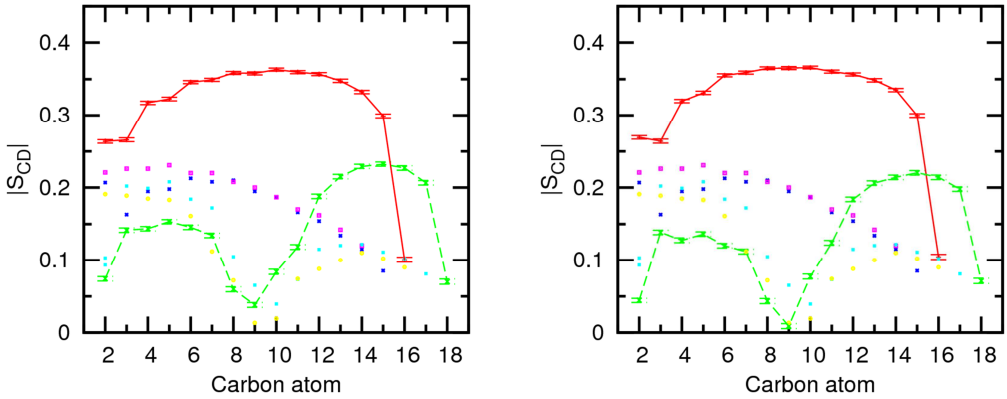

Figure 35 – Computed $|S_{CD}|$ for palmitoyl and oleyl chains for 15 ns of sampling for system C (left) and for system D (right). Remaining details as given in Figure 34.

Lateral diffusion

The diffusion of the lipid head groups through the membrane system is a kinetic parameter that can also be evaluated by means of molecular dynamics simulations, and is related with the restrictions of phosphate and choline groups experimented at the water/lipid interface, which are modulated by electrostatic interactions and hydrogen bonds.(141) The lateral diffusion (D_{lat}) for the NPT ensemble was calculated using the Equation 4:

$$D_{lat} = \frac{1}{2d} \lim_{t \to \infty} \frac{1}{t} \langle (x(t + t_0) - x(t_0))^2 + (y(t + t_0) - y(t_0))^2 \rangle \qquad \text{Equation 4}$$

In Equation 4, *x* and *y* correspond to the coordinates of the centre of mass of the atoms in the head groups, t_0 is the starting reference time and *d* represents the degrees of freedom (for the two-dimensional analysis, *d*=2).

The diffusion coefficients for the last 10 ns of the MD simulation time, presented in the left panel of Figure 36 to Figure 39 (where 0 ns corresponds to 140 ns of simulation time), for the simulations A to D, reveal the existence of two distinct diffusion domains: a short time domain and a long time domain. These domains were investigated fitting the mean square displacement (MSD) of the lipid head groups, defined by the non-hydrogen atoms of the choline and phosphate groups of POPC, from 0 to a given t, using time windows with different widths: till t=500 ps, five windows with a 100 ps difference; between t=500 and t=5000 ps, ten windows with a difference of 500 ps; and between t=5 ns and t=10 ns, five windows with a difference of 1 ns. These fittings, in the right plots of Figure 36 to Figure 39, converged at

different times, thus defining several short and long time domains for the different replicas of each system. In the systems A and C, the short time domain was defined between 0 and 4 ns, while the long time domain was defined between 4 and 10 ns. For the systems B and D, the short time domain was delimited between 0 and 7 ns for system B and between 0 and 8 ns for system D, meaning that the long time domain starts at 7 and at 8 ns for each system, respectively.

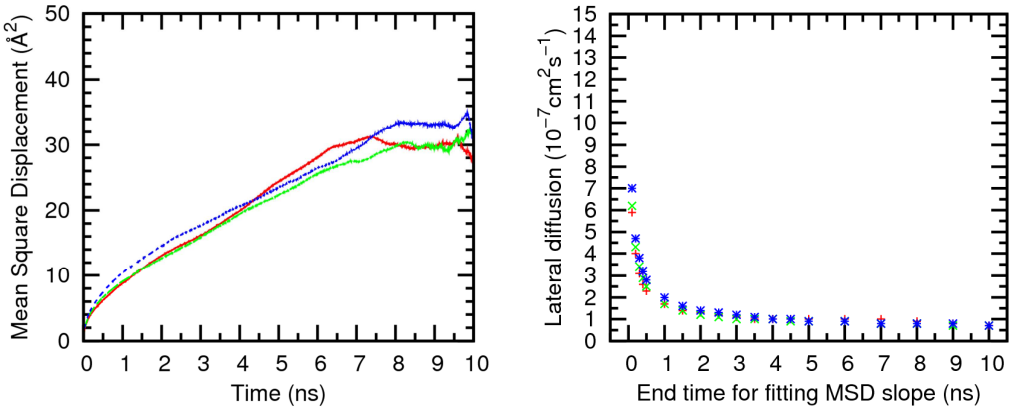

Figure 36 – Lipid diffusion coefficients for the last 10 ns of each replica MD simulation for system A (left plot) and MSD values calculated using different time windows (right plot). In both plots, red, green and blue colours stand for the first, second and third replica, respectively.

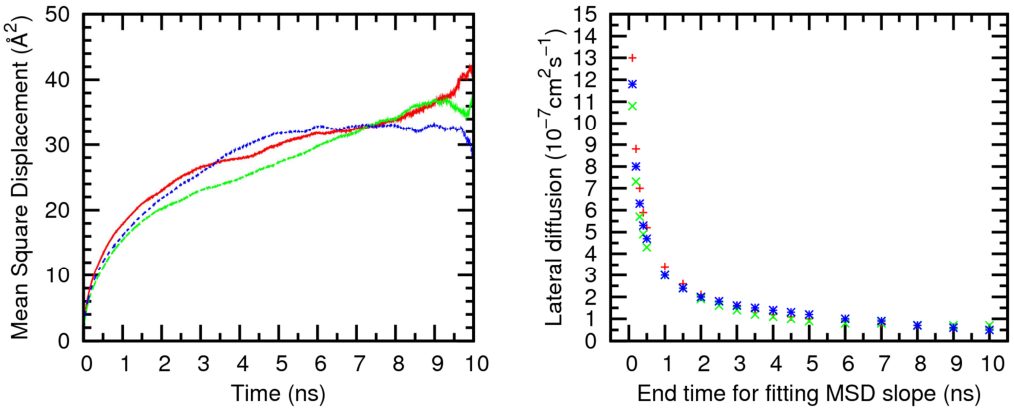

Figure 37 – Lipid diffusion coefficients for the last 10 ns of each replica MD simulation for system B (left plot) and MSD values calculated using different time windows (right plot). Remaining details as given in Figure 36.

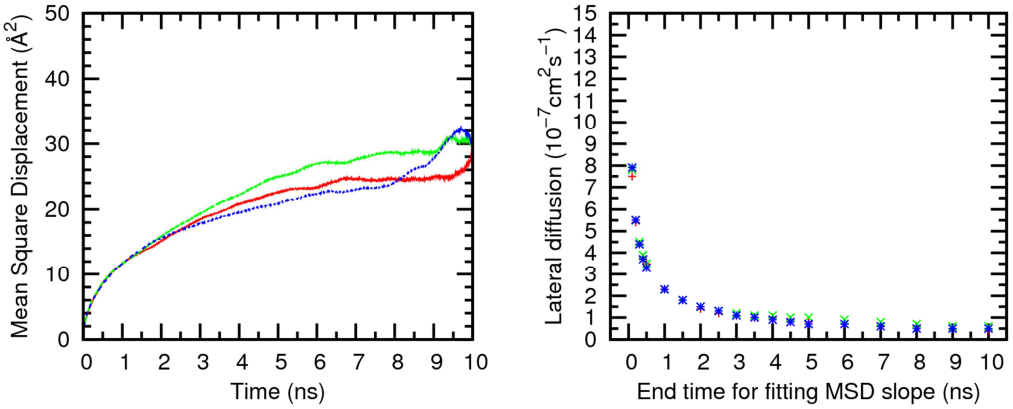

Figure 38 – Lipid diffusion coefficients for the last 10 ns of each replica MD simulation for system C (left plot) and MSD values calculated using different time windows (right plot).Remaining details as given in Figure 36.

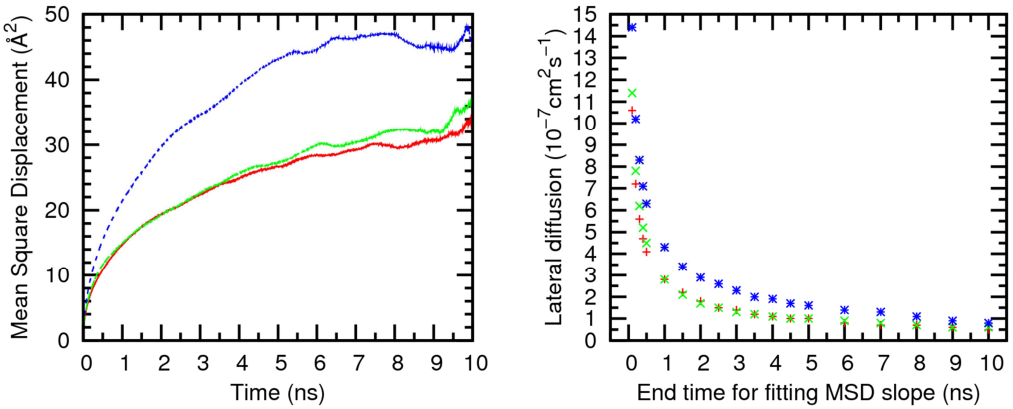

Figure 39 – Lipid diffusion coefficients for the last 10 ns of each replica MD simulation for system D (left plot) and MSD values calculated using different time windows (right plot). Remaining details as given in Figure 36.

The diffusion coefficient D_{lat} estimated for the short time domain was 1.0 × 10^{-7} cm^2s^{-1} for all three replicas of system A and ranged between 0.9 and 1.1 × 10^{-7} cm^2s^{-1} in the three MD simulation replicas of system C, as listed in Table 26. These simulations were performed with the SPC/E water model. In the MD simulations where the TIP3P water model was utilized, the values measured for diffusion coefficient D_{lat} ranged between 0.8 and 0.9 × 10^{-7} cm^2s^{-1} for system B, and between 0.7 and 1.1 × 10^{-7} cm^2s^{-1} for D. The values for the four systems are close to the lower limit of the experimental values (1.0 to 10 × 10^{-7} cm^2s^{-1}).(142, 143) On the long time domain, several replicas presented a diffusion coefficient *D* value below the experimental range values between 0.5 and 1.0 × 10^{-7} cm^2s^{-1}.(144-148) However, two replicas, one of system A and other of B, characterized with the unconstrained RESP charges, present the value of 0.6 and 0.7 × 10^{-7} cm^2s^{-1}, respectively, above the lower limit of the experimental range. Also, as seen in Table 26, in one MD replica simulation of the systems B

and D, characterized with the TIP3P water model, the MSD values for the long time domain assumed the values 0.0 and -0.1 × 10^{-7} cm^2s^{-1}.

Table 26 – Lateral diffusion coefficient for POPC lipid head groups, for each replica of the systems A to D.

System	*Short time domain (× 10^{-7} cm^2s^{-1})*			*Long time domain (× 10^{-7} cm^2s^{-1})*		
Experimental	1.0 to 10.0 (142, 143)			0.5 to 1.0 (144-148)		
Ref. (83)	5.5[a]			0.9		
	R1	*R2*	*R3*	*R1*	*R2*	*R3*
A[b]	1.0	1.0	1.0	0.4	0.5	0.6
B[c]	0.8	0.8	0.9	0.7	0.3	-0.1
C[b]	1.0	1.1	0.9	0.2	0.3	0.5
D[d]	0.7	0.7	1.1	0.5	0.5	0.0

[a] for the first 200 ps
[b] the short time domain is defined between 0 and 4 ns, while the long time domain is defined between 4 and 10 ns
[c] the short time domain is defined between 0 and 7 ns, while the long time domain is defined between 7 and 10 ns
[d] the short time domain is defined between 0 and 8 ns, while the long time domain is defined between 8 and 10 ns
R1 – Replica 1
R2 – Replica 2
R3 – Replica 3

Hydration of the water/lipid interface

Following the analysis for the diffusion coefficient D_{lat} dependent on the water molecules surrounding the lipid head groups, the hydration of each head group was assessed during the last 1 ns of each replica, calculating the average water solvation shell within 3.5 Å of the head group. The results obtained for the systems A to D are summarized in Table 27. The average number of water molecules, varying between 11.4 for system A and 12.8 for system C, agrees well with the experimental value of 12 water molecules per lipid head group, (refs. (149, 150) cited in (83)) as well as with the average 13.4 ± 0.2 water found by Martinek and Jójárt in their POPC membrane simulation.(83) In other words, the average number of water molecules seems to not depend on the simulation conditions, given how close they are. Furthermore, the P-O RDF between the phosphorus atoms in the head groups and oxygen atoms of the water molecules clearly shows that up to 3.0 Å from the phosphorus atoms, no water molecules are present and that the first hydration shell, defined by a sharp peak, is between 3.8 and 3.9 Å from that origin. Two other solvation shells appear between 5.7 and 6.2 Å and between 8.3 and 8.6 Å radii, as shown in Figure 40. Also, albeit lipid head group hydration results from

Martinek and Jójárt are comparable, it is not defined in their work how the head group was defined for assessment of the head group hydration or of the lateral diffusion.

Table 27 – Solvation of POPC lipid head groups within a 3.5 Å radius.

System	*Water molecules*
Experimental (149, 150)	12
Ref. (83)	13.4 ± 0.2
A	11.4 ± 0.4
B	12.7 ± 0.4
C	12.8 ± 0.3
D	12.4 ± 0.5

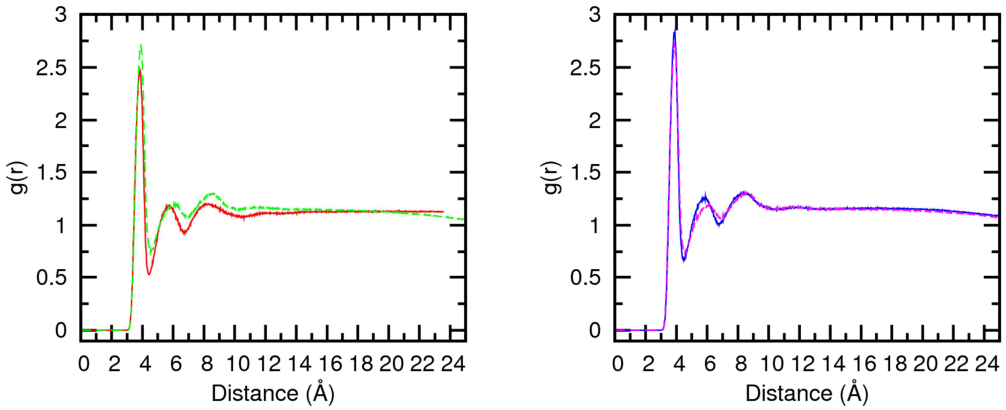

Figure 40 – P-O RDF of water molecules around lipid head groups in three replica MD simulations of the systems A and B (left view) and in three replica MD simulations of the systems C and D (right view), for the last 1 ns of the MD simulation time. The following line colour scheme was employed: system A in red, B in green, C in blue and D in magenta.

Summing Up

The average values for four of the seven biophysical parameters evaluated for the systems A to D are summarised in Table 28. It is straightforward that among the parameter combinations employed, system A, with the unconstrained RESP charges for phospholipids and SPC/E water molecules, is the most suitable one to reproduce the experimental values of the majority of the assessed parameters, especially Area per lipid, Bilayer thickness, Electronic density

profile, Chain order and Lateral diffusion of lipid head groups. On the other hand, for the Volume per lipid, a less commonly analysed parameter in the POPC lipid simulations reported in the literature, a close value of the experimental reference at 303 K was obtained with system B, also with RESP charges, although with the TIP3P water model. In system D a Hydration of the water/lipid interface closer to the experimental one was found.

Table 28 – Comparison between the structural parameters for the phospholipid bilayer systems A to D.

Parameter	*System*				
	A	B	C	D	Experimental
Area per lipid ($Å^2$)[a]	65.55 ± 3.05	79.87 ± 3.29	73.80 ± 2.48	78.34 ± 3.09	66[c]
Volume per lipid ($Å^3$)[a]	1248.9 ± 23.8	1262.4 ± 10.6	1251.8 ± 19.2	1271.2 ± 11.4	1256[d]
Bilayer thickness (Å)[a]	37.1 ± 1.4	31.7 ± 0.9	33.7 ± 1.4	32.3 ± 0.8	37 [d]
Head group hydration[b]	11.4 ± 0.4	12.7 ± 0.4	12.8 ± 0.3	12.4 ± 0.5	12 [e]

[a] For the last 50 ns of each replica, totalling 150 ns of sampling time in system A to D
[b] For the last 1 ns of each replica, totalling 3 ns of sampling time in system A to D
[c] Value measured at 310 K(136)
[d] Values measured at 303 K (135)
[e] From ref. (149, 150)

In conclusion, the parameters defined by system A corresponded well to most of experimental values, indicating that the pair of conditions defined by the RESP set of charges and SPC/E water model is appropriate to simulate a bilayer model composed of POPC lipid molecules. Therefore, they were definitively selected for the subsequent simulations presented in the next sections.

3.1.2 Overhydrated free membrane simulation

Methodology

In order to accommodate $L^{26}\subset Cl^-$ or $L^{8}\subset Cl^-$ associations in the water slab as sketched in Figure 41, the pre-equilibrated lipid bilayer utilized in the previous simulations was extended along the *z* axis direction by the addition of 2712 molecules with *Packmol*.(113) An overhydrated membrane model with a high water molecules per lipid ratio (68.81) and composed of 72 POPC lipids and 4954 water molecules equally distributed by two water slabs was produced. Afterwards, this large system, containing 24510 atoms, was equilibrated

following the protocol previously employed for the fully hydrated membrane. The equilibrated box has two water slabs with thicknesses *ca.* 32 Å, permitting the insertion of either receptor in the centre of a water slab, and the use of a 10 Å cut-off for the van der Waals and electrostatics interactions.

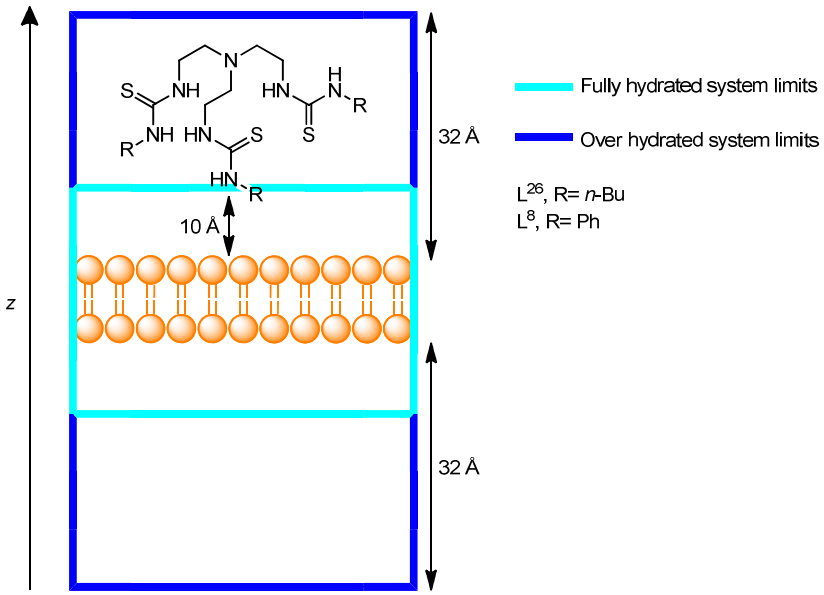

Figure 41 – Schematic comparison of the fully and overhydrated systems.

Results from this MD simulation are compared with both experimental results and results from system A, a fully hydrated system, to evaluate the eventual changes caused on the structure and dynamics of the membrane by the enlarged number of water molecules.

Results and discussion

The overhydrated system, henceforth called E, was also simulated for 150 ns. Unfortunately due to the computational cost associated with simulation of this large system, only a single replica was produced in the time available for this master thesis. However, two additional replicas are currently running in the Beowulf cluster. In these circumstances, the analysis of the simulation data is limited and the results obtained should be viewed as the first insights into the impact caused by the enlargement of water slabs in the biophysical membrane properties. A snapshot illustrative of this overhydrated simulation system taken at the end of simulation is presented in Figure 42.

The structural and dynamic biophysical parameters of system E will be evaluated following the methodology for the fully hydrated systems and compared with system A, also characterized with the unconstrained RESP atomic charges and SPC/E water model.

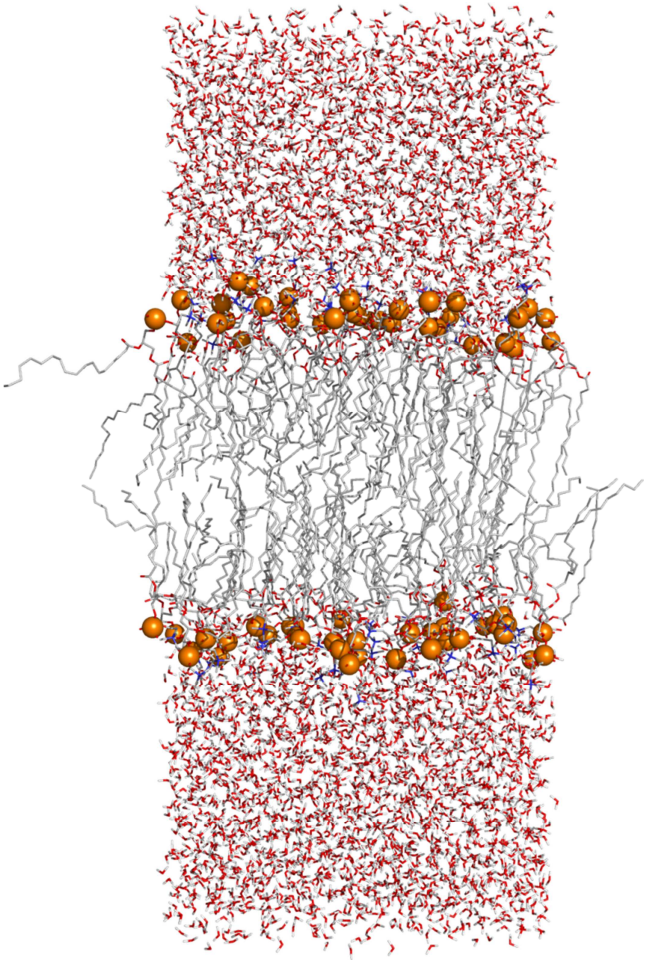

Figure 42 – Snapshot of a replica MD simulation of system E, at 150 ns.

Area per lipid

Similarly to the MD simulation replicas of the systems A to D, in the simulation of system E only the last 50 ns are considered to be equilibrated, in agreement with the variation of the area per lipid monitored throughout the 150 ns simulation time, shown in Figure 43. The average value of area per lipid is 60.18 ± 0.96 $Å^2$, below the 66 $Å^2$ experimental reference at 310 K, as well as the average value for system A (65.55 ± 3.05 $Å^2$), also shown in Figure 43. This comparison clearly indicates that the sampling of system E has to be increased with more simulation time and additional replicas. However, the remark is the proximity of the two

theoretical values, as expected, to demonstrate that increasing the number of waters in the system does not substantially change this physical property of the membrane model.

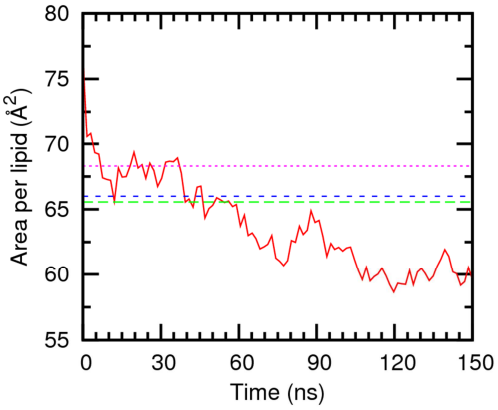

Figure 43 – Evolution of the Area per lipid in the MD simulation E (red line) and comparison with average value of area per lipid in from system A (green dashed line). Experimental references are also plotted as a blue dashed line (310 K) and as a magenta dotted line (303 K). Data was smoothed with Bézier curves.

Volume per lipid

The average value of volume per lipid in the last 50 ns of the MD simulation time was 1225.3 ± 6.8 Å^3, a value below the 1256 Å^3 experimental reference at 303 K, but within the range of 1194.6 to 1297.8 Å^3 found for system A, with an average value of 1248.9 ± 23.8 Å^3. This is depicted in Figure 44, where the values of the volume per lipid in system E are below the reference value at 303 K and the average of system A.

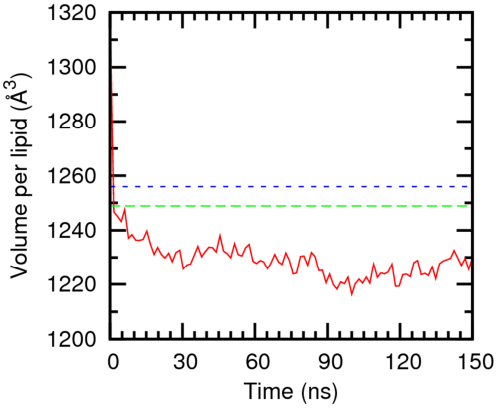

Figure 44 – Evolution of the Volume per lipid in the MD simulation E (red line) and comparison with average value of volume per lipid in from system A (green dashed line). Experimental reference is also plotted as a blue dashed line (303 K). Data was smoothed with Bézier curves.

Bilayer thickness

The evolution of the bilayer thickness for system E, during the entire time of the MD simulation, is plotted in Figure 45, revealing that this structural parameter is stable for the last 50 ns, as found for the previous ones. As the average area per lipid estimated for system E is lower than that for system A, and remembering the inverse relation between area per lipid and bilayer thickness, it was expected that bilayer thickness would be higher for system E. This is corroborated by the average bilayer thickness during the last 50 ns of 39.5 ± 0.5 Å, which indicates that the distance between the phosphorus atoms on each monolayer is 2.4 Å longer than in system A, with an average distance of 37.1 ± 1.4 Å. Indeed, the average of the three replicas of system A corresponds to higher bilayer thickness through the MD simulations than the system E, as illustrated in Figure 45. However, bilayer thicknesses are not substantially different.

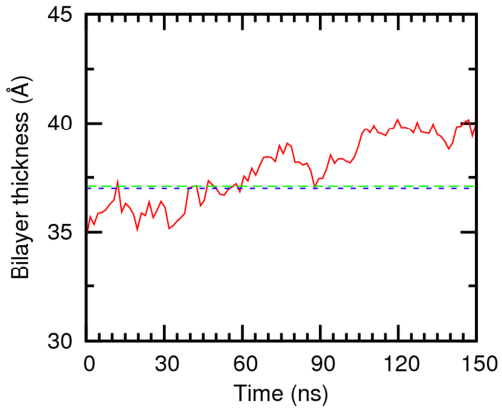

Figure 45 – Evolution of bilayer thickness in the MD simulation E (red line) and comparison with average value of bilayer thickness from system A (green dashed line). Experimental reference is also plotted as a blue dashed line (303 K). Data was smoothed with Bézier curves.

Electron density profile

The electron density profiles of system E, calculated with the last 10 ns simulation data, are plotted in Figure 46 along with the experimental profile at 303 K and the system profile of A. The three electron density profiles of E reflect the overall phospholipid bilayer membrane structure, as explained above for the systems A to D.

Regarding the comparison of the electronic density profile of system E (red line) with the experimental profile one (see Figure 46, left), it is noteworthy the good match of these two profiles throughout the *z* axis, especially in the bilayer region, between the polar heads of the POPC phospholipids. This is in contrast with the density profile of system A (see Figure 46,

right), which has a slight elevation in middle of the bilayer, suggesting the close packing of the terminal methyl of two opposite phospholipid chains (see above), while the density profile of E fits perfectly well in this apolar bilayer region. In other words, in system E, the neighbouring methyl groups from two individual lipid layers are displaced relatively to each other. This structural insight is corroborated by the layer thickness given by the distance between two peaks determined by polar phospholipid head groups of system E (37.7 Å), which is 3 Å larger than in system A (34.7 Å). Therefore, the larger number of water molecules in the system seems to have a small effect in this physical parameter of the studied membrane model.

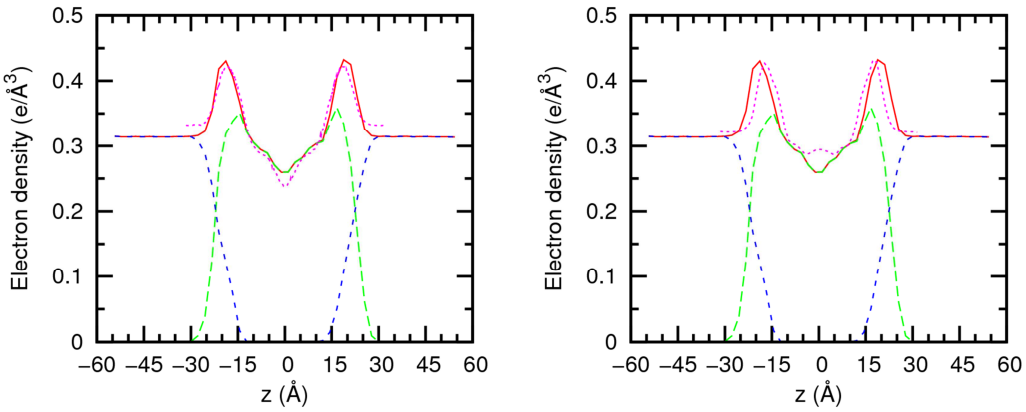

Figure 46 – Electron density profile of system E calculated for the last 10 ns of the MD simulation time in comparison with the experimental (left, magenta profile) and the electron density profile for system A (right, magenta profile). The colours red, green and blue stand for the system, POPC lipid and water electronic profiles.

Chain order

In the previous MD simulations of the systems A to D, corresponding to the fully hydrated membrane model, chain ordering was the parameter that presented the most different results when compared with the experimental ones. For system E this is no longer the case, as can be seen in the left plot of Figure 47. Regarding the analysis of the *sn*-1 chain (identified in Scheme 12) results and comparison with the experimental results, it is clear that values of $|S_{CD}|$ are higher than experimental values on every carbon atom of the chain, with $|S_{CD}|$ values above 0.3. Comparison of the computed deuterium parameters with the available experimental results for *sn*-2 oleyl chain (identified as well in Scheme 12), yields better matches, especially on the first atom, C2, and near the double bond (atoms from C8 to C12). In system E, the computed $|S_{CD}|$ values are higher when the carbon atoms are closer to the water/lipid interface and lower towards the bilayer core, in agreement with the experimental results. Results from

MD simulations of the systems E and A are compared in the left plot of Figure 47, where $|S_{CD}|$ values from system A, for both chains, are higher in the core of the bilayer.

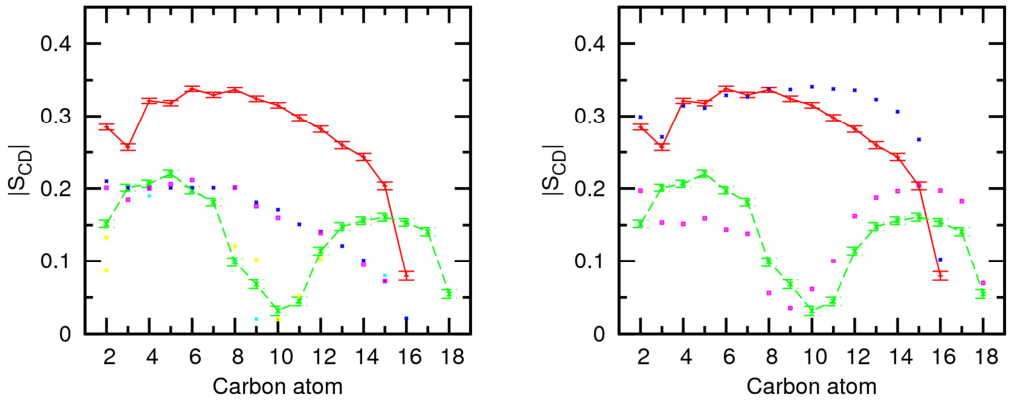

Figure 47 – Computed $|S_{CD}|$ for palmitoyl and oleyl chains for 5 ns of sampling for system E are show in the left plot. The $|S_{CD}|$ values calculated for the *sn*-1 chain are shown in red, while the values computed for the *sn*-2 chain are shown in green. The error bars associated with these results correspond to the standard error. The experimental results for the *sn*-1 chain were taken from refs. (138) and (139) and are presented as blue and magenta points, while the results for the *sn*-2 chain were taken from refs. (140) and (139) and are presented as cyan and yellow points. In the right plot, the computed $|S_{CD}|$ for system E (*sn*-1 chain in red, *sn*-2 chain in green) are compared with the computed $|S_{CD}|$ for system A (*sn*-1 chain in blue points, *sn*-2 chain in magenta points).

Lateral diffusion

The evaluation of the diffusion of the lipid head groups was also assessed in the MD simulation of system E. Similar to the MD simulation of system A, for the last 10 ns of simulation time (where 0 ns corresponds to 140 ns of simulation time), it is possible to see in Figure 48 (left plot), that the two distinct diffusion domains are present. Fitting the MSD curve of the lipid head groups in the same different time windows as before (till t=500 ps, with a raise of 100 ps; between t=500 and t=5000 ps with a raise of 500 ps; and between t=5 ns and t=10 ns with a raise of 1 ns), it was found that diffusion coefficient D_{lat} converged between 4 and 5 ns for system E, thus defining the long time domain in this simulation between 5 and 10 ns.

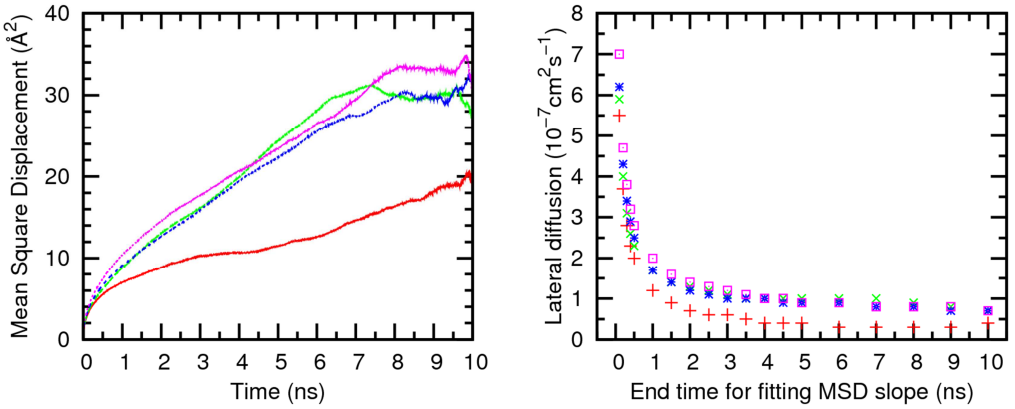

Figure 48 – Comparison of the Lipid diffusion coefficients calculated for the systems E and A, using the last 10 ns of the MD simulation data (left plot) and MSD values of these two systems using different time windows (right plot). In both plots, red stands for the single replica of system E, while green, blue and magenta correspond to each one of the three replicas of system A.

The diffusion coefficient D_{lat} estimated for the short time domain of system E for the first 5 ns is 0.4×10^{-7} cm^2s^{-1}, being lower than D_{lat} for system A (1.0×10^{-7} cm^2s^{-1}) and than the experimental values, ranging from 1.0 to 10×10^{-7} cm^2s^{-1}.(142, 143) On the long time domain, both simulations present diffusion coefficient D_{lat} values of 0.4×10^{-7} cm^2s^{-1}, below the experimental minimum of 0.5×10^{-7} cm^2s^{-1} in the interval 0.5 to 1.0×10^{-7} cm^2s^{-1}.(144-148) Despite the role of water molecules on the lateral diffusion of lipid head groups, the substantial increase of these molecules in both water slabs seems to have little effect in this parameter.

Hydration of the water/lipid interface

Following the analysis of the reduced short time domain diffusion coefficient D_{lat} for MD simulation of system E, hydration of each head group was assessed, also for the last 1 ns of simulation time, calculating the water solvation shell within 3.5 Å of the phospholipid head groups. The lipid head groups were found hydrated by an average number of 11.0 ± 0.2 water molecules, a value identical to the 11.4 ± 0.4 water molecules reported for system A. Moreover, the RDF for MD simulations A and E display identical profiles with three water shells occurring at *ca.* 3.8, 6.0 and 8.5 Å, as can be seen in Figure 49.

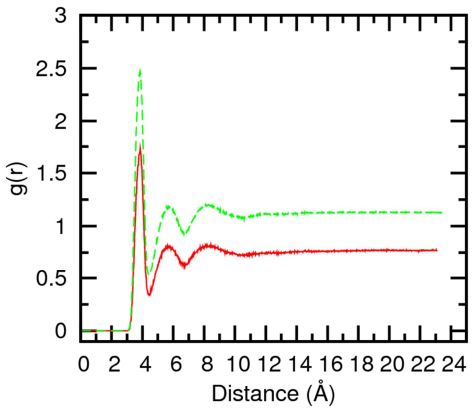

Figure 49 – Comparison of P-O RDF of the water molecules around lipid head groups for the systems E (red) and A (green), for the last 1 ns of the MD simulation time.

Summing Up

The comparison of some of the biophysical membrane parameters estimated from molecular dynamics simulation data of the *overhydrated* system E and *fully hydrated* system A (sharing the same atomic charges set and water model) done in the previous subsections, and summarized in Table 29, shows that the substantial enlargement of the water slabs with water molecules has a marginal impact in the structure and dynamics of the phospholipid bilayer.

Table 29 – Comparison between the structural parameters for the phospholipid bilayer systems E and A.

Parameter	*System*		
	E	A	Experimental
Area per lipid ($Å^2$)[a]	60.18 ± 0.96	65.55 ± 3.05	66[c]
Volume per lipid ($Å^3$)[a]	1225.3 ± 6.8	1248.9 ± 23.8	1256[d]
Bilayer thickness (Å)[a]	39.5 ± 0.5	37.1 ± 1.4	37 [d]
Head group hydration[b]	11.0 ± 0.2	11.4 ± 0.4	12[e]

[a] 50 ns of sampling in system E and 150 ns of sampling time in system A
[b] 10 ns of sampling in system E and 3 ns of sampling time in system A
[c] Value measured at 310 K(136)
[d] Values measured at 303 K (135)
[e] From ref. (149, 150)
*The system E is an overhydrated system equivalent to the system A as describe below.

Indeed, the area and volume per lipid and bilayer thickness all show small variations. On the other hand, the electronic density profile and order parameters both have shown better results

in the MD simulation of system E, getting closer to the experimental values than in the MD simulation replicas of system A regarding the lipid bilayer. In what concerns the lateral diffusion of the lipid head groups, as well as the hydration of the water/lipid interface, small changes were found, but deemed unimportant.

This system, composed of 72 POPC lipid molecules and 4954 water molecules was found to reproduce fairly well most of the experimental parameters available, and will be utilized to support the following MD simulations of membranes with receptors. With this section, the second major objective is finally fulfilled with simulation of system E, which enables the MD investigations of L^{26} and L^{8} diffusion across the phospholipid membrane.

3.2 Membranes and Receptors

To study the primary changes introduced by the presence of the two thiourea receptors inside the bilayer, one association of each ($L^{26}\subset Cl^-$ or $L^{8}\subset Cl^-$) was placed between the hydrophobic chains of the phospholipids, and then followed throughout MD simulations. On the other hand, to study whether the receptors are capable of bonding and penetrating the membrane, they were placed in the aqueous phase and left free of restrains to move around in the water slabs. Thus, two independent systems were built for both receptors, listed in Table 30 with the simulation conditions employed.

Table 30 – Summary of the simulations conditions of the membrane systems with L^{26} and L^{8}.

System ID	Receptor	Starting position of the receptor	Temperature (K)	Surface tension γ^a(dyn/cm)	Water model	Atomic Charges
F	L^{26}	Within the bilayer	310	60	SPC/E	RESP
G	L^{8}					
H	L^{26}	In the water slab				
I	L^{8}					

[a] Surface tension applied per bilayer.

The main goals of the MD simulations reported below are summarised as follows:

- For the systems F and G are to:
    - Evaluate the effect of the inserted receptor in the membrane properties;
    - Observe the behaviour of either chloride association when placed in the hydrophobic core of the bilayer.
- For the systems H and I are to:
    - Understand the behaviour of the chloride associations when near a lipid bilayer;
    - Eventually, if the association reaches the bilayer, evaluate the effect of the inserted association in the membrane properties.

Methodology

Due to bad contacts and to eventual chains crossing the phenyl rings of L^8, it was found difficult to place each receptor inside of the phospholipid bilayer, using a frame extracted from the equilibrated system E. So, another option was found: to use the CHARMM online membrane builder (151) to prepare a 72 POPC lipid bilayer with a pore large enough (diameter of ~20 Å) to accommodate either association ($L^{26}\subset Cl^-$ or $L^8\subset Cl^-$) within the bilayer. Afterwards, the systems were solvated with *Packmol*, to achieve the same number of water molecules as in the overhydrated system E (4954 water molecules). The charge neutrality was obtained by the addition of sodium, which was described by electrostatic and van der Waals interactions with parameters developed to be employed along with the SPC/E water model, taken from ref. (112). The tool *acpype.py* was applied to convert the sodium, $L^{26}\subset Cl^-$ and $L^8\subset Cl^-$ AMBER topology and coordinate files into GROMACS format.

These systems, containing either $L^{26}\subset Cl^-$ or $L^8\subset Cl^-$, were applied in the subsequent preparation stage, in which each anion association was accommodated between the aliphatic chains of phospholipids, as follows.

Preparation stage

The initial system configuration, with a pore in the bilayer and ordered water slabs, was submitted to 10000 steps of molecular mechanics energy minimisation using the steepest descent algorithm, and keeping the chloride association fixed by the application of a positional restrain of 200000 kJ mol^{-1} nm^{-2}. After this minimization, a short MD run of 250 ps at 310 K in a NPT ensemble was performed with the chloride association kept fixed with a 4000 kJ mol^{-1} nm^{-2} restrain. The time step of 1 fs was utilized and the system surface tension was maintained at 40 dyn/cm. After this NPT run, a few water molecules migrated to the middle of the lipid bilayer and were subsequently removed and relocated in the water slabs. At this stage the initial bilayer pore was closed, with the chloride association well accommodated among the apolar chains of the phospholipids. The system was again energy minimised with a positional restrain of 200000 kJ mol^{-1} nm^{-2} on the chloride association, through the 100000 steps of MM, using the steepest descent method, followed by the relaxation of the entire system for another 100000 steps, with the same algorithm. The equilibration of the system proceeded by means of a MD run at 310 K in a NPT ensemble and with the chloride association kept fixed with a positional restraint of 4000 kJ mol^{-1} nm^{-2} for 4 ns. The remaining simulation details for this preparation stage are as previously given (see *Simulation conditions* for the systems A to D), except the surface tension of 50 dyn/cm.

Simulation of the systems F and G

The final structure of the previous preparation stage was energy minimized following the protocol described earlier. Subsequently, the system was heated in a NVT ensemble from 0 to 310 K, for 50 ps (25000 steps), with the chloride associations fixed with a 4000 kJ mol^{-1} nm^{-2} restraint. Afterwards, the system was submitted to a NPT simulation run of 1 ns, using a time step of 2 fs. The positional restrain was removed and the simulation continued for further 150 ns using a NPT ensemble. The remaining simulation protocol was as previously given. These MD simulation runs with NPT ensemble were carried out with a surface tension of 60 dyn/cm.

Simulation of the systems H and I

For the simulations where the chloride associations $L^{26}\subset Cl^-$ and $L^{8}\subset Cl^-$ are solvated in the water slabs, the last structure of the *Preparation Stage* was edited with the GROMACS tool *editconf*, and the chloride associations were moved from the middle of the bilayer to the water slab, positioned at a distance from the closest water/lipid interface that enabled the use of a 10 Å cut-off. These systems were equilibrated following the protocol given above.

Results and discussion

While this thesis was being written, only a single replica of the systems F to I was available for analysis, due to time constraints. Nevertheless, as off this moment, each system is already being replicated at least two times.

Initial and final snapshots of the systems F and G

Figure 50 presents two snapshots showing the position of the chloride and L^{26} at the start and at the end of the 150 ns of the MD simulation run. In the beginning, the chloride is encapsulated by L^{26} via hydrogen bonding interactions, in the middle of phospholipid bilayer, while in the end of the simulation, the receptor is positioned near of the water/lipid interface and the chloride is no longer inside the bilayer nor close to L^{26}, as seen in Figure 51. The diffusion process of both species will be discussed later.

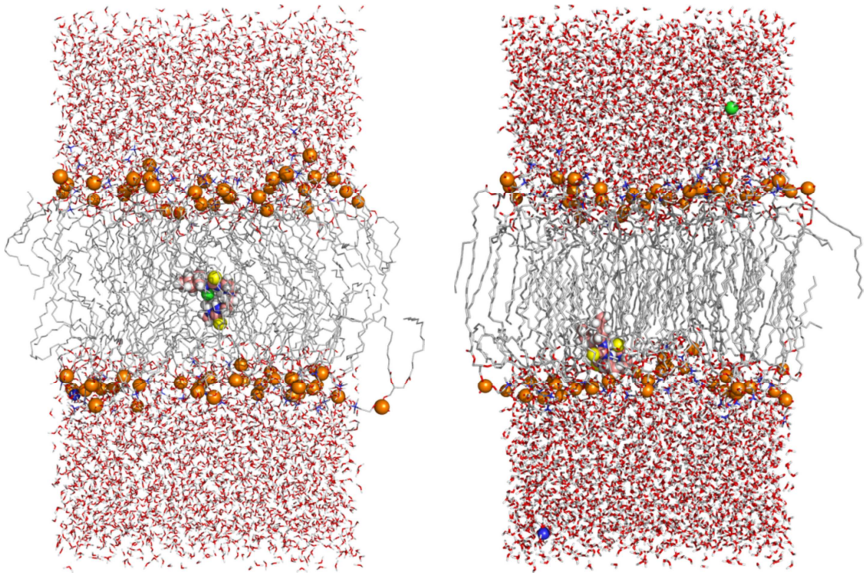

Figure 50 – Two snapshots of system F, taken at 0 (left) and 150 ns (right), showing the position of L^{26} and chloride in the beginning and in the end of this simulation run. L^{26} is drawn in space filling model with carbon atoms in salmon, sulfur atoms in yellow, hydrogen atoms in white and nitrogen atoms in blue. The chloride, sodium and phosphorus atoms from the phospholipids are represented as green, blue and orange spheres respectively, while oxygen and carbon atoms of the POPC lipids are drawn in red and grey lines. C-H hydrogen atoms in the POPC lipids have been omitted for clarity.

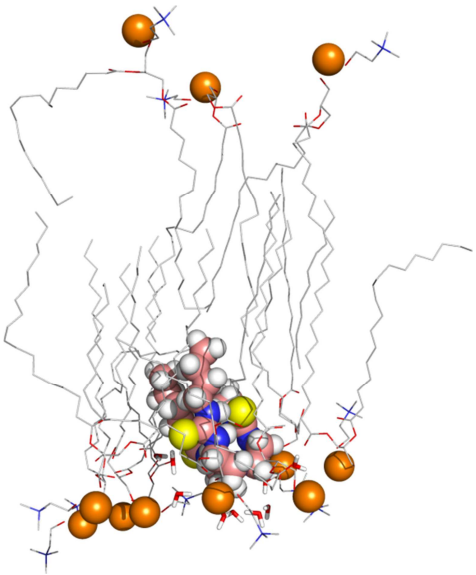

Figure 51 – Insight into the position of L^{26} at 150 ns of the MD simulation of system F, showing the receptor located near the water/lipid interface. C-H hydrogen atoms in the POPC lipids are hidden for clarity.

Figure 52 shows two snapshots taken at the beginning and at the end of the MD simulation of system G. In contrast with system F, in this single replica, the $L^8 \subset Cl^-$ association remains in the middle of phospholipid bilayer for 150 ns of the MD simulation with the chloride bonded to the receptor as shown in detail in Figure 53.

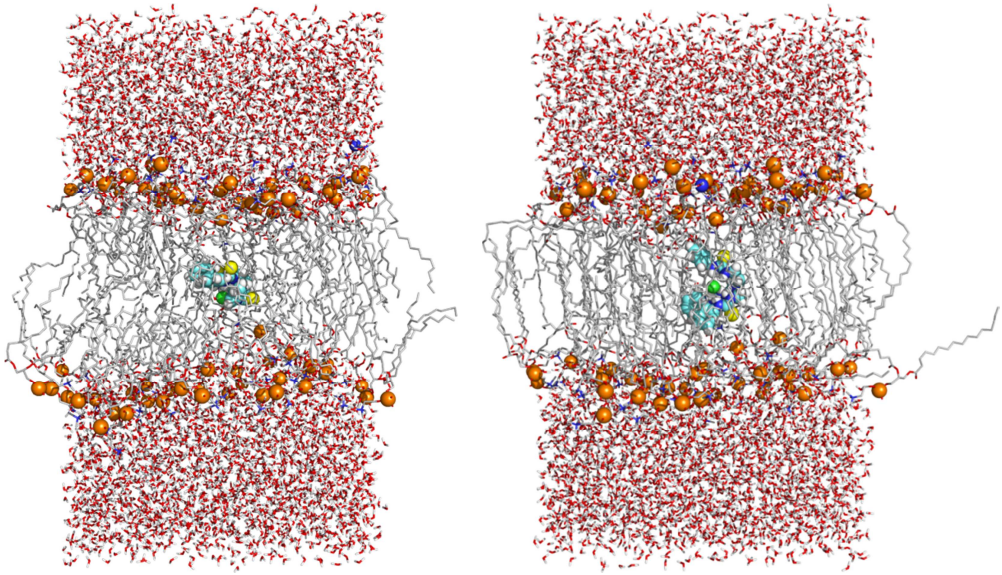

Figure 52 – Two snapshots of system G, taken at 0 (left) and 150 ns (right), showing $L^8 \subset Cl^-$ association located almost in the middle of phospholipid bilayer in both simulation times. L^{26} is drawn in space filling model with carbon atoms in cyan. Remaining details as given in Figure 50.

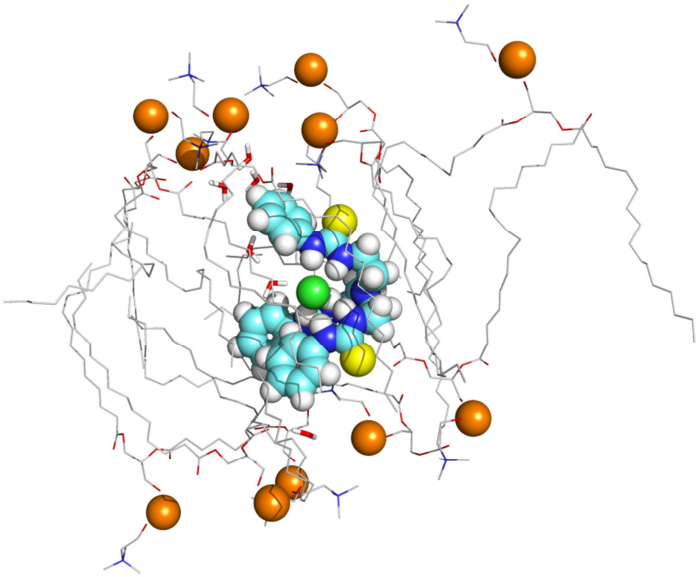

Figure 53 – Snapshot of system G at end of simulation, showing the $L^8 \subset Cl^-$ association surrounded by apolar phospholipid chains. Remaining details as given in Figure 51.

Initial and final snapshots in the systems H and I

In unconstrained MD simulations where chloride associations $L^{26}\subset Cl^-$ and $L^{8}\subset Cl^-$ were placed in the water slabs of the systems H and I, as shown by the corresponding snapshots taken at 0 and 150 ns of simulation run and presented in Figure 54 and Figure 55, in this order. Both receptors migrated from the water slab to the water/lipid interface during the simulation time. as revealed by the snapshots taken at 150 ns of simulation in the systems H and I, presented in the right panels of Figure 54 and Figure 55. A more detailed view of L^{26} embedded in the phospholipid bilayer of system H is shown in Figure 56, while the corresponding view for L^{8} in system I is shown in Figure 57. Further analysis will bring insights to the period of time it took for each receptor to internalize into the bilayer, as well as how this process occurred. Comparison with systems F and G will be done where appropriate.

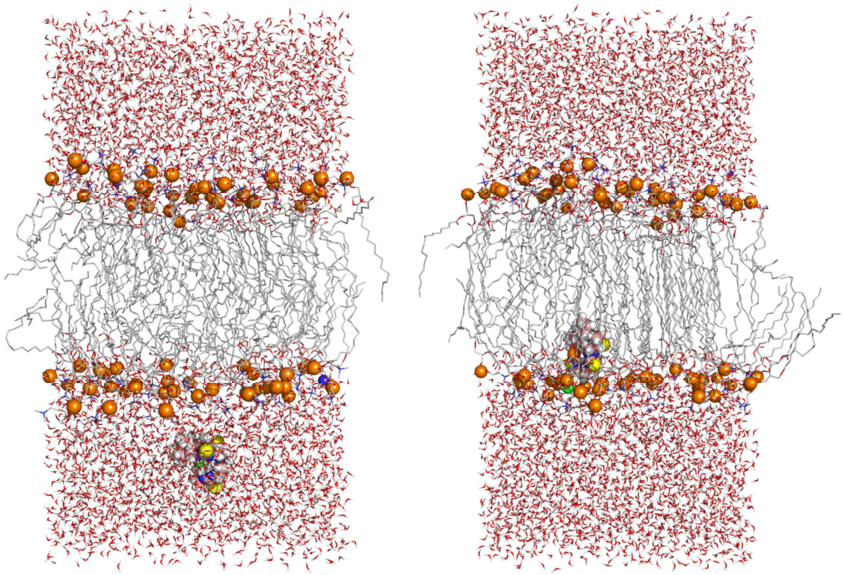

Figure 54 – Structure of system H recorded at 0 (left) and 150 ns (right) of the MD simulation. Remaining details as given in Figure 50.

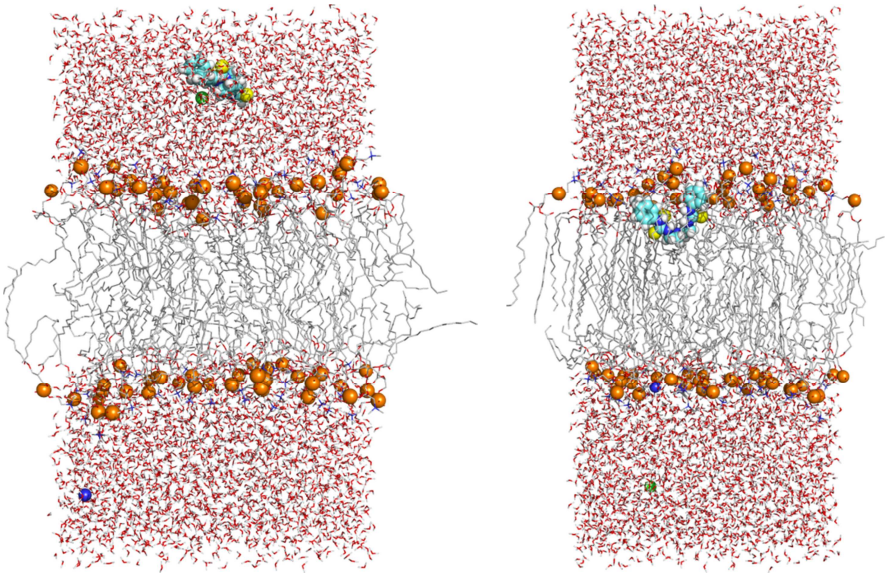

Figure 55 – Structure of system I recorded at 0 (left) and 150 ns (right) of the MD simulation. Remaining details as given in Figure 52.

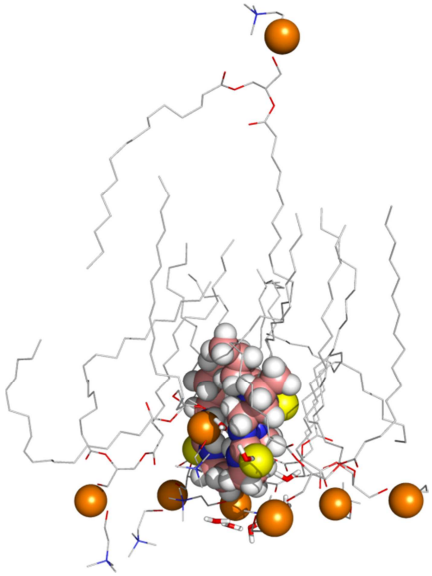

Figure 56 – Structure of system H taken at 150 ns of MD simulation time showing the receptor between phospholipids near of membrane interface. Remaining details as given in Figure 51.

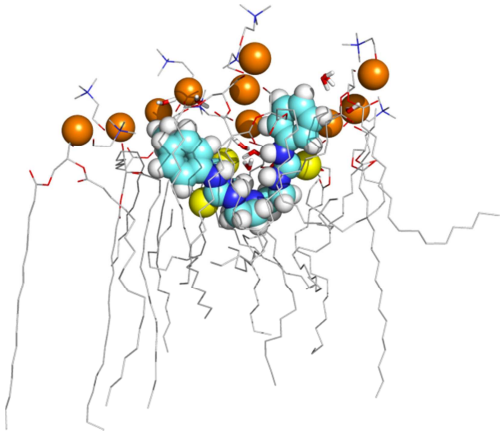

Figure 57 – Structure of system I recorded at 150 ns MD simulation time, showing the receptor between phospholipids near of the water/lipid interface. Remaining details as given in Figure 51.

In the following subsections, the evolution of the distance from the centre of mass of both receptors, defined by all non-hydrogen atoms, to the water/lipid interface will be analysed. The impact of the receptor within the phospholipid bilayer, on the structural and dynamic parameters of the membrane, will be assessed by the comparison with the results from the overhydrated system E.

Diffusion of the receptors within the membrane starting from the phospholipid bilayer

Tracking the distance of both receptors to the lipid-water interface[‡] is a way to evaluate the evolution of the MD simulation: if the receptor moves from its starting position and gets closer to the interface, that could be an indicator of whether or not it is capable of moving inside the membrane, even if it implies its disruption or other changes in the biophysical properties of the bilayer. In this context, the receptor position within the phospholipid bilayer was evaluated tracking the distance along the *z* axis (Figure 58) between the centre mass of the receptor and the origin of the periodic system, located at the external boundary of a water slab, henceforth mentioned as z_0•••L. The structural integrity of phospholipid membrane was assessed measuring the average distance of 36 phosphorus atoms in each monolayer relatively to the origin. These two individual distances are designated as z_0•••P_1 and z_0•••P_2. The variances in these three structural parameters for 150 ns are presented in Figure 58 for L^{26} and L^{8}. In

[‡] Distance is calculated between the centre of mass of a molecule, group or atom and the average *z* coordinate of the phosphorus atoms in the closest monolayer.

agreement with the MD dynamics events previously presented in Figure 50, L^{26} migrates to the water/lipid interface after *ca.* 10 ns of simulation (blue line, left plot) while L^{8} remains almost in the middle of phospholipid bilayer (blue line, right plot), in line with the representation in Figure 52. Furthermore, the average distances from the origin to the phosphorus atoms in the lipid polar heads (lines red and green), are roughly constant throughout the simulation time, indicating that the structural integrity of the model membrane is preserved in both systems in the presence of these two receptors (this point is recalled later).

In addition, the proximity of each receptor to the water/lipid interface (L•••P distance[§]) was evaluated measuring the distance in the *z* axis to the average coordinate of the phosphorus atoms in each monolayer. Thus, this parameter indicates the relative position of a receptor to a water/lipid interface defined by the positions of the phosphorus atoms in that monolayer, as shown in Figure 59 for L^{26} (left) and L^{8} (right). L^{26} is near of only one water/lipid interface during most of the simulation time, leading to an average L•••P distance of 5.4 ± 1.3 Å for the last 100 ns. In contrast, L^{8}, in this replica, is positioned preferentially near the middle of phospholipid bilayer, with an average L•••P distance of 14.3 ± 1.4 Å, during the entire simulation time. The stability in the position assumed by L^{26} or L^{8} is of paramount importance to consider each system equilibrated.

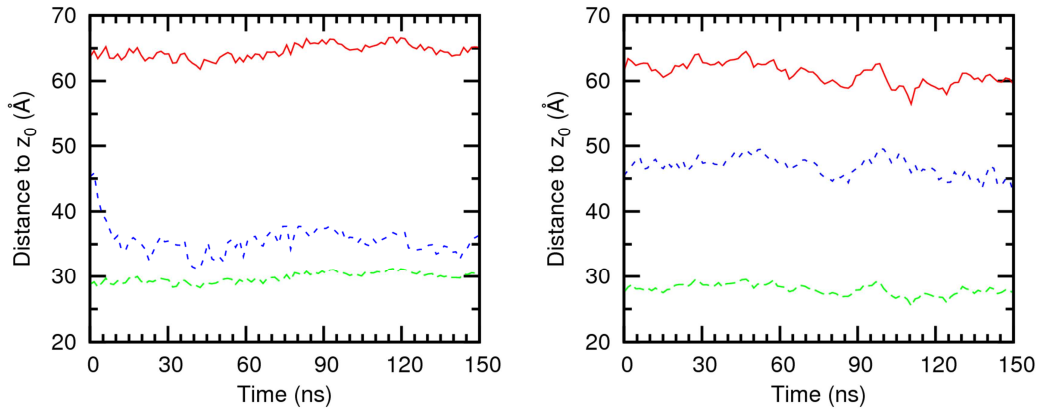

Figure 58 – Evolution of z_0•••L (blue), z_0•••P_1 (red) and z_0•••P_2 (green) distances for 150 ns of the MD simulation in the systems F (left) and G (right). Data was smoothed with Bézier curves.

[§] In plots, when L•••P distance assumes a negative value, it means that the analysed group is within the bilayer; when its value is positive, the group is present in the water phase of the system. A L•••P distance of 0 Å indicates that the analysed group is at the water/lipid interface.

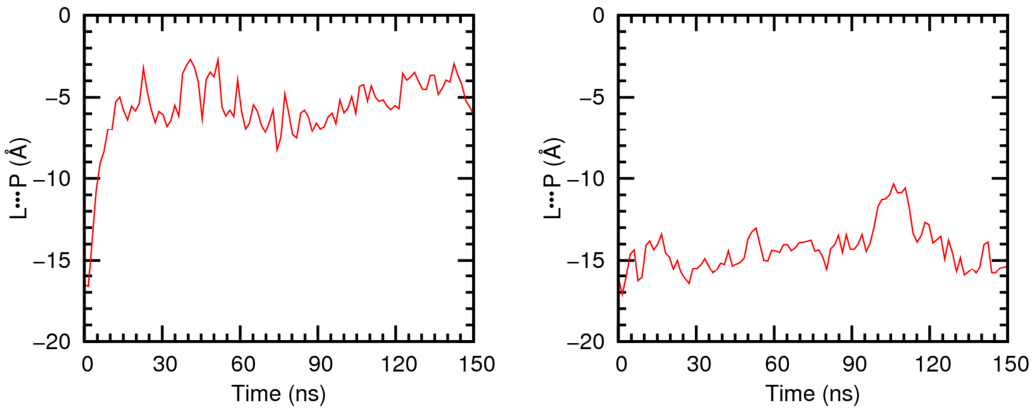

Figure 59 – Evolution of L•••P distances between L^{26} (left) and L^{8} (right) and the closest water/lipid interface thorough the simulation time, in the systems F and G, respectively. Data was smoothed with Bézier curves.

Diffusion of the receptors within the membrane starting from the water phase

The distance from each receptor to the closest water/lipid interface, as well as the tracking of the positions of L^{26} and L^{8} to that reference point was assessed like in the MD simulations for the systems F and G. As can be seen in Figure 60, in which z_0•••L, z_0•••P_1 and z_0•••P_2 distances are plotted for 150 ns, both L^{26} and L^{8}, initially positioned in the water slab, migrate towards the interface of the bilayer, at different simulation times, without disruption of the structure of the phospholipid bilayer. In addition, Figure 61 reveals that, in the single replica here reported, L^{26} has crossed the bilayer interface at 35 ns of simulation time, while L^{8} entered into the bilayer near the 80^{th} ns of simulation time. Figure 61 also includes the evolution of L•••P distances between L^{26} or L^{8} and the water/lipid interfaces in the systems F (left plot, green line) and G (right plot, green line), for comparison purposes. In spite of the different initial positions, as L^{26} enters the bilayer (system H, red line) or moves from its core (system F, green line), it assumes approximately the same position when the it reaches the water/lipid interface in both cases (see Figure 61, left). This structural insight is corroborated by the equivalent average distances of 4.7 ± 1.6 and 5.4 ± 1.3 Å in the replicas of the systems H and F, respectively, for the last 100 ns. The scenario in the right panel of Figure 61 is quite different, as L^{8} enters the bilayer (system I, red line) and assumes its position at an average distance of 4.3 ± 1.1 Å to the interface, calculated for the last 50 ns of the MD simulation, while on system G (green line) the average distance to the interface was 14.3 ± 1.4 Å. These observations indicate that the favourable positioning of either L^{26} or L^{8} is near the water/lipid bilayer, as observed in simulations of the systems F, H and I.

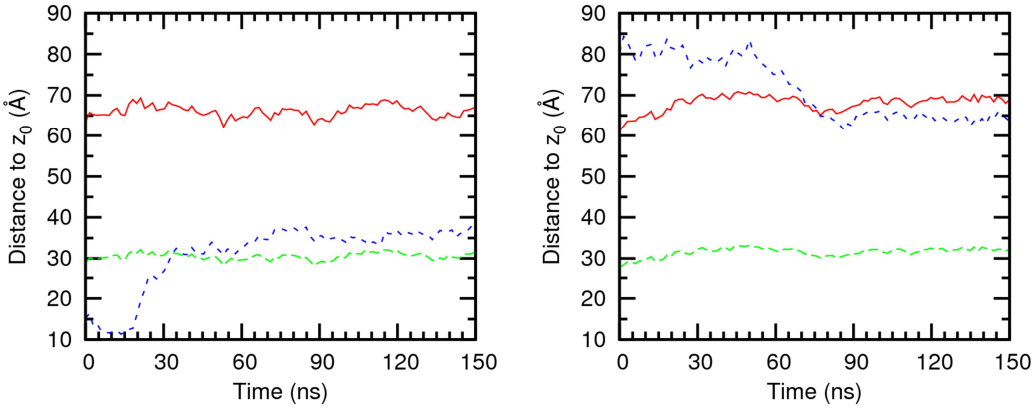

Figure 60 – Evolution of z_0•••L (blue line), z_0•••P_1 (red line) and z_0•••P_2 (green line) distances, showing the movement of L^{26} (left) and L^8 (right) from the water slab to the bilayer, for 150 ns MD simulations, in the systems H and I, respectively. Data was smoothed with Bézier curves.

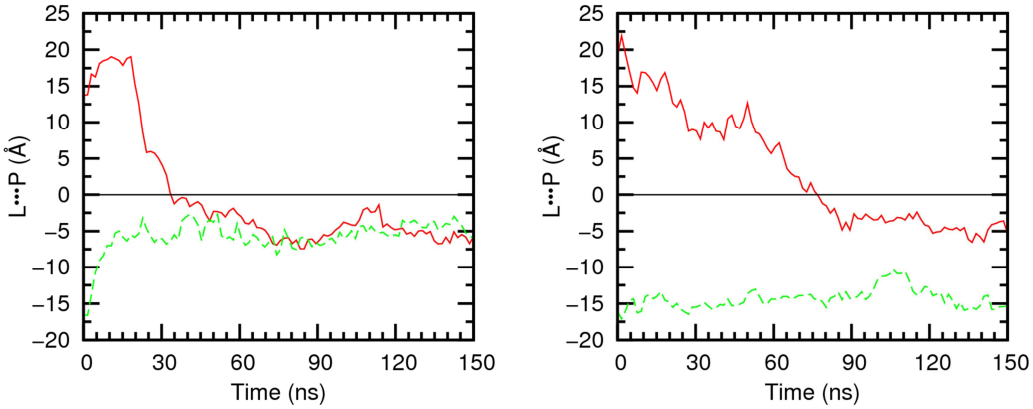

Figure 61 – Evolution of L•••P distance through the MD simulations of the systems H (red line) and F (green line) in left plot, and of the systems I (red line) and G (green line) in right plot. The black line represents the water/lipid interface closer to L^{26} or L^8. Data was smoothed with Bézier curves.

Complementary to the analysis of the evolution of distance between each receptor and the interface, and the time they entered the membrane, it is of crucial importance to understand how they perform that action, *i.e.*, how does each receptor face the membrane to permeate between the head groups and then became positioned below the phosphate groups of the bilayer. This process is illustrated with six successive snapshots, taken between 21 and 42 ns of simulation time in Figure 62 for system H. A single chain of L^{26} initially permeates between the head groups (represented by the phosphorus atoms), followed by a second chain. As the two chains are between several head groups, the tertiary nitrogen atom also gets between choline and phosphate groups, thus pulling the third chain of the receptor. As the three

thiourea chains are now between the POPC head groups, the receptor appears to be hydrogen bonded to the oxygen atoms of a phosphate group, while nested between the lipid molecules. The achieved position is close to the one presented in Figure 56.

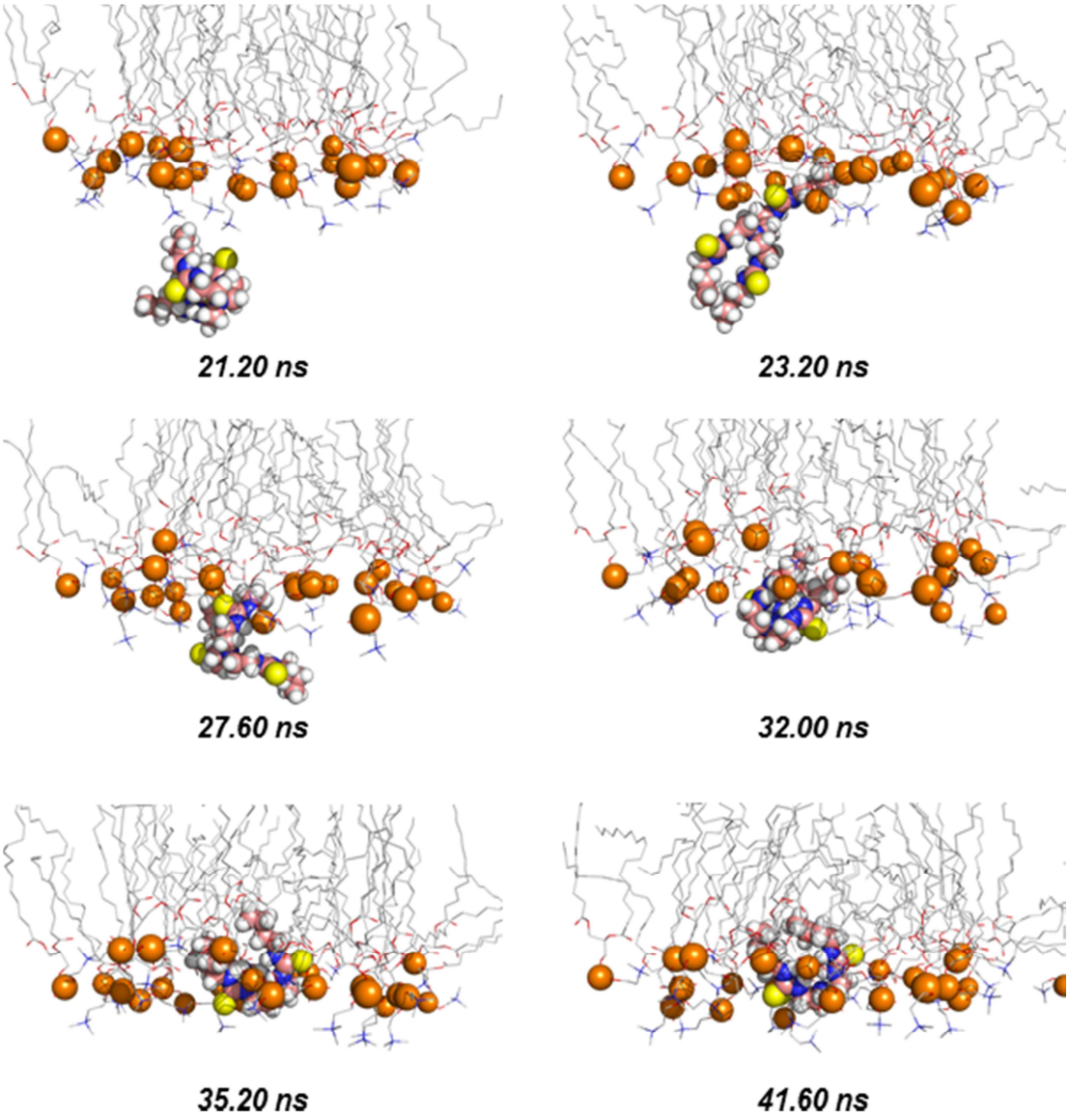

Figure 62 – Six frames of system H successively taken, showing L^{26} entering the phospholipid bilayer. Phosphorus atoms of the POPC lipids are represented as orange spheres, while nitrogen, oxygen and carbon atoms are represented in blue, red and grey. Water molecules and C-H atoms in the POPC lipids are omitted for clarity.

Concerning system I, the approach of L^8 to the phospholipid bilayer is somehow different, as depicted in Figure 63. L^8 faces the lipid head groups with the tripodal motif head approaching the bilayer, in opposition to the chain-based anchorage previously described for L^{26}, thus leaving the phenyl rings pointing to the water slab, as it goes deeper between the lipids. This orientation is maintained until the end of the simulation as shown in the snapshot of Figure 57. Furthermore, from the simulations performed with systems H and I, it is also evident that L^{26} and L^8 form hydrogen bonds to the oxygen atoms from the phosphate moieties, contributing to the final positioning of both receptors near the phosphorus atoms, as clearly illustrated by the red line in both views of Figure 61.

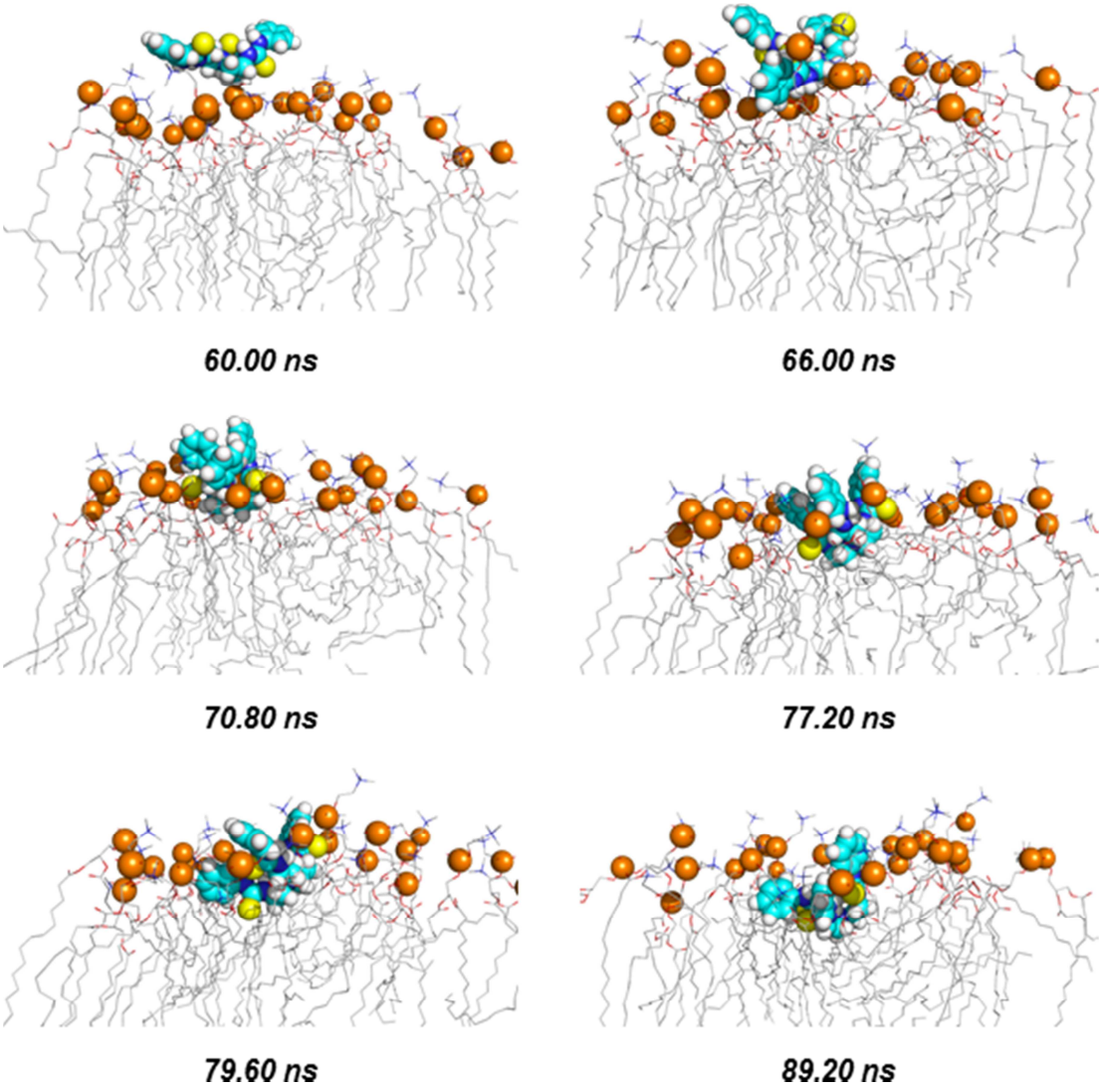

Figure 63 – L^8 entering the membrane in system I, starting from the water slab. Six successive frames are presented. Phosphorus atoms of the POPC lipids are represented as orange spheres, while nitrogen, oxygen and carbon atoms are represented in blue, red and grey. Remaining details as given in Figure 62.

Stability of the chloride associations in the membrane model

As is illustrated in Figure 51 above (right view), at the end of the simulation time, the chloride is no longer associated with L^{26} (system F), while in system G it is still associated to L^{8}, as shown in Figure 53 (right view), also above. Indeed, the association $L^{26}\subset Cl^-$ was stable during the initial 35 ns of the MD simulation of system F (for the replica reported), after which the chloride left the receptor, until the end of the simulation. During this initial period of simulation, the average $Cl^-\bullet\bullet\bullet N_c$ distance, between chloride and the centre of mass of L^{26} (defined by the six nitrogen binding sites, as in Chapter 2), was 1.47 ± 0.32 Å, which is comparable to the distance 1.35 ± 0.17 Å found in the simulation where $L^{26}\subset Cl^-$ was solvated in DMSO/water solution. Furthermore, the arrival of L^{26} to the interface and the release of the chloride do not occur simultaneously, as shown in Figure 64. However, the second event is dependent on the first one.

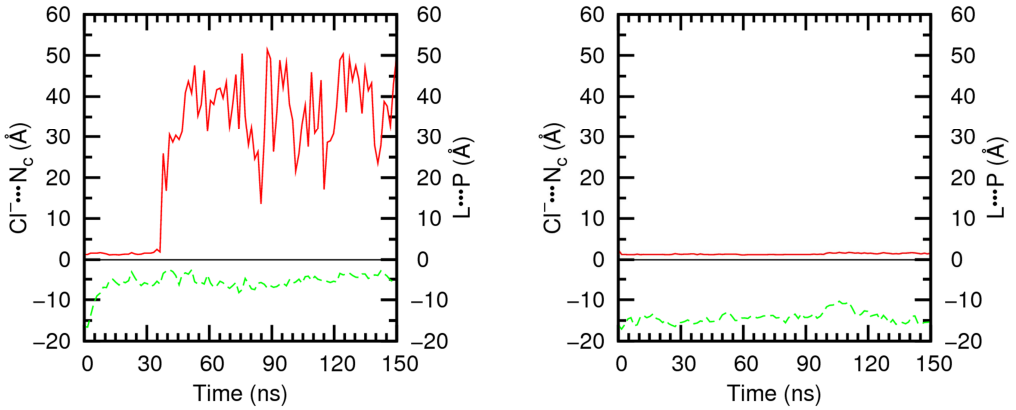

Figure 64 – Evolution of $Cl^-\bullet\bullet\bullet N_c$ distance of each receptor (red line), compared to the L•••P distance (green line), along the simulation of the systems F (L^{26}, left plot) and G (L^{8}, right plot). Data was smoothed with Bézier curves.

A further insight into the chloride release process is given by Figure 65, which precisely illustrates, with four sequential frames, how the chloride left L^{26}, from within the lipids to the water slab. When L^{26} is near of the phospholipid head groups, the tertiary nitrogen atom of the tren motif in the receptor is pointed towards the water/lipid interface, and the chloride is promptly released from the receptor to the water/lipid interface.

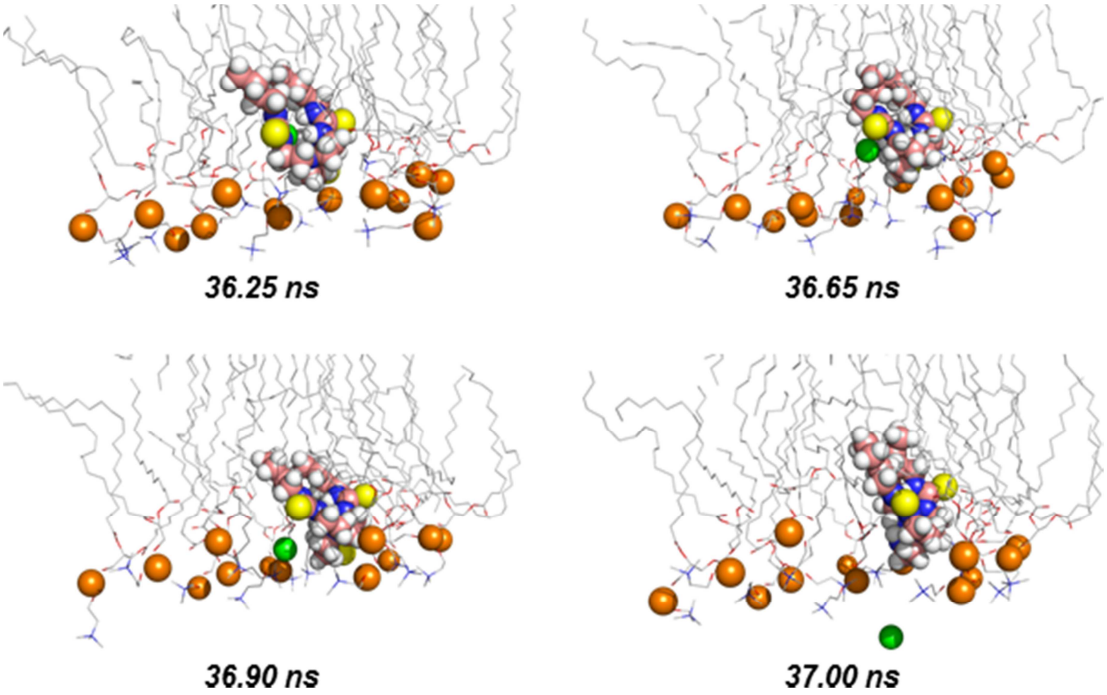

Figure 65 – Release of chloride from L^{26} (shown in salmon) in system F. Phosphorus atoms of the POPC lipids are represented as orange spheres, while nitrogen, oxygen and carbon atoms are represented in blue, red and grey. Remaining details as given in Figure 62.

Concerning the chloride association of L^8, it is rather stable through all of the 150 ns of simulation time. The average $Cl^-•••N_c$ distance between chloride and the centre of mass of L^8 is 1.40 ± 0.23 Å, coming in perfect agreement with the average distance of 1.40 ± 0.16 Å found when the association was solvated in DMSO/water solution. Furthermore, the hydrogen bonds formed between L^{26} or L^8 and the chloride were also evaluated during the time that each association is maintained (35 ns for system F and 150 ns for system G). This information is given in Table 31.

The dimension of the $N•••Cl^-$ distances and $N\text{-}H•••Cl^-$ angles presented in Table 31 are consistent with the formation of weak hydrogen bonds between each receptor and the chloride anion. It is important to note that these apparently different results for the systems F and G were obtained with a single replica and consequently have to be further substantiated with the analysis of subsequent replicas.

Table 31 – Dimensions of the parameters of N-H•••Cl^- hydrogen bonds with the standard deviations for L^{26} and L^8 chloride associations inside the POPC bilayer (systems F and G).

Dimension	*Binding site*	*L^{26}*			*L^8*		
		Min (Å)	Max (Å)	Mean ± Std Dev (Å)	Min (Å)	Max (Å)	Mean ± Std Dev (Å)
Distance	N1•••Cl^-	2.98	8.28	3.46 ± 0.35	2.96	5.86	3.39 ± 0.17
	N2•••Cl^-	2.98	7.38	3.46 ± 0.32	2.99	5.03	3.37 ± 0.14
	N3•••Cl^-	2.96	4.65	3.44 ± 0.17	2.96	5.92	3.42 ± 0.18
	N4•••Cl^-	2.98	5.29	3.38 ± 0.16	2.97	5.42	3.41 ± 0.17
	N5•••Cl^-	2.99	6.18	3.44 ± 0.18	2.96	6.31	3.37 ± 0.18
	N6•••Cl^-	2.96	5.07	3.34 ± 0.14	2.96	6.26	3.43 ± 0.19
Angle	N1-H•••Cl^-	80	180	155 ± 10	104	180	154 ± 10
	N2-H•••Cl^-	92	180	156 ± 10	102	180	155 ± 9
	N3-H•••Cl^-	97	180	153 ± 9	87	180	157 ± 9
	N4-H•••Cl^-	98	180	157 ± 9	99	180	157 ± 8
	N5-H•••Cl^-	97	180	154 ± 9	88	180	157 ± 9
	N6-H•••Cl^-	97	180	159 ± 8	91	180	154 ± 9

These values are calculated with *N*= 35000 observations for the $L^{26}\subset Cl^-$ association and with *N*=150000 observations for the $L^8\subset Cl^-$ association.

Stability of the chloride associations in the systems H and I

In agreement with the observations of chloride associations $L^{26}\subset Cl^-$ and $L^8\subset Cl^-$ solvated in water (simulations described in Chapter 2, *Molecular Dynamics Simulations in solution*), in the MD simulations of the systems H and I, the chloride anion has been released from L^{26} at about 400 ps of simulation time, while in the case of L^8 this event occurs before the beginning of the unscontrained MD simulation, as shown in Figure 66. Furthermore, as both events happen before either receptor reaches the bilayer, the release of chloride is deemed unrelated to internalization of L^{26} or L^8.

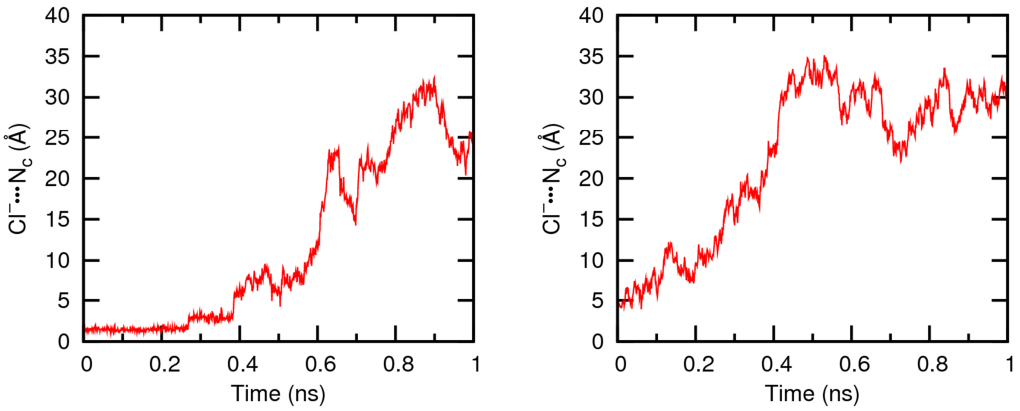

Figure 66 – Evolution of $Cl^-•••N_c$ distances for L^{26} (system H, left plot) and for L^8(system I, right plot) for the first ns of the MD simulation.

Area per lipid

The comparison of the evolution of the areas per lipid in the systems F, G and E through the 150 ns of the MD simulation, plotted in Figure 67, indicates that this biophysical parameter is perturbed by the presence of L^{26} and L^8 within the bilayer of each respective system. As for the corresponding overhydrated system free of receptors (system E), an initial period (50 ns) of the long NPT ensemble of system F was considered equilibration time and was discarded from the data. During the remaining 100 ns (see Figure 67, left plot), L^{26} is inside of the phospholipid bilayer, at an average distance of 5.4 ± 1.3 Å from the water/lipid interface, and the average area per lipid is 69.50 ± 1.25 $Å^2$. This value is deviated by *ca.* 9 $Å^2$ from the average 60.18 ± 0.96 $Å^2$ assessed in simulation E. In contrast, the area per lipid of system G (see Figure 67, right plot) shows a considerable variation during the course of the MD simulation, except for the last 50 ns. During this period, the average area per lipid is 76.47 ± 1.58 $Å^2$, differing expressively from the value of system E, indicating that $L^8⊂Cl^-$ and the water molecules surrounding it caused a great effect in the structure of the membrane model.

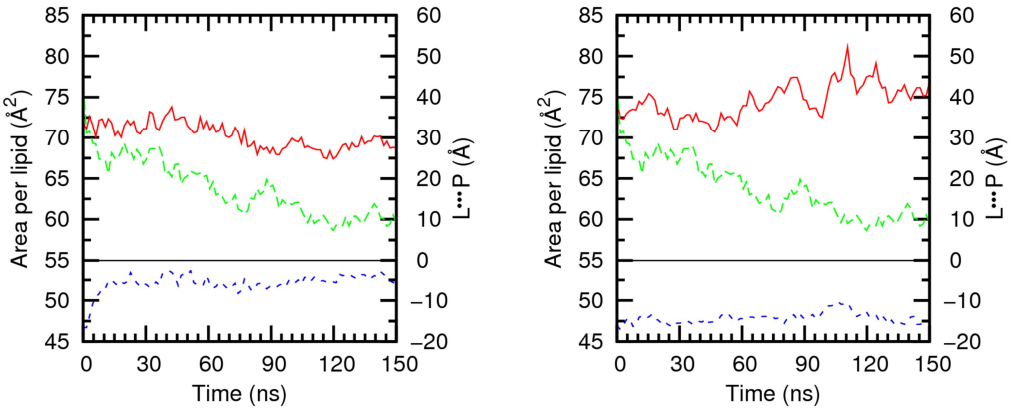

Figure 67 – Evolution of the area per lipid through the MD simulations carried out for the systems F (left, red line) and G (right, red line). Both are compared with evolution of area per lipid in system E (green line). Also represented, is the evolution of the L•••P distance (blue line) in each system. Data was smoothed with Bézier curves.

The area per lipid in simulations of the systems H and I seems to be slightly affected by the internalization of L^{26} and L^{8} in the bilayer of each system, when their simulations are compared with evolution of area per lipid in system E, as shown in Figure 68. After insertion of L^{26}, and during the last 100 ns of simulation time, when the system was equilibrated, the average area per lipid was 68.88 ± 1.85 Å^2, and, as found for system F, is *ca.* 9 Å^2 away from the average value for system E. Regarding area per lipid of system I, during the equilibrated period of the system, for the last 50 ns, the average area per lipid, 65.77 ± 0.79 Å^2, is deviated by about 6 Å^2 from the average value of system E. Again, this comparison indicates the imperative necessity of the additional replica data for all overhydrated systems.

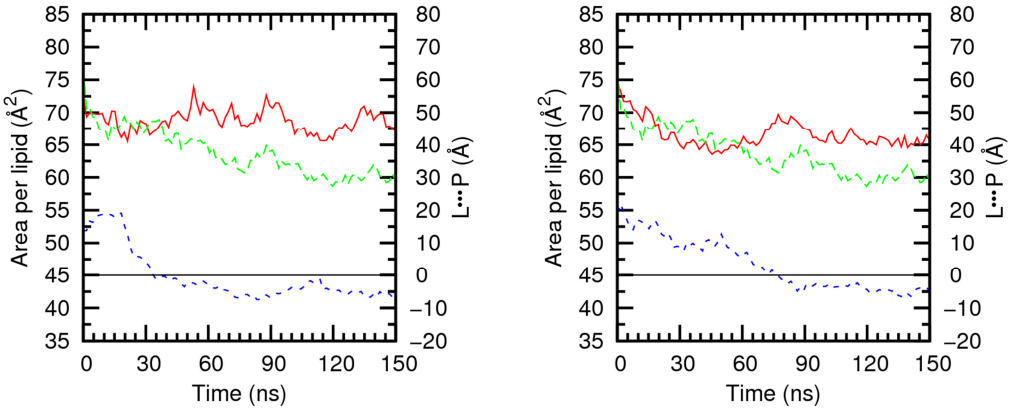

Figure 68 – Evolution of the area per lipid through the MD simulations carried out for the systems H (left, red line) and I (right, red line). Both are compared with evolution of area per lipid in system E (green line). Remaining details as given in Figure 67.

Volume per lipid

Volume per lipid, as seen in the pure membrane systems A and E, with average volumes of 1248.9 ± 23.8 $Å^3$ and 1225.3 ± 6.8 $Å^3$, respectively, are below the 1256 $Å^3$ experimental reference at 303 K. Despite the difference presented in the area per lipid above, the average volume per lipid of system F is close to the values assessed in system E, with an average volume per lipid of 1227.4 ± 10.4 $Å^3$, estimated for the last 100 ns of the MD simulation. On the other hand, as can be seen in the right plot of Figure 69, and considering the greater difference found in the area per lipid in the MD simulation G, it is worth to note that during the last 50 ns of simulation time, where the system was considered equilibrated, the average volume per lipid in this simulation is 1241.8 ± 7.1 $Å^3$, a value that is slightly above the average volume per lipid found for system E, and that certainly depends on the perturbation caused by $L^8 \subset Cl^-$ inside the bilayer. Also, of note, is that the early movement of the chloride association $L^{26} \subset Cl^-$ inside the bilayer in simulation F seems to have caused no relevant changes in the lipid volume evolution, as suggested by the curves of F and E systems, which present almost the same behavior during the initial 40 ns of both simulations (see Figure 69, left).

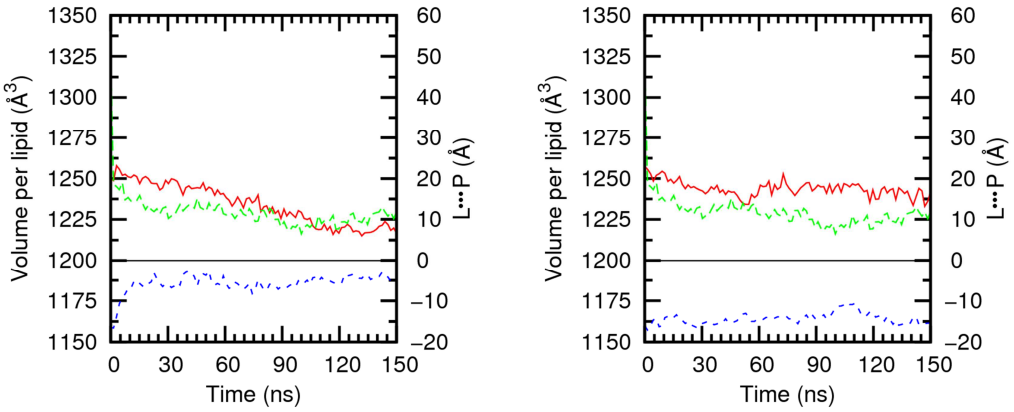

Figure 69 – Evolution of the volume per lipid through the MD simulations carried out for the systems F (left, red line) and G (right, red line). Both are compared with evolution of volume per lipid in system E (green line). Remaining details as given in Figure 67.

The analysis of the internalization of L^{26} and L^8 into the bilayer, using as starting geometry the receptor placed in the water slab (systems H and I), indicates that those events present no relevant effect on volume per lipid, as seen in Figure 70. In fact, the average volume per lipid in system H after internalization of L^{26} is 1239.4 ± 9.9 $Å^3$ (last 100 ns), while for system I, for the last 50 ns, the volume per lipid average is 1238.7 ± 6.6 $Å^3$. For both systems, the average area per lipid after internalization of either L^{26} or L^8 is slightly above the average for system E, 1227.4 ± 10.4 $Å^3$, but not considered to be substantially affected.

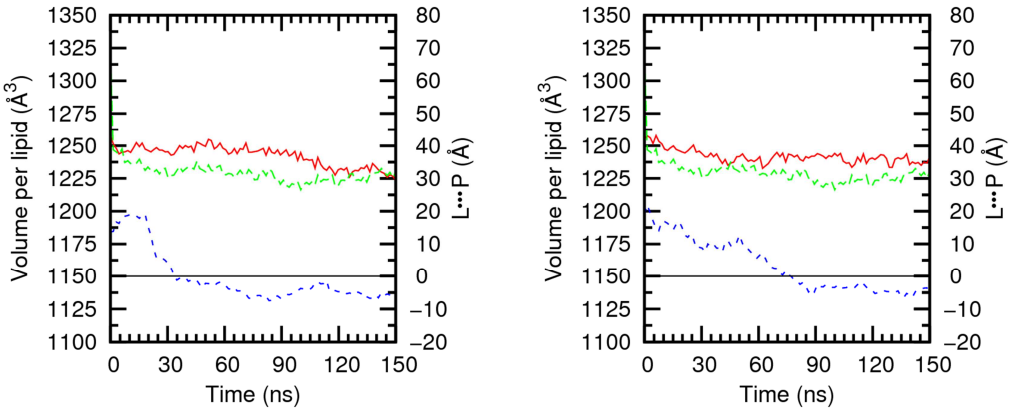

Figure 70 – Evolution of the volume per lipid through the MD simulations carried out for the systems H (left, red line) and I (right, red line). Both are compared with evolution of volume per lipid in system E (green line). Remaining details as given in Figure 67.

Bilayer thickness

Following the analysis above for area per lipid evolution of the systems F to I, the bilayer thickness estimated for these systems from the corresponding MD simulation data is expected to be lower than in system E. Such prediction is corroborated by Figure 71, for the systems F and G, containing L^{26} and L^{8}, respectively. The bilayer thickness given by the average distance between the phospholipid head groups during the last 100 ns of the MD simulation of system F is 34.7 ± 0.5 Å, which is 4.8 Å lower than the 39.5 ± 0.5 Å average of system E. The bilayer thickness assessed during the last 50 ns of simulation of system G, with an average value of 32.4 ± 0.5 Å, as expected, is lower than the average bilayer thickness of the systems E and F. Therefore, the bilayer thickness of system F seems to undergo little interference from the presence of L^{26}, whilst the changes caused by the association $L^{8}\subset Cl^{-}$ are meaningful and, as previously stated, have caused more pronounced changes in the structural properties of the bilayer.

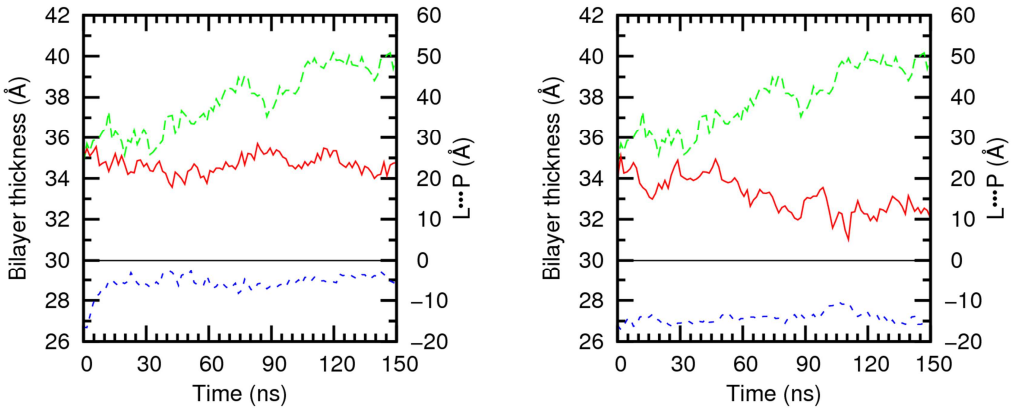

Figure 71 – Evolution of the bilayer thickness through the MD simulations carried out for the systems F (left, red line) and G (right, red line). Both are compared with evolution of bilayer thickness in system E (green line). Remaining details as given in Figure 67.

Similar to area per lipid, bilayer thickness also experiences little effect from the penetration of either receptor through the water/lipid interface, as can be observed in the left (system H) and right plot (system I) of Figure 72. For the last 100 ns of the simulation of system H, where the system is equilibrated, the average bilayer thickness is 35.4 ± 0.7 Å, below the average value for system E. Also below the average of system E, is the average bilayer thickness for the last 50 ns of simulation of system I, 36.8 ± 0.4 Å, although closer to the bilayer thickness of 39.5 ± 0.5 Å, observed in system E.

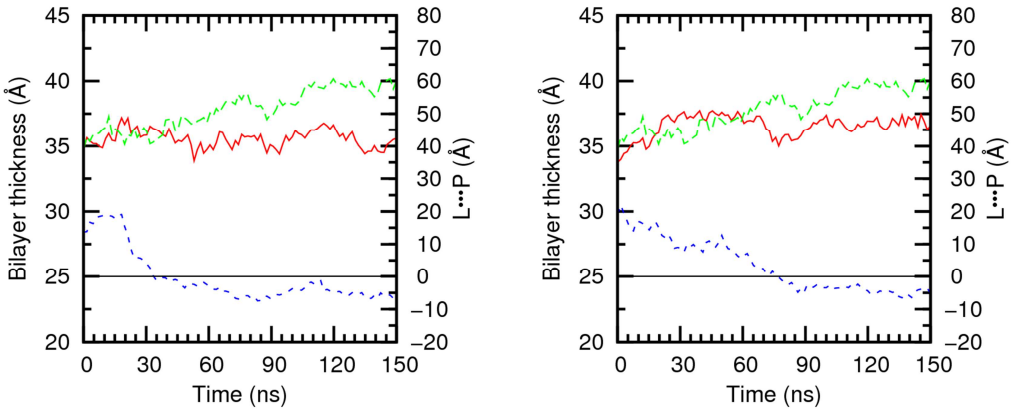

Figure 72 – Evolution of the bilayer thickness through the MD simulations carried out for the systems H (left, red line) and I (right, red line). Both are compared with evolution of bilayer thickness in system E (green line). Remaining details as given in Figure 67.

Electron density profile

As stated in the analysis of the fully hydrated POPC pure membranes, the electron density profiling of each system allows the determination of the individual positions occupied by the different species of the system, during the period of analysis, with proper highlight to receptors L^{26} and L^{8}. The electron density of the systems F and G are plotted, along with the individual profiles for water, phospholipids, phosphorus atoms, L^{26} or $L^{8}\subset Cl^{-}$ in Figure 73.

The bilayer thickness estimated from the distance between the peaks of the electron density profile of the system (red lines in Figure 73) is 36.5 Å for system F and 32.7 Å for system G, while the bilayer thickness calculated by the average distance between the phosphorus atoms is 34.7 ± 0.5 and 32.4 ± 0.5 Å, respectively. Furthermore the first two measured distances are shorter the than the distance for system E, 37.7 Å, which is evident when the profiles of these three systems are compared for the last 10 ns of the MD simulation, as can be seen in Figure 73. The profile of system F shows an elevation at the core of the bilayer, consistent with observations on thinner bilayer thicknesses assessed in the systems A to D (see *Electron density profile*, in *Fully Hydrated free membrane simulation*). Despite the thinner thickness presented by system G, this elevation is not shown. However, as seen in the right panel of Figure 73, the chloride association $L^{8}\subset Cl^{-}$, represented by the cyan line, is preferentiality located near the core of the phospholipid bilayer and might be the cause for this perturbation. In contrast, L^{26} in system F, shows an electron density profile with a single peak at z=-12.4 Å (*i.e.*, 12.4 Å away from the bilayer core) indicating the position of this receptor, close to and below the lipid head groups, as illustrated with the snapshot presented in Figure 51. Indeed, the electron density profile defined by the phosphorus atoms positions, has two peaks centred at z=±18.2 Å, with the peak at z=-18.2 Å at 5.8 Å distance from the L^{26} one, being this, distance consistent with the 5.4 ± 1.3 Å average L•••P distance during the last 100 ns of the MD simulation of system F. In system G, the chloride association $L^{8}\subset Cl^{-}$ has its peak at z=-0.9 Å, *i.e.*, 15.5 Å away from the closest phosphorus peak (z=-16.4 Å), which is in good agreement with the average L•••P distance assessed for the last 50 ns of simulation of system G, 14.3 ± 1.4 Å.

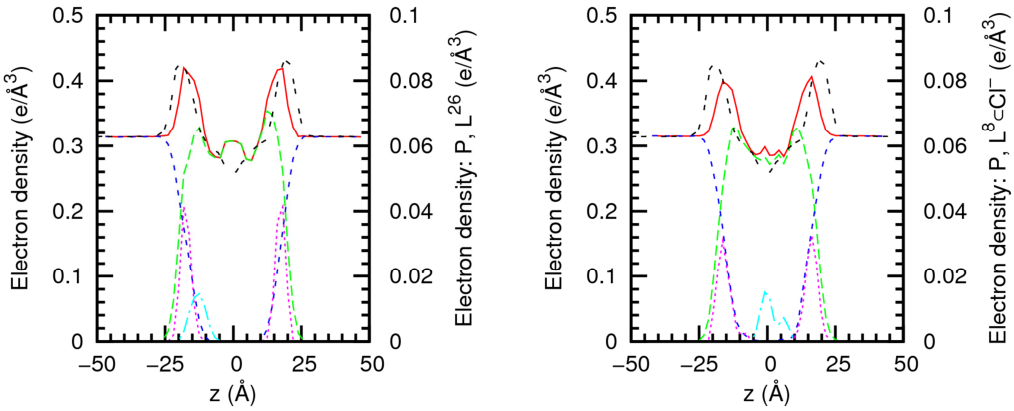

Figure 73 – Electron density profiles for the systems F (left) and G (right), calculated for the last 10 ns of simulation time, with the system profile in red, lipids in green, water in blue, phosphorus atoms in magenta, and L^{26} and $L^8 \subset Cl^-$ in cyan. The electron density profile of system E (black line) is also included in both plots for comparison purposes.

The electron density profiles for the systems H and I are depicted in Figure 74 for the last 10 ns of simulation time. The density profile of both systems exhibits two peaks separated by 35.4 Å for H and 35.3 Å for I. These distances agree well with the bilayer thickness of 35.4 ± 0.7 and 36.8 ± 0.4 Å mentioned above for the systems H and I respectively, but shorter than the distance of 37.7 Å found for system E, as shown by the comparison of the electron density of these three systems presented in left and right plots of Figure 74. The profiles of both systems also show a small elevation at the core of the bilayer, consistent with observations previously done for the systems A to D and F.

Figure 74 reveals that during the last 10 ns of simulation of system H, L^{26} was constantly close to the phosphorus atoms, as illustrated in the snapshot presented in Figure 57. The L^{26} electron density profile has a single peak at z=-14.7 Å, which is 1.8 Å away from the closest peak at z=-16.5 Å, exhibited by the phosphorus atoms electron density profile This distance is substantially shorter than the 4.7 ± 1.6 Å average L•••P distance found between the mass centre of L^{26} (see *Bilayer thickness*, above) and the positions successively occupied by the phosphorous atoms through the last 100 ns simulation of system H. The electron density profile of L^8 in system I, with the peak of L^8 at z=15.1 Å, indicates that the receptor is near to the phosphorus atoms, considering that these polar groups have an electron density profile with two peaks at z=±19.2 Å. Indeed, the peak for L^8 is separated of the closest phosphorus peak by 4.1 Å, which is in excellent agreement with the average 4.3 ± 1.1 Å L•••P distance between L^8 and the closest interface during the last 50 ns of simulation of system I.

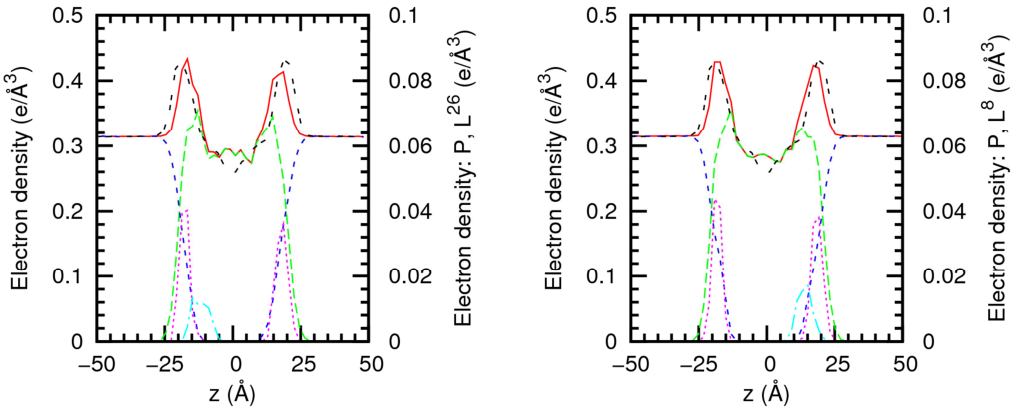

Figure 74 – Electron density profiles for the systems H (left) and I (right), calculated for the last 10 ns of simulation time, with L^{26} and L^8 profiles in cyan. Remaining details as given in Figure 73.

Chain order

The deuterium order parameters of each chain of the POPC lipids are expected to be perturbed during the last 5 ns of simulation time by the presence of L^{26} in the systems F and H, $L^8 \subset Cl^-$ in system G and L^8 in system I. The proper assessment of this variation would consist on the evaluation of chains closer (at a stipulated radius) to each receptor within the bilayer with comparison to the remaining chains of the system, to understand the effect caused on order parameters. Due to technical limitations, such evaluation was not possible, so the whole bilayer was analysed and compared to the reference system E.

Recalling the experimental results closely reproduced in the MD simulation of system E, order parameters on both *sn*-1 and *sn*-2 chains (see Scheme 12, above) have higher $|S_{CD}|$ values closer to the interface, and these values decrease on atoms with a higher index, *i.e.*, deeper in the bilayer. Thus, for the systems F and G, the analysis of both plots on Figure 75 is rather simplified, as the order parameters for both chains do not reproduce that feature, along with the mismatch of $|S_{CD}|$ values for the carbon atoms in the double bond of the *sn*-2 chain. Furthermore, it would be expected that on system F, as L^{26} is closer to the interface, the major difference in both chains, if existent, would be present in the initial carbon atoms of either chain. Nonetheless, as can be seen in the left plot of Figure 75, that assumption is only verified for the *sn*-2 chain, with lower $|S_{CD}|$ values registered in the initial atoms of the chain, when compared to the results from system E. For the *sn*-1 chain, the major difference is found towards the terminal carbon atoms of the chain, with higher values of $|S_{CD}|$. Regarding system G, where the chloride association $L^8 \subset Cl^-$ remained at the core of the bilayer and, thus, near the middle and terminal atoms of either chain, it is noteworthy that, as seen on the right view of Figure 75, for both chains in atoms C12 and beyond, the $|S_{CD}|$ values are overlapped. The

reason for this occurrence might be explained by one of the following possibilities: the presence of $L^8 \subset Cl^-$ has no effects on the terminal ends of either chain (*sn*-1 or *sn*-2); or the effect of $L^8 \subset Cl^-$ on closer chains is diluted in the $|S_{CD}|$ values obtained for the whole system. These hypotheses will be further investigated when new replicas are completed.

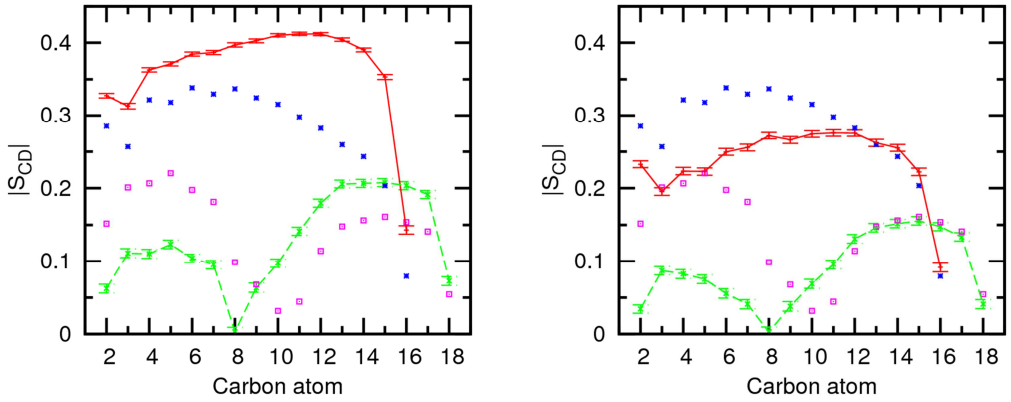

Figure 75 – Computed $|S_{CD}|$ for palmitoyl *sn*-1 and oleyl *sn*-2 during the 5 last ns of the MD simulation of the systems F (left) and G (right), and compared with results from MD simulation of system E, as a function of the carbon atom index. $|S_{CD}|$ values for *sn*-1 and *sn*-2 chains of the systems F and G are represented by the red and green lines, respectively, with associated standard error represented by the error bars. $|S_{CD}|$ values for *sn*-1 and *sn*-2 chains of system E are represented by the blue filled and magenta empty squares, respectively.

Following the assessment above, the analysis of both plots on Figure 76 is also abbreviated, as the computed order parameters for both chains fail to perfectly reproduce the behaviour of the *sn*-1 chain of system E, despite the closer match presented by $|S_{CD}|$ values for the double bond atoms in the *sn*-2 chain. In the systems H and I, as both receptors are closer to the interface, the major difference from the order parameters for both chains, if existent, would be present at the initial carbon atoms of either chain. Indeed, as seen in the left plot of Figure 76, for system H, this assumption is verified for the initial carbon atoms of *sn*-2 chain, with higher $|S_{CD}|$ values registered when compared to the results from system E. In system H, for the *sn*-1 chain, the major differences are found near the terminal atoms of that lipid chain, with higher values of $|S_{CD}|$. Regarding system I, represented in the right plot of Figure 76, the values computed for the $|S_{CD}|$ of the *sn*-2 chain are closer to the values assessed for system E, while the values for the *sn*-1 chain present slight differences in the initial carbons, from C2 to C9.

From this analysis, it is observed that the presence of L^{26} or L^8 does influence this biophysical parameter of the bilayer when the receptor is initially found within the bilayer; on the other

hand, a permeating receptor seems to have a smaller effect, as shown in the comparison of the systems H and I with the system E, depicted in Figure 76.

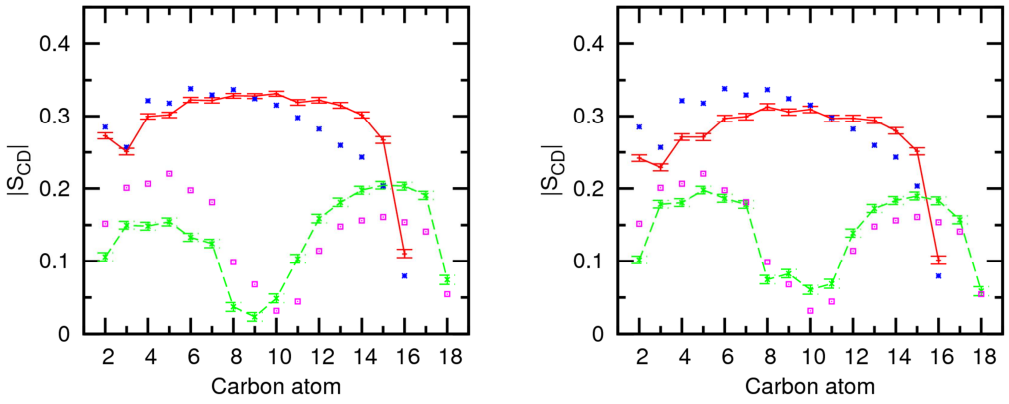

Figure 76 – Computed $|S_{CD}|$ for palmitoyl *sn*-1 and oleyl *sn*-2 during the 5 last ns of the MD simulation of the systems H (left) and I (right), and compared with results from MD simulation of system E, as a function of the carbon atom index. Remaining details as given in Figure 75.

Lateral diffusion

The lateral diffusion of the lipid head groups is not expected to change when the receptors are inside the bilayer, thus exerting little effect on these groups. Like before, the diffusion of the lipid head groups was also assessed in the systems F to I during the last 10 ns of simulation time. As can be seen in the left plots of Figure 77 and Figure 78, two distinct diffusion domains are present for all systems. The MSD curve of the lipid head groups was fitted in the same time windows as above (see the right plots of both Figures), showing that, for each simulation system, the diffusion coefficient D_{lat} converged between 3 and 4 ns for both simulations, thus defining the long time domain between 4 and 10 ns.

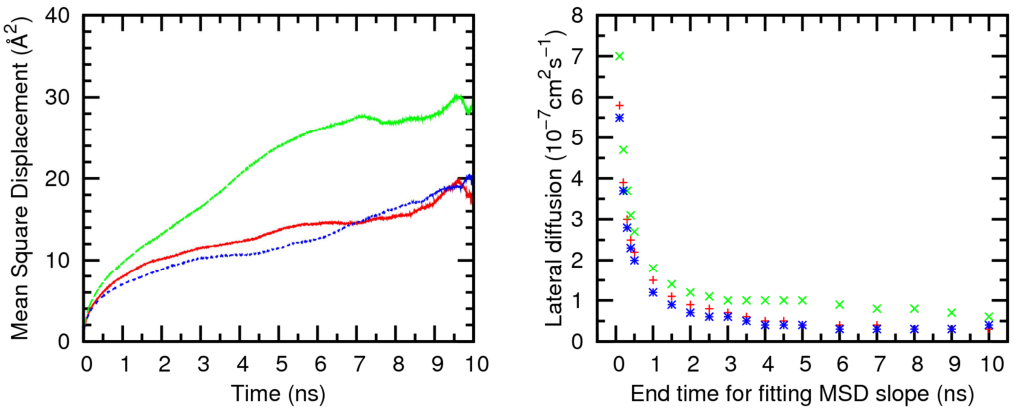

Figure 77 – Lipid diffusion coefficients calculated for the last 10 ns, using MD simulation data of the systems F, G and E (left plot) and MSD values calculated using different time windows (right plot). In both plots, red, green and blue colours stand for the systems F, G and E.

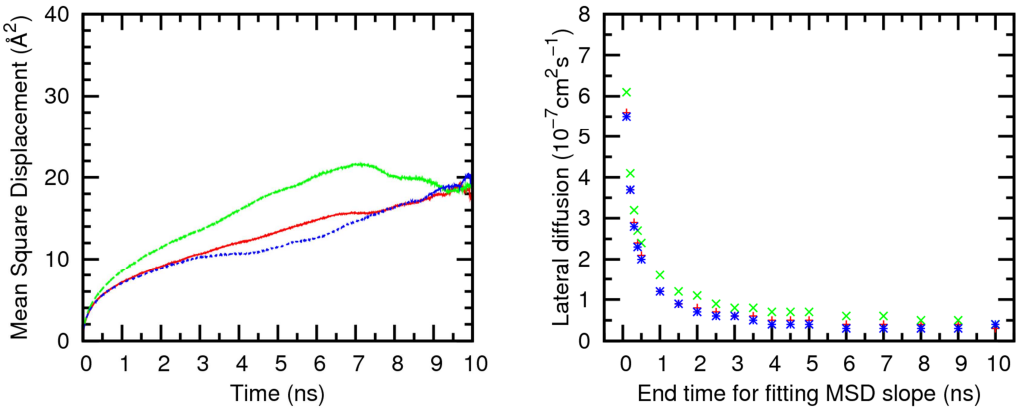

Figure 78 – Lipid diffusion coefficients calculated for the last 10 ns, using MD simulation data of the systems H, I and E (left plot) and MSD values calculated using different time windows (right plot). In both plots, red, green and blue colours stand for the systems H, I and E.

The diffusion coefficient D_{lat} for the short time domain in system F, during the first 4 ns, is 0.5 × 10^{-7} cm^2s^{-1}, while in system G it is 1.0 × 10^{-7} cm^2s^{-1}. This coefficient is 0.5 × 10^{-7}, and 0.7 × 10^{-7} cm^2s^{-1}, for the short time domain of the systems H and I, in this order. The results for the systems F, H and I are close to the D_{lat} diffusion coefficient of system E (0.4 × 10^{-7} cm^2s^{-1}), while in system G the D_{lat} coefficient is above the value assessed for system E. Despite the initial assumption, on the long time domain systems F and G present diffusion coefficients D_{lat} of 0.2 and 0.4 × 10^{-7} cm^2s^{-1}, respectively, while system H has a diffusion coefficient D_{lat} of 0.3 × 10^{-7} cm^2s^{-1}, and system I presents a diffusion coefficient D_{lat} of 0.1 × 10^{-7} cm^2s^{-1}. These values are generally below the 0.4 × 10^{-7} cm^2s^{-1} of simulation E, especially on system I.

These results shed some light on the influence of L^{26} and L^{8} in this dynamic parameter, demonstrating that the internalized receptors, beneath the lipid head groups, change the D_{lat} coefficient of the several systems.

Hydration of the water/lipid interface

The assessment of the water molecules near the head groups of the POPC lipid in the systems F to I yields results consistent with the data from system E. The MD simulation data of system E shows that, on average, 11.0 ± 0.2 water molecules are solvating the lipid head groups (within a 3.5 Å radius). Concerning systems F to I, an average of 11.7 ± 0.2 water molecules was found for system F, 12.4 ± 0.2 water molecules were found near the head groups of system G, and an average of 11.8 ± 0.2 and 11.7 ± 0.2 water molecules were found within a 3.5 Å radius of the head groups in systems H and I, respectively. Furthermore, the structure of water molecules assembly around the phospholipid head groups for the systems F to I is similar to the one of system E, as evident from the RDF for these systems, shown in Figure 79, which are nearly superimposable, with small differences only in the third solvation shell, at about 8.5 Å.

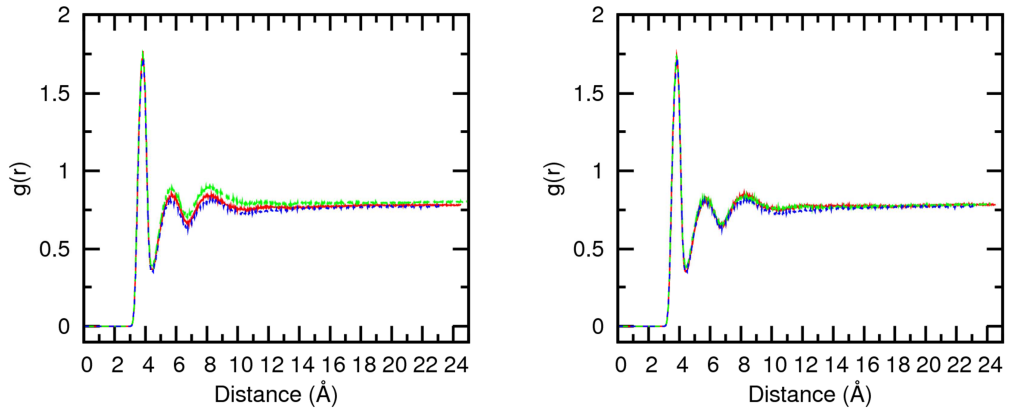

Figure 79 – P-O RDF of water molecules around the head groups in the MD simulations of the systems E to G for the last 1 ns of simulation time. In the left plot, the systems F, G and E are represented as red, green and blue lines respectively, while in the right plot, the red, green and blue lines correspond to the systems H, I and E, in this order.

Summing Up

Although only a single replica was available for analysis during the time available for the conclusion of this thesis, and despite the restrictions drawn from that limitation, some preliminary conclusions are possible to be drawn. A comparison between the biophysical membrane parameters estimated from MD simulation data of the systems F to I, with the different starting geometries, and system E is presented in Table 32.

Table 32 – Comparison between the structural parameters for the phospholipid bilayer systems F to I and E.

Parameter	*System*				
	F	G	H	I	E
L•••P (Å)[a]	5.4 ± 1.3	14.3 ± 1.4	4.7 ± 1.6	4.3 ± 1.1	--
Area per lipid (Å^2)[b]	69.50 ± 1.25	76.47 ± 1.58	68.88 ± 1.85	65.77 ± 0.79	60.18 ± 0.96
Volume per lipid (Å^3)[b]	1227.4 ± 10.4	1241.8 ± 7.1	1239.4 ± 9.9	1238.7 ± 6. 6	1225.3 ± 6.8
Bilayer thickness (Å)[b]	34.7 ± 0.5	32.4 ± 0.5	35.4 ± 0.7	36.8 ± 0.4	39.5 ± 0.5
Head group hydration[b]	11.7 ± 0.2	12.4 ± 0.2	11.8 ± 0.2	11.7 ± 0.2	11.0 ± 0.2

[a] 100 ns of sampling time for the systems F and H, 150 ns for system G and 100 ns for system I.
[b] 100 ns of sampling in the systems F and H and 50 ns in the systems G, I and E.

The data available indicates that the presence of L^{26} or L^{8} in the systems F, H and I has marginal effects on the membrane structural properties evaluated, while in system G, where $L^{8}\subset Cl^{-}$ has remained at the core of the bilayer, these properties seem to have endured a greater effect.

The analysis of the binding behaviour of the chloride associations inside the phospholipid bilayers in the systems F and G has shown that L^{26} has migrated to the water/lipid interface and quickly released the chloride, while L^{8} has remained in the middle of the phospholipid bilayer, associated with chloride. In both cases, while the association was preserved, the chloride was hydrogen bonded to the receptor, consistently with results previously obtained in the MD simulations performed in DMSO/water solution.

For the systems H and I, where both associations were placed in the water slab, the chloride was promptly released to the water medium, in agreement with previous results of the MD simulations in water solution. Albeit it took different time lengths, both L^{26} and L^{8} have reached the phospholipid bilayer and breached through the water/lipid interface, nesting between the lipids, below to the lipid head groups, as L^{26} has done in the MD simulation of system F.

As mentioned above, at least two replica MD simulations are being run for all the four systems, in search of further insights and corroboration of the preliminary data here presented. However, it is now safe to state that the outlined MD simulations are adequate to fulfill the objectives outlined in the beginning of this section.

4 Conclusions

As previously stated by Davis *et al.*, 2010, to develop synthetic molecules for the anion transmembrane transport, a fine balance must be achieved regarding the synthetic effort, the ion selectivity, and the transport activity.(8) In this context, the molecular dynamics simulations performed in DMSO/water solution and in pure water, indicate that both L^{26} and L^{8} have transport ability potential. Indeed, when in DMSO/water solution, the chloride association with each receptor is retained with resort to hydrogen bonds between each species. On the other hand, when the associations $L^{26}\subset Cl^-$ and $L^{8}\subset Cl^-$ were solvated in water, the anion was promptly released from each receptor and solvated by the surrounding water molecules.

Before placing each chloride association in a membrane system, extensive testing was performed to select the simulation conditions that produced the results with better consistency with the experimental data available. The evaluation of several structural (area and volume per lipid, bilayer thickness, electron density profile, chain order and lipid head group hydration) and dynamic (lateral lipid head group diffusion) parameters led to the election of the SPC/E water model to hydrate the bilayer system and the selection of the unconstrained RESP atomic charges for the characterization of the POPC lipids. These conditions were obtained from the simulations carried out with a fully hydrated phospholipid bilayer and further employed in the simulation of a large overhydrated membrane system, which is characterised by an excess of water molecules, to accommodate $L^{26}\subset Cl^-$ and $L^{8}\subset Cl^-$. The simulation of this larger system demonstrated that the increased number of waters had no substantial effect on the evaluated structural and dynamic properties.

Finally, when the chloride associations were included in an overhydrated system, two different starting geometries for each association were generated, placing the associations within the phospholipid bilayer or in the water slab of the system. As for these four systems only a single replica simulation was carried out, all results must be carefully taken into account, requiring further confirmation. The preliminary data demonstrate that L^{26} and L^{8} have the ability to diffuse from the water slab and permeate the water/lipid interface of the phospholipid bilayer, as well as the ability to move from the middle of the bilayer to the water/lipid interface and release the associated chloride anion.

In three of the four studied systems, the receptors diffused and positioned themselves near the lipid head groups, inside the phospholipid bilayer. Some biophysical parameters of the bilayer were perturbed by the presence of the receptors, differing slightly from the estimated values for the pure overhydrated system. In the system where $L^8 \subset Cl^-$ was placed inside the phospholipid bilayer, the association remained near the starting position and the chloride was kept associated to the receptor during the entire simulation time. This led to great perturbations in the area per lipid and bilayer thickness in the system. In spite of only a single replica simulation was concluded for each of the overhydrated systems, the membrane simulations here reported, totalling 2.55 μs of simulation time, took nearly 4400 hours of CPU time, *i.e.*, 183 days of continuous simulation time.

The results presented, although in need of confirmation by further replica MD simulations, indicate that the L^{26} and L^8 have little impact on biophysical parameters of the phospholipid bilayer model studied, suggesting the ability of these receptors to promote the chloride transmembranar transport in agreement with experimental studies. Moreover, the employed methodology can be extended to other anion associations with structurally related receptors, thus enabling a comprehensive research of potential therapeutic alternatives for channelopathies such as cystic fibrosis.

5 Future Work

Following the work previously described, further MD investigations will be performed, to bring more insights in the chloride transport mediated by tripodal receptors. In addition, following the recent work of Gale *et al.*,(152) theoretical studies will be extended to other related receptors, as summarized below:

- Study of the binding ability of L^{26}, L^{8} and fluorinated tripodal receptors towards other biologically relevant anions (such as sulfate, phosphate, nitrate and bicarbonate);
- Study of clustering effects of two or more receptors in solution (pure water or DMSO/water solution) and in phospholipid bilayer models;
- Further insights in the chloride anion transport mediated by synthetic receptors will be investigated, using a bilamellar membrane system composed of two adjacent phospholipid bilayers;
- Investigation of a wide range of tripodal based receptors in other membrane models composed of other lipids (*e.g.*, DPPC, DMPC, POPE) or in phospholipid bilayers incorporating cholesterol.

The future work will be carried out using the GAFF force field for the receptors and phospholipids. Alternatively, the lipid molecules will be described using a force field compatible with the use of GAFF and not requiring the imposition of surface tension. This approach will be possible with the new release of the AMBER software suite, available in a near future, and enabling the full use of the twelve Nvidia Graphics Processing Units available at the Molecular Modeling Group.

6 References

1. Alberts B, Johnson A, Lewis J, Raff M, Roberts K, Walter P. Molecular Biology of the Cell. 4th ed: Garland Science; 2002.

2. Lodish H, Berk A, Matsudaira P, Kaiser CA, Krieger M, Scott MP, et al. Molecular Cell Biology. 5th ed: W. H. Freeman; 2003.

3. Rhoades RA, Tanner GA. Medical Physiology. 2nd ed: Lippincott Williams & Wilkins; 2003.

4. Barrett KE, Barman SM, Boitano S, Brooks H. Ganong's Review of Medical Physiology. 23rd ed: McGraw-Hill Medical; 2009.

5. Par-Plan. In: Licker MD, editor. Encyclopedia of Science and Technology. 10th ed. New York: McGraw-Hill; 2007. p. 375.

6. Karp G. Cell and Molecular Biology: Concepts and Experiments. 6th ed: Wiley; 2009.

7. Boron WF, Boulpaep EL. Medical Physiology - Updated Edition. Updated ed: Saunders; 2004.

8. Davis JT, Okunola O, Quesada R. Recent advances in the transmembrane transport of anions. Chem Soc Rev. 2010 Oct;39(10):3843-62.

9. Ashcroft FM. Ion Channels and Disease. 1st ed: Academic Press; 1999.

10. Planells-Cases R, Jentsch TJ. Chloride channelopathies. Biochim Biophys Acta. 2009 Mar;1792(3):173-89.

11. Cannon SC. Physiologic principles underlying ion channelopathies. Neurotherapeutics. 2007 Apr;4(2):174-83.

12. Hoffman EP, Lehmann-Horn F, Rudel R. Overexcited or inactive: ion channels in muscle disease. Cell. 1995 Mar 10;80(5):681-6.

13. Bernard G, Shevell MI. Channelopathies: a review. Pediatr Neurol. 2008 Feb;38(2):73-85.

14. Lehmann-Horn F, Jurkat-Rott K, Begley TP. Ion Channels in Medicine. Wiley Encyclopedia of Chemical Biology: John Wiley & Sons, Inc.; 2007.

15. Davis AP, Sheppard DN, Smith BD. Development of synthetic membrane transporters for anions. Chem Soc Rev. 2007;36(2):348-57.

16. Antonisse MMG, Reinhoudt DN. Neutral anion receptors: design and application. Chem Comm. 1998 Feb 21(4):443-8.

17. Gale PA. Anion receptor chemistry. Chem Comm. 2011;47(1):82-6.

18. McNaught AD, Wilkinson A. IUPAC. Compendium of Chemical Terminology. 2nd ed. Oxford: Blackwell Scientific Publications; 1997.

19. Ionophores - MeSH Result. Bethesda1960 [November 24th, 2010]; Available from: http://www.ncbi.nlm.nih.gov/sites/entrez?Db=mesh&Cmd=ShowDetailView&TermToSearch=68007476&ordinalpos=1&itool=EntrezSystem2.PEntrez.Mesh.Mesh_ResultsPanel.Mesh_RVDocSum.

20. I-Lev. In: Licker MD, editor. Encyclopedia of Science and Technology. 10th ed. New York: McGraw-Hill; 2007. p. 445-7.

21. Fyles TM. Synthetic ion channels in bilayer membranes. Chem Soc Rev. 2007 Feb;36(2):335-47.

22. Jeong EJ, Kang EJ, Sung LT, Hong SK, Lee E. Stereoselective synthesis of pamamycin-607. J Am Chem Soc. 2002 Dec 11;124(49):14655-62.

23. Sheth TR, Henderson RM, Hladky SB, Cuthbert AW. Ion channel formation by duramycin. Biochim Biophys Acta. [Research Support, Non-U.S. Gov't]. 1992 Jun 11;1107(1):179-85.

24. Ohkuma S, Sato T, Okamoto M, Matsuya H, Arai K, Kataoka T, et al. Prodigiosins uncouple lysosomal vacuolar-type ATPase through promotion of H+/Cl- symport. Biochem J. 1998 Sep 15;334:731-41.

25. Davis JT, Gale PA, Okunola OA, Prados P, Iglesias-Sanchez JC, Torroba T, et al. Using small molecules to facilitate exchange of bicarbonate and chloride anions across liposomal membranes. Nat Chem. 2009 May;1(2):138-44.

26. Cook GA, Prakash O, Zhang K, Shank LP, Takeguchi WA, Robbins A, et al. Activity and structural comparisons of solution associating and monomeric channel-forming peptides derived from the glycine receptor m2 segment. Biophys J. 2004 Mar;86(3):1424-35.

27. McNally BA, O'Neil EJ, Nguyen A, Smith BD. Membrane Transporters for Anions That Use a Relay Mechanism. J Am Chem Soc. 2008;130(51):17274-5.

28. Atkinson AJ, Abernethy DR, Daniels CE, Dedrick R, Markey SP. Principles of Clinical Pharmacology. 2nd ed: Academic Press; 2007.

29. McNally BA, Koulov AV, Lambert TN, Smith BD, Joos JB, Sisson AL, et al. Structure-Activity Relationships in Cholapod Anion Carriers: Enhanced Transmembrane Chloride Transport through Substituent Tuning. Chem Eur J. 2008;14(31):9599-606.

30. Pedersen CJ. Cyclic polyethers and their complexes with metal salts. J Am Chem Soc. 1967;89(26):7017-36.

31. Park CH, Simmons HE. Macrobicyclic Amines .3. Encapsulation of Halide Ions by in,in-1,(K+2)-Diazabicyclo[K.L.M]Alkane-Ammonium Ions. J Am Chem Soc. 1968;90(9):2431-&.

32. Cresp TM, Probert CL, Sondheimer F. An approach to the synthesis of ionophores related to A23187. Tetrahedron Letters. 1978;19(41):4.

33. Evans D, Sacks C, Whitney R. Studies directed towards the total synthesis of the ionophore antibiotic A-23187. Tetrahedron Letters. 1978(8):8.

34. Tabushi I, Kuroda Y, Yokota K. A,B,D,F-tetrasubstituted [beta]-cyclodextrin as artificial channel compound. Tetrahedron Letters. 1982;23(44):4601-4.

35. van Beijnen AJM, Nolte RJM, Zwikker JW, Drenth W. A molecular cation channel. Rec des Trav Chim des Pays-Bas. 1982;101(11):409-10.

36. Doyle DA, Morais Cabral J, Pfuetzner RA, Kuo A, Gulbis JM, Cohen SL, et al. The structure of the potassium channel: molecular basis of K+ conduction and selectivity. Science. 1998 Apr 3;280(5360):69-77.

37. Gouaux E, Mackinnon R. Principles of selective ion transport in channels and pumps. Science. 2005 Dec 2;310(5753):1461-5.

38. Gale PA. Anion receptor chemistry: highlights from 1999. Coord Chem Rev. 2001 Mar;213:79-128.

39. Gale PA. Anion and ion-pair receptor chemistry: highlights from 2000 and 2001. Coord Chem Rev. 2003 May;240(1-2):191-221.

40. Gale PA, Quesada R. Anion coordination and anion-templated assembly: Highlights from 2002 to 2004. Coord Chem Rev. 2006 Dec;250(23-24):3219-44.

41. Gale PA, Garcia-Garrido SE, Garric J. Anion receptors based on organic frameworks: highlights from 2005 and 2006. Chem Soc Rev. 2008;37(1):151-90.

42. Caltagirone C, Gale PA. Anion receptor chemistry: highlights from 2007. Chem Soc Rev. 2009;38(2):520-63.

43. Gale PA. Anion receptor chemistry: highlights from 2008 and 2009. Chem Soc Rev. 2010;39(10):3746-71.

44. Brotherhood PR, Davis AP. Steroid-based anion receptors and transporters. Chem Soc Rev. 2010 Oct;39(10):3633-47.

45. Kang SO, Llinares JM, Day VW, Bowman-James K. Cryptand-like anion receptors. Chem Soc Rev. 2010 Oct;39(10):3980-4003.

46. Matile S, Vargas Jentzsch A, Montenegro J, Fin A. Recent synthetic transport systems. Chem Soc Rev. 2011 Mar 9.

47. Gokel GW, Carasel IA. Biologically active, synthetic ion transporters. Chem Soc Rev. 2007;36(2):378-89.

48. McNally BA, Leevy WM, Smith BD. Recent Advances in Synthetic Membrane Transporters. Supramol Chem. 2007 Jan;19(1-2):29-37.

49. Schlesinger PH, Ferdani R, Pajewski R, Pajewska J, Gokel GW. A hydrocarbon anchored peptide that forms a chloride- selective channel in liposomes. Chem Comm. 2002(8):840-1.

50. Ferdani R, Pajewski R, Djedovic N, Pajewska J, Schlesinger PH, Gokel GW. Anion transport in liposomes responds to variations in the anchor chains and the fourth amino acid of heptapeptide ion channels. New J Chem. 2005;29(5):673-80.

51. Gorteau V, Bollot G, Mareda J, Perez-Velasco A, Matile S. Rigid oligonaphthalenediimide rods as transmembrane anion-pi slides. J Am Chem Soc. 2006 Nov 22;128(46):14788-9.

52. Hennig A, Fischer L, Guichard G, Matile S. Anion−Macrodipole Interactions: Self-Assembling Oligourea/Amide Macrocycles as Anion Transporters that Respond to Membrane Polarization. J Am Chem Soc. 2009 2009/11/25;131(46):16889-95.

53. Iqbal KSJ, Cragg PJ. Transmembrane ion transport by calixarenes and their derivatives. Dalton Trans. 2007 Jan 7(1):26-32.

54. Gokel GW, Barkey N. Transport of chloride ion through phospholipid bilayers mediated by synthetic ionophores. New J Chem. 2009;33(5):947-63.

55. Matile S, Som A, Sordé N. Recent synthetic ion channels and pores. Tetrahedron. 2004;60(31):6405-35.

56. Gale PA. Anion coordination and anion-directed assembly: highlights from 1997 and 1998. Coord Chem Rev. 2000 Apr;199:181-233.

57. Valiyayeettil S, Engbersen JFJ, Verboom W, Reinhoudt DN. Synthesis and Complexation Studies of Neutral Anion Receptors. Angew Chem Int Ed Engl. 1993 Jun;32(6):900-1.

58. Allen FH. The Cambridge Structural Database: a quarter of a million crystal structures and rising. Acta Crystallogr B. 2002 Jun;58:380-8.

59. Lakshminarayanan PS, Ravikumar I, Suresh E, Ghosh P. Trapped inorganic phosphate dimer. Chem Comm. 2007(48):5214-6.

60. Ravikumar I, Lakshminarayanan PS, Arunachalam M, Suresh E, Ghosh P. Anion complexation of a pentafluorophenyl-substituted tripodal urea receptor in solution and the solid state: selectivity toward phosphate. Dalton Trans. 2009(21):4160-8.

61. Ravikumar I, Ghosh P. Efficient fixation of atmospheric CO2 as carbonate in a capsule of a neutral receptor and its release under mild conditions. Chem Comm. 2010;46(7):1082-4.

62. Wu B, Liang J, Yang J, Jia C, Yang XJ, Zhang H, et al. Sulfate ion encapsulation in caged supramolecular structures assembled by second-sphere coordination. Chem Comm. 2008 Apr 21(15):1762-4.

63. Custelcean R, Remy P, Bonnesen PV, Jiang DE, Moyer BA. Sulfate recognition by persistent crystalline capsules with rigidified hydrogen-bonding cavities. Angew Chem Int Ed Engl. [Research Support, U.S. Gov't, Non-P.H.S.]. 2008;47(10):1866-70.

64. Custelcean R, Remy P. Selective Crystallization of Urea-Functionalized Capsules with Tunable Anion-Binding Cavities. Cryst Growth Des. 2009 Apr;9(4):1985-9.

65. Zhuge F, Wu B, Liang J, Yang J, Liu Y, Jia C, et al. Full- or half-encapsulation of sulfate anion by a tris(3-pyridylurea) receptor: effect of the secondary coordination sphere. Inorg Chem. [Research Support, Non-U.S. Gov't]. 2009 Nov 2;48(21):10249-56.

66. Jose DA, Kumar DK, Ganguly B, Das A. Rugby-ball-shaped sulfate-water-sulfate adduct encapsulated in a neutral molecular receptor capsule. Inorg Chem. 2007 Jul 23;46(15):5817-9.

67. Custelcean R, Moyer BA, Hay BP. A coordinatively saturated sulfate encapsulated in a metal-organic framework functionalized with urea hydrogen-bonding groups. Chem Comm. 2005 Dec 28(48):5971-3.

68. Busschaert N, Gale PA, Haynes CJ, Light ME, Moore SJ, Tong CC, et al. Tripodal transmembrane transporters for bicarbonate. Chem Comm. 2010 Sep 14;46(34):6252-4.

69. Winstanley KJ, Allen SJ, Smith DK. Encapsulated binding sites-synthetically simple receptors for the binding and transport of HCl. Chem Comm. 2009(28):4299-301.

70. Berezin SK, Davis JT. Catechols as Membrane Anion Transporters. J Am Chem Soc. 2009 Feb 25;131(7):2458-+.

71. Sprong H, van der Sluijs P, van Meer G. How proteins move lipids and lipids move proteins (vol 2, pg 504, 2001). Nat Rev Mol Cell Bio. 2001 Sep;2(9):698-.

72. National Center for Biotechnology Information - CID=5934766. 2006 [updated 2006-04-28April 2011]; Available from: http://pubchem.ncbi.nlm.nih.gov/summary/summary.cgi?cid=6436017&loc=ec_rcs.

73. National Center for Biotechnology Information - CID=10350317. 2006 [updated 2006-04-28April 2011]; Available from: http://pubchem.ncbi.nlm.nih.gov/summary/summary.cgi?cid=10350317&loc=ec_rcs.

74. National Center for Biotechnology Information - CID=452110. 2006 [updated 2006-04-28April 2011]; Available from: http://pubchem.ncbi.nlm.nih.gov/summary/summary.cgi?cid=452110&loc=ec_rcs.

75. National Center for Biotechnology Information - CID=5459377. 2006 [updated 2006-04-28April 2011]; Available from: http://pubchem.ncbi.nlm.nih.gov/summary/summary.cgi?cid=5459377.

76. Bio-Cha. In: Licker MD, editor. Encyclopedia of Science and Technology. 10th ed. New York: McGraw-Hill; 2007. p. 634.

77. Hsueh YW, Chen MT, Patty PJ, Code C, Cheng J, Frisken BJ, et al. Ergosterol in POPC membranes: Physical properties and comparison with structurally similar sterols. Biophys J. 2007 Mar 1;92(5):1606-15.

78. Sansom MSP, Biggin PC. Molecular Simulations and Biomembranes: From Biophysics to Function. 1st ed: Royal Society of Chemistry; 2010.

79. Force fields. [Wiki] 2010 [updated 14 April 2010April 2011]; Available from: http://www.sklogwiki.org/SklogWiki/index.php/Force_fields.

80. Leach A. Molecular Modelling: Principles and Applications. 2nd ed: Prentice Hall; 2001.

81. Höltje H-D, Sippl W, Rognan D, Folkers G. Molecular Modeling: Basic Principles and Applications 3rd ed: Wiley-VCH; 2008.

82. Cramer CJ. Essentials of Computational Chemistry: Theories and Models. 2nd ed: Wiley; 2004.

83. Jojart B, Martinek TA. Performance of the general amber force field in modeling aqueous POPC membrane bilayers. J Comput Chem. 2007 Sep;28(12):2051-8.

84. Rosso L, Gould IR. Structure and dynamics of phospholipid bilayers using recently developed general all-atom force fields. J Comput Chem. 2008 Jan 15;29(1):24-37.

85. Siu SWI, Vacha R, Jungwirth P, Bockmann RA. Biomolecular simulations of membranes: Physical properties from different force fields. J Chem Phys. 2008 Mar 28;128(12):-.

86. Janosi L, Gorfe AA. Simulating POPC and POPC/POPG Bilayers: Conserved Packing and Altered Surface Reactivity. J Chem Theory Comput. 2010 Oct;6(10):3267-73.

87. Klauda JB, Venable RM, Freites JA, O'Connor JW, Tobias DJ, Mondragon-Ramirez C, et al. Update of the CHARMM all-atom additive force field for lipids: validation on six lipid types. J Phys Chem B. 2010 Jun 17;114(23):7830-43.

88. Chiu SW, Pandit SA, Scott HL, Jakobsson E. An Improved United Atom Force Field for Simulation of Mixed Lipid Bilayers. J Phys Chem B. 2009 Mar 5;113(9):2748-63.

89. Poger D, Mark AE. On the Validation of Molecular Dynamics Simulations of Saturated and cis-Monounsaturated Phosphatidylcholine Lipid Bilayers: A Comparison with Experiment. J Chem Theory Comput. 2010 Jan;6(1):325-36.

90. Marrink SJ, Risselada HJ, Yefimov S, Tieleman DP, de Vries AH. The MARTINI force field: Coarse grained model for biomolecular simulations. J Phys Chem B. 2007 Jul 12;111(27):7812-24.

91. National Center for Biotechnology Information - CID=16219887. 2006 [updated 2006-04-28April 2011]; Available from: http://pubchem.ncbi.nlm.nih.gov/summary/summary.cgi?cid=16219887&loc=ec_rcs.

92. National Center for Biotechnology Information - CID=16219822. 2006 [updated 2006-04-28April 2011]; Available from: http://pubchem.ncbi.nlm.nih.gov/summary/summary.cgi?cid=16219822&loc=ec_rcs.

93. National Center for Biotechnology Information - CID=47211568. 2006 [updated 2006-04-28April 2011]; Available from: http://pubchem.ncbi.nlm.nih.gov/summary/summary.cgi?sid=47211568.

94. National Center for Biotechnology Information - CID=445468. 2006 [updated 2006-04-28April 2011]; Available from: http://pubchem.ncbi.nlm.nih.gov/summary/summary.cgi?cid=445468&loc=ec_rcs.

95. National Center for Biotechnology Information - CID=44251425. 2006 [updated 2006-04-28April 2011]; Available from: http://pubchem.ncbi.nlm.nih.gov/summary/summary.cgi?cid=44251425.

96. Jorgensen WL. Quantum and Statistical Mechanical Studies of Liquids .10. Transferable Intermolecular Potential Functions for Water, Alcohols, and Ethers - Application to Liquid Water. J Am Chem Soc. 1981;103(2):335-40.

97. Jorgensen WL, Chandrasekhar J, Madura JD, Impey RW, Klein ML. Comparison of Simple Potential Functions for Simulating Liquid Water. J Chem Phys. 1983;79(2):926-35.

98. Heller H, Schaefer M, Schulten K. Molecular dynamics simulation of a bilayer of 200 lipids in the gel and in the liquid crystal phase. J Phys Chem-Us. 1993;97(31):8343-60.

99. Wilson MA, Pohorille A. Mechanism of unassisted ion transport across membrane bilayers. J Am Chem Soc. 1996 Jul 17;118(28):6580-7.

100. Gurtovenko AA, Vattulainen I. Pore formation coupled to ion transport through lipid membranes as induced by transmembrane ionic charge imbalance: Atomistic molecular dynamics study. J Am Chem Soc. 2005 Dec 21;127(50):17570-1.

101. Wei C, Pohorille A. Permeation of Nucleosides through Lipid Bilayers. J Phys Chem B. 2011;115(13):3681-8.

102. Wilson MA, Pohorille A. Unassisted and assisted ion transport across membranes: insights from computer simulations. Cell Mol Biol Lett. 2001;6(2A):6.

103. Wang J, Wolf RM, Caldwell JW, Kollman PA, Case DA. Development and testing of a general amber force field. J Comput Chem. 2004;25(9):1157-74.

104. Case DA, Darden TA, T.E. Cheatham III, Simmerling CL, Wang J, Duke RE, et al. AMBER 11. San Francisco: University of California; 2010.

105. Bayly CI, Cieplak P, Cornell WD, Kollman PA. A Well-Behaved Electrostatic Potential Based Method Using Charge Restraints for Deriving Atomic Charges - the Resp Model. J Phys Chem-Us. 1993 Oct 7;97(40):10269-80.

106. Avogadro: an open-source molecular builder and visualization tool. Version 1.0.1 ed2010.

107. Frisch MJ, Trucks GW, Schlegel HB, Scuseria GE, Robb MA, Cheeseman JR, et al. Gaussian 03. Revision B.04 ed. Pittsburgh PA: Gaussian, Inc.; 2003.

108. Wang J, Wang W, Kollman PA, Case DA. Automatic atom type and bond type perception in molecular mechanical calculations. J Mol Graph Model. [Research Support, N.I.H., Extramural]. 2006 Oct;25(2):247-60.

109. Jakalian A, Bush BL, Jack DB, Bayly CI. Fast, efficient generation of high-quality atomic charges. AM1-BCC model: I. Method. J Comput Chem. 2000;21(2):132-46.

110. Jakalian A, Jack DB, Bayly CI. Fast, efficient generation of high-quality atomic charges. AM1-BCC model: II. Parameterization and validation. J Comput Chem. 2002 Dec;23(16):1623-41.

111. Rappe AK, Casewit CJR. Molecular Mechanics Across Chemistry. 1st ed: Univ Science Books 1997.

112. Joung IS, Cheatham TE. Determination of alkali and halide monovalent ion parameters for use in explicitly solvated biomolecular simulations. J Phys Chem B. 2008 Jul 31;112(30):9020-41.

113. Martinez L, Andrade R, Birgin EG, Martinez JM. PACKMOL: A Package for Building Initial Configurations for Molecular Dynamics Simulations. J Comput Chem. 2009 Oct;30(13):2157-64.

114. Fox T, Kollman PA. Application of the RESP methodology in the parametrization of organic solvents. J Phys Chem B. 1998 Oct 8;102(41):8070-9.

115. Li Y, Mullen KM, Sardinha J, Felix V, Beer PD. Clipping and stoppering anion templated synthesis of a [2]rotaxane host system. Dalton Trans. 2011.

116. Cornell WD, Cieplak P, Bayly CI, Gould IR, Merz KM, Ferguson DM, et al. A second generation force field for the simulation of proteins, nucleic acids, and organic molecules (vol 117, pg 5179, 1995). J Am Chem Soc. 1996 Mar 6;118(9):2309-.

117. Loncharich RJ, Brooks BR, Pastor RW. Langevin Dynamics of Peptides - the Frictional Dependence of Isomerization Rates of N-Acetylalanyl-N'-Methylamide. Biopolymers. 1992 May;32(5):523-35.

118. Ryckaert J-P, Ciccotti G, Berendsen HJC. Numerical integration of the cartesian equations of motion of a system with constraints: molecular dynamics of n-alkanes. J Comput Phys. 1977;23(3):327-41.

119. Darden T, York D, Pedersen L. Particle Mesh Ewald - an N.Log(N) Method for Ewald Sums in Large Systems. J Chem Phys. 1993 Jun 15;98(12):10089-92.

120. Schrodinger, LLC. The PyMOL Molecular Graphics System, Version 1.3r1. 2010.

121. Kalugin ON, Volobuev MN, Ishchenko AV, Adya AK. Structure and dynamics of Na+ and Cl- solvation shells in liquid DMSO: molecular dynamics simulations. J Mol Liq. 2001 Apr;91(1-3):135-48.

122. Wakabayashi K, Maeda Y, Ozutsumi K, Ohtaki H. The structure of solvated halide ions in dimethyl sulfoxide studied by Raman spectroscopy and X-ray diffraction. J Mol Liq. 2004 Mar 15;110(1-3):43-50.

123. Kim J, Lee HM, Suh SB, Majumdar D, Kim KS. Comparative ab initio study of the structures, energetics and spectra of X-center dot(H2O)(n=1-4) [X=F, Cl, Br, I] clusters. J Chem Phys. 2000 Oct 1;113(13):5259-72.

124. Xantheas SS. Quantitative description of hydrogen bonding in chloride-water clusters. J Phys Chem-Us. 1996 Jun 6;100(23):9703-13.

125. Chiu SW, Jakobsson E, Subramaniam S, Scott HL. Combined Monte Carlo and molecular dynamics simulation of fully hydrated dioleyl and palmitoyl-oleyl phosphatidylcholine lipid bilayers. Biophys J. [Research Support, N.I.H., Extramural

Research Support, U.S. Gov't, Non-P.H.S.]. 1999 Nov;77(5):2462-9.

126. Ulrich AS, Watts A. Molecular Response of the Lipid Headgroup to Bilayer Hydration Monitored by H-2-Nmr. Biophys J. 1994 May;66(5):1441-9.

127. Hess B, Kutzner C, van der Spoel D, Lindahl E. GROMACS 4: Algorithms for highly efficient, load-balanced, and scalable molecular simulation. J Chem Theory Comput. 2008 Mar;4(3):435-47.

128. Whiteford N, Taylor J. MOLDY Tools Dublin: Trinity College Dublin; 2007 [updated 01 Jul 2010; cited 2011]; Available from: http://www.tchpc.tcd.ie/node/488.

129. Klauda JB. Free Programs, Molecular Coordinates, & Files. College Park: Department of Chemical and Biomolecular Engineering - University of Maryland; 2007 [updated 2011; cited 2011]; Available from: http://terpconnect.umd.edu/~jbklauda/research/download.html.

130. Batista PR, Wilter A, Durham EH, Pascutti PG. Molecular dynamics simulations applied to the study of subtypes of HIV-1 protease common to Brazil, Africa, and Asia. Cell Biochem Biophys. [Research Support, Non-U.S. Gov't]. 2006;44(3):395-404.

131. Sousa da Silva AW, Laue ED, Vranken WF. ACPYPE - AnteChamber PYthon Parser interfacE. 2010.

132. Lindahl E, Edholm O. Mesoscopic undulations and thickness fluctuations in lipid bilayers from molecular dynamics simulations. Biophys J. 2000 Jul;79(1):426-33.

133. Berendsen HJC, Postma JPM, Vangunsteren WF, Dinola A, Haak JR. Molecular-Dynamics with Coupling to an External Bath. J Chem Phys. 1984;81(8):3684-90.

134. Hess B, Bekker H, Berendsen HJC, Fraaije JGEM. LINCS: A linear constraint solver for molecular simulations. J Comput Chem. 1997 Sep;18(12):1463-72.

135. Kucerka N, Tristram-Nagle S, Nagle JF. Structure of fully hydrated fluid phase lipid bilayers with monounsaturated chains. J Membrane Biol. 2005 Jan;208(3):193-202.

136. Hyslop PA, Morel B, Sauerheber RD. Organization and Interaction of Cholesterol and Phosphatidylcholine in Model Bilayer-Membranes. Biochemistry-Us. 1990 Jan 30;29(4):1025-38.

137. Davis PJ, Fleming BD, Coolbear KP, Keough KMW. Gel to liquid-crystalline transition temperatures of water dispersions of two pairs of positional isomers of unsaturated mixed-acid phosphatidylcholines. Biochemistry-Us. 1981 1981/06/01;20(12):3633-6.

138. Huber T, Rajamoorthi K, Kurze VF, Beyer K, Brown MF. Structure of docosahexaenoic acid-containing phospholipid bilayers as studied by H-2 NMR and molecular dynamics simulations. J Am Chem Soc. 2002 Jan 16;124(2):298-309.

139. Seelig J, Waespesarcevic N. Molecular Order in Cis and Trans Unsaturated Phospholipid Bilayers. Biochemistry-Us. 1978;17(16):3310-5.

140. Perly B, Smith ICP, Jarrell HC. Effects of the Replacement of a Double-Bond by a Cyclopropane Ring in Phosphatidylethanolamines - a H-2 Nmr-Study of Phase-Transitions and Molecular-Organization. Biochemistry-Us. 1985;24(4):1055-63.

141. Pastor RW, Venable RM, Feller SE. Lipid bilayers, NMR relaxation, and computer simulations. Accounts Chem Res. 2002 Jun;35(6):438-46.

142. Tabony J, Perly B. Quasi-Elastic Neutron-Scattering Measurements of Fast Local Translational Diffusion of Lipid Molecules in Phospholipid-Bilayers. Biochim Biophys Acta. 1991 Mar 18;1063(1):67-72.

143. Konig S, Pfeiffer W, Bayerl T, Richter D, Sackmann E. Molecular-Dynamics of Lipid Bilayers Studied by Incoherent Quasi-Elastic Neutron-Scattering. J Phys II France. 1992 Aug;2(8):1589-615.

144. Kuo AL, Wade CG. Lipid Lateral Diffusion by Pulsed Nuclear Magnetic-Resonance. Biochemistry-Us. 1979;18(11):2300-8.

145. Vaz WLC, Clegg RM, Hallmann D. Translational Diffusion of Lipids in Liquid-Crystalline Phase Phosphatidylcholine Multibilayers - a Comparison of Experiment with Theory. Biochemistry-Us. 1985;24(3):781-6.

146. Shin YK, Freed JH. Dynamic Imaging of Lateral Diffusion by Electron-Spin Resonance and Study of Rotational-Dynamics in Model Membranes - Effect of Cholesterol. Biophys J. 1989 Mar;55(3):537-50.

147. Schwille P, Korlach J, Webb WW. Fluorescence correlation spectroscopy with single-molecule sensitivity on cell and model membranes. Cytometry. 1999 Jul 1;36(3):176-82.

148. Fujiwara T, Ritchie K, Murakoshi H, Jacobson K, Kusumi A. Phospholipids undergo hop diffusion in compartmentalized cell membrane. J Cell Biol. 2002 Jun 10;157(6):1071-81.

149. Arnold K, Pratsch L, Gawrisch K. Effect of Poly(Ethylene Glycol) on Phospholipid Hydration and Polarity of the External Phase. Biochim Biophys Acta. 1983;728(1):121-8.

150. Nagle JF. Area Lipid of Bilayers from Nmr. Biophys J. 1993 May;64(5):1476-81.

151. CHARMM-GUI. Lawrence: The University of Kansas / Department of Molecular Biosciences / Center for Bioinformatics; 2011 [updated January; cited 2011 April]; 1.1:[Available from: http://www.charmm-gui.org/?doc=input/membrane.

152. Busschaert N, Wenzel M, Light ME, Iglesias-Hernández P, Pérez-Tomás R, Gale PA. Structure–Activity Relationships in Tripodal Transmembrane Anion Transporters: The Effect of Fluorination. J Am Chem Soc. 2011;133(35):14136-48.